BIO-INSPIRED AND BIOMIMETIC ENDOGENOUS CORNEA REPAIR AND REPLACEMENT STRATEGIES

By
Shoumyo Majumdar

A dissertation submitted to Johns Hopkins University in conformity with the requirements for the degree of Doctor of Philosophy

Baltimore, Maryland
August, 2017

Abstract

The cornea is an avascular and transparent tissue, refracting light towards the retina. Corneal collagen fibers run parallel to each other and organize into stacked lamellae. Corneal ectasia due to diseases such as keratoconus causes disruption of the organized ultrastructure, significantly impairing vision. In more severe disease conditions, or when the cornea stroma is damaged, blindness can occur as a result of tissue fibrosis requiring corneal transplantation. This dissertation addresses the need for development of safer and more effective treatments for corneal disease and transplantation.

An *ex vivo* corneal ectasia model was developed to ascertain efficacy of novel therapies for corneal ectasia. Reinforcement of corneal biomechanics, thermal stability, restoration of damaged corneal stromal ultrastructure and gene expression following treatment with tissue derived extracellular matrix (ECM) microparticles was investigated. ECMs significantly improve corneal biomechanics, reduce inflammation and maintain healthy keratocyte phenotype. Concurrently, functionalized chondroitin sulfate (CS) proteoglycans which were used to chemically crosslink the corneal stroma promoted lamellar and fibrillar stabilization, restored stiffness and lowered proinflammatory gene expression, compared to the conventional clinical treatment. These therapies indicate that harnessing biological and bio-inspired crosslinking techniques allow for equally effective, and significantly safer corneal ectasia treatments.

Further, to engineer biosynthetic corneal transplants, collagen self-assembly processes were modulated using cyclodextrins (CD) as artificial chaperones to create biomaterials that mimic native corneal structure. Combination of βCD with collagen (Col) gelation and vitrification produced materials with aligned fibers and lamellae that were mechanically robust and transparent. Molecular analysis revealed CD formed reversible interactions with hydrophobic amino acids on the collagen chains. To translate *in vivo*, custom molds for gelation and vitrification were

engineered to create βCD/Col implants with corneal curvature which were implanted in rabbits. Moreover, fibrillogenesis and collagen gelation was modulated though controlled ammonia exposure conditions. Changes in duration of exposure and points of surface contact were able to confer control over the fibrillar structures formed. Use of straightforward gelation techniques and inexpensive artificial chaperones could potentially be used to manipulate collagen assembly to engineer biomaterials with advanced structural and functional properties.

Readers:

Professor Jennifer Elisseeff

Professor Hai-Quan Mao

Acknowledgements

First and foremost, I would like to express my gratitude to my advisor, Professor Jennifer Elisseeff for her invaluable advice and guidance, and my academic advisor Professor Hai-Quan Mao for his constant support and help. I am also deeply appreciative of Professor Anirudha Singh, Professor Kalina Hristova, and Dr. Oliver Schein for their invaluable comments and constructive criticism as members of my thesis defense committee.

A special thanks to Dr. Marcos-Garza Madrid, Dr. Qiongyu Guo, Dr. Xiaokun Wang, Dr. Jemin J. Chae in the Elisseeff lab who all helped in mentoring and teaching me in the beginning of my graduate studies, and provided me with assistance and advice whenever I needed it. I would also like to extend a heartfelt appreciation to all past and present members of the Elisseeff lab during my time as a graduate student, for their technical, intellectual and moral support, all of which contributed to my success and the development of my analytical and scientific skills.

I am also very grateful to Dr. Morgana Trexler, Professor Stellacci, Dr. Tripp, Professor Amzel, Barbara Smith, Michael Delannoy and Evangelia Athanasopoulou who have helped both directly and indirectly with training and running several specialized equipment. A very special gratitude goes out to Tony Lee, Dr. Derek Duan, Jack England, Priscilla Carbajal and Kylie Matsumoto at Eyegenix, LLC for their counsel on product development, quality and translation of the research.

I also wish to express my gratitude to Research to Prevent Blindness, the US Department of Defense, and the Wilmer Eye Institute, who helped fund this research. I am also grateful to the faculty and staff of the Translational Tissue Engineering Center, and Department of Materials Science and Engineering at the Johns Hopkins University for their unfailing support, encouragement, financial means and laboratory facilities that permitted my research.

Finally, last but by no means the least, I am thankful for my friends and family – especially my parents, siblings, and my wife – for their patience, encouragement, and boundless love during the course of my studies.

Table of Contents

List of Tables

List of Figures

1. Introduction

The cornea is the transparent, anterior-most ocular tissue, with a highly organized extracellular matrix. Normal cornea tissue structure provides a clear and mechanically robust surface for the outermost segment of the eye. When the cornea is damaged, due to injury or disease, loss of vision occurs. Diseases such as Keratoconus are characterized by progressive thinning and ectasia of the cornea, creating a cone-shaped cornea, severe stigmatism, and visual impairment [1]. Up to 20% of keratoconus patients require keratoplasty, or corneal transplantation. A number of treatment modalities have been developed to reduce corneal deformation and correct vision. Corneal crosslinking via UV light is a popular strategy that enhances mechanical properties of the cornea and potentially reduce disease progression [2]. However, little is known about the ultrastructural changes that occur during crosslinking, therapeutic optimization, and long-term consequences.

In case of deeper corneal stromal wounds, the cornea stroma cannot repair itself; instead it undergoes a scarring process that limits transparency and impairs vision. In the U.S. alone, total medical costs related to injuries and burns to the eye resulting in visual disability in patients, was $1.3 billion in 2013, not including corneal defects and disease[3]. Keratoplasty is the most frequent clinical intervention. Although donor tissue is not in short supply in the US, demand is steadily increasing. Total demand for corneal graft tissue in the US has seen a 45% increase from 52,487 in 2008 to 76,431 in 2014[4]. several barriers limit the effectiveness of keratoplasty. In the U.S., the costs of tissue are high and the shelf life of donor tissue in storage media is limited. While implant rejection rate for first-time transplant recipients is relatively low at 10% without immunosuppression or antigen matching, rejection rates climb to as high as 70% for high-risk patients with vascularization or previous transplant rejection history[5,6,7,8]. These patients need another option for corneal replacement.

In developing countries, corneal blindness is even more prevalent, and the availability of quality donor tissue is extremely limited. In certain parts of Africa, almost 90% of all blindness is caused by underlying corneal pathology[9]. A recent review estimated that globally, only 1 cornea is available for 70 that are needed[10]. The pool of donor tissue is decreasing globally owing to the increased rates of surgery for refractive correction. One review concluded, “Efforts to encourage cornea donation must continue in all countries, but is also essential to develop alternative and/or complementary solutions, such as corneal bioengineering.”[10] Rejection and mechanical failure (non-immunologic loss of corneal clarity over time) are common, especially for younger patients and those with ocular comorbidities[11]. In both developed and developing nations, alternative options for preventing corneal disease progression and repairing corneal injury and scarring are needed.

In the following dissertation, the author addresses corneal disease and injury treatment with multiple biologically inspired strategies. Chapter 2 of this thesis aims to understand and modulate fibrillogenesis in collagen gels to study changes in physical, thermal and biological characteristics, thereby controlling corneal stromal phenotype when based on collagen fibrillar nanoarchitecture of the cell substrate. In Chapter 3 and 4, the thesis explores the development of bio-inspired corneal ectasia therapies. These therapies aim to increase safety of treatment modalities while maintaining the level of crosslinking efficacy seen in current treatment options. These sections involve the development of *ex vivo* ectasia model followed by microparticle ECM treatment of corneas in Chapter 3 and chondroitin-sulfate proteoglycan crosslinking in Chapter 4. These methods efficiently crosslink the ex vivo corneas and were observed to be safer than the traditional UV crosslinking methods currently used in the clinic.

Chapter 5 describes the design and development of bio-mimetic biomaterial collagen implant that replicates the native cornea structure. Owing to the knowledge gained from Chapter 2 about cell behavior on collagen substrates, and from Chapter 3/4 regarding effects of proteoglycan

interactions with collagen, a biomaterial with artificial chaperones to direct collagen fibril formation and organization was envisioned. The cornea mimetic materials are formulated and optimized for mechanical, thermal, optical characteristics. Biophysical and ultrastructural studies of biomaterials depict the control and unique structural arrangement from controlled self-assembly of the collagen. Further, we establish biocompatibility and evaluate the *in vivo* performance of the biomaterials in a corneal defect model.

Chapter 6 contends with another unique collagen-based biomaterial formulation, wherein directed modulation of collagen fibrillogenesis is achieved through ammonia exposure. Full characterization and implantation of the resulting biomaterials in vivo is successfully undertaken.

1.1. Corneal Ectasia Progression and Current Clinical Treatments

The cornea has a unique matrix structure that allows it to have clarity for vision and mechanical strength to protect the eye and support vision acuity. The matrix is composed of collagen fibrils that are highly organized into lamellae. In addition, proteoglycans (PGs) intermingle to organize and provide additional mechanical properties to the meta-structure [12]. This extracellular matrix structure influences the biological properties and behavior of keratocytes that populate the corneal stroma. Keratoconus is a disease where the corneal stroma matrix becomes disrupted and loses this fine structural organization [13]. Clinically, keratoconic corneas (KCs) are treated by riboflavin (RF)-catalyzed crosslinking of the corneal stroma under exposure of long-wavelength ultraviolet light (UVA). In normal corneas, the crosslinking reactions were reported to be carbonyl-based, and mainly happened within the single collagen fibrils and the PG core proteins [14]. A limited number of linkages are present between collagen fibrils and the PG [15], which can be explained by the dependence of the crosslinking reaction on the availability of functional groups within a distance of 5-10 nm [16]. This distance is shorter than the fibril spacing in normal corneas and it can be anticipated that in the KC corneas, the frequency of natural crosslinking reactions will be even

more negatively impacted due to the disrupted collagen fibrillar organization and the dysfunctional PGs between the collagen fibrils. However, no systematic study has been reported to understand the changes in the diseased cornea in response to the crosslinking reaction as compared to the normal cornea. Moreover, significant reduction of keratocyte density in KCs was reported after RF-UVA treatment, indicating a potential cytotoxicity issue from the crosslinking process [17]. A comprehensive investigation of the evolution of the extracellular matrix (ECM) in the diseased cornea under RF-UVA crosslinking is critical to both gaining insight into disease mechanisms and maximizing therapeutic strategies to salvage the cornea. Therefore, the goal is to develop new therapeutic agents for corneal crosslinking to re-establish normal cornea architecture and mechanical properties while remaining biocompatible. Considering the limited linkages between the collagen fibril and the PG due to shortage of functional groups, disperse ECM components or specific PGs would serve well as crosslinkers for the crosslinking reaction. The crosslinking conditions, including the reaction medium, the dosage of the bio-crosslinkers, and the exposure time, would need to be evaluated and optimized. ECM changes that occur with bioinspired therapies could be tested in rabbit cadaver eyes.

1.2. Complex Collagen Organization in Corneal Stroma

The structure of corneal tissue makes it challenging to engineer and mimic. The cornea has a highly organized and complex extracellular matrix (ECM) structure making it uniquely transparent. Corneal tissue is avascular, and consists of three major layers: the outermost epithelium, the stroma, and the innermost endothelium. The stroma represents over 90% of the total cornea, sparsely populated with keratocyte cells and composed mainly of type I collagen extracellular matrix molecules and smaller percentages of type V collagen and proteoglycans. The corneal stroma also has a unique structural organization of approximately 200 lamellae, each 2-μm thick, which contribute to the mechanical strength and transparency of the tissue [18]. Collagen fibrils in each layer are aligned in parallel, but in each lamellae the alignment of the collagen fibrils is orthogonal

(at a right angle) to the adjacent layers above and below[19]. The orthogonally aligned collagen lamella with defined interfibrillar spacing gives rise to the unique property of transparency of the cornea tissue [20]. To date, this unique organization has not been replicated in a biomaterial on the size scale of the native cornea, therefore leading to inadequate functional properties.

1.3. Current Options for Keratoplasty and Competing Strategies.

Several strategies evolved over the years in an attempt to obviate the use of allograft corneas. As early as the 1980s, purely synthetic materials, such as poly(methyl methacrylate), were developed as corneal implants [21] and were approved for clinical use, including the Boston keratoprosthesis (1992) and AlphaCor (2002). Although these synthetic corneal replacements can restore vision, they are not able to integrate with the surrounding tissue causing graft extrusion and failure. Clinical reports found the failure rate of AlphaCor to be 20% in the first year and up to 58% by the third year [22]. Similarly, the association of the Boston keratoprosthesis with blinding glaucoma, endophthalmitis, and prosthesis-host intersection keratolysis has largely limited that technology to patients who have failed multiple conventional corneal transplantation efforts. More recently, researchers have moved from synthetic polymers to biological polymers to create corneal substitutes that are more biocompatible with the ocular surface and can potentially better integrate with the surrounding tissue. One such biological corneal substitute was engineered by the Griffith group at Linköping University (Sweden) using crosslinked collagen gels [23]. This biological corneal replacement was tested in preclinical pig and rabbit models [24,25] and translated—as a prototype derived from recombinant human type III collagen (RHCIII)—to human trials. Although this achievement represented an exciting shift in corneal replacements, the implant did not have adequate mechanical strength to support standard suturing techniques, such as single interrupted sutures[26]. This limited mechanical integrity is likely due to the low collagen density and lack of collagen fibrillar organization in the implants compared to the native tissue. Recent approaches taking advantage of the liquid crystal properties of highly concentrated collagen

solution have been developed, such as long-term dialysis[27] and molecular crowding to produce collagen fibrils and organized lamellae[28]. These methods are able to create thin collagen membranes with lamellar structures that are similar to the native cornea structure, but owing to the viscosity of these highly concentrated collagen solutions, it is thus far challenging to manufacture materials with a thickness relevant for corneal transplantation. Finally, synthetic materials such as functionalized silk and PLGA membranes, although effective cell carriers, may cause significant immune responses similar to other synthetic materials in the eye, in addition to the difficulties in clinical translation due to requirement of cell seeding, and the lack of thickness, strength, and transparency.

Table 1.1 Strengths and weaknesses of emerging approaches to create biosynthetic corneas

Material	Strengths	Challenges
Crosslinked RHCIII biosynthetic cornea[29]	Transparent, in vivo, in clinical stage	Not suturable, lacks corneal ultrastructure
RGD functionalized silk[30]	Cell alignment on individual sheets	Fibroblasts seeded – less translatable, thin, no mechanical data
Collagen constructs[28]	Cornea mimetic structure	Non-implantable, no mechanical data
TEC PLGA membranes[31]	Effective cell carrier, fibril control with electrospinning	Non-transparent, possible biocompatibility issues, membrane degradation
CD-Col vitrigels	Transparent, suturable, biomimetic, biocompatible	Optimization and mechanism studies required

Currently, there is no corneal substitute that mimics native cornea's suturability, thickness, and transparency. A corneal substitute would benefit patients with failed corneal transplants or those that have an underlying condition that precludes corneal transplant.

1.4. Controlled Self-assembly of Collagen through Artificial Chaperones

Artificial self-assembled cornea materials represent a new paradigm in guided self-assembly processes. Using synthetic chaperone molecules with biologically derived materials may spur

innovation in understanding and modulating biological ECM scaffold organization, spacing, and alignment. Such insight is relevant in multiple tissue engineering fields. The new biomaterial that we have developed exhibits unique properties that have not yet been achieved in a corneal substitute. Experimentally, we are incorporating innovative analysis in the characterization of the implant.

Table 1.2 Comparison of emerging biosynthetic corneal technologies with native cornea.

Material	Transparent	Suturable	400-500 um thickness	Collagen alignment	Lamellar ultrastructure
Native Cornea	✓	✓	✓	✓	✓
Crosslinked RHCIII	✓	×	×	×	×
RGD functionalized silk	✓	×	×	✓	✓
Collagen constructs	✓	×	×	✓	✓
TEC PLGA membranes	×	✓	✓	×	×
CD-Col vitrigels	✓	✓	✓	✓	✓

Engineers have tried to mimic normal embryological development to synthesize more functional tissues for a variety of applications. Stem cells are frequently employed to recapitulate development. Here, we are mimicking the unique developmental assembly of the cornea ECM *without* a cellular component by combining CD and vitrification with collagen. The CD molecules mimic the small proteoglycan chaperones that help to assemble and create the complex cornea ECM structure during the native cornea development. Furthermore, the vitrification process combined with these chemistries provides the collagen concentrating and fibril assembly mechanism. The result of this new approach mimicking embryonic cornea ECM development using self-assembly is a biomaterial with the unique structure of the native cornea tissue.

1.5. Cornea-mimetic Biomaterial Structure and Resulting Properties.

An ideal biomaterial for corneal transplantation would, at minimum, have three fundamental physical characteristics – high transparency, physiological thickness and suturability. These parameters are interdependent, making optimization challenging. For instance, increasing thickness may increase suturability, but decreases transparency. Other existing corneal biomaterials-based strategies have focused on only one or two of these crucial characteristics. The biomimetic corneal implant described in this thesis is the first example of a biomaterial that is able to achieve all three: transparency and sutures retention at physiologically relevant thicknesses. We believe this is possible due to the cornea mimetic structure of our biomaterials that demonstrate collagen fibrils and a macro scale lamellar organization, suggesting the underlying ultrastructure of the material may play a larger role in the physical characteristics of the material than previously anticipated.

1.6. Collagen Biomaterial Processing to Create Vitrigels.

Several innovations underpin the material development process. Collagen vitrification increased mechanical strength Specifically, collagen membranes with fibrillar structures were developed in collaboration with Dr. Toshiaki Takezawa, the inventor of collagen vitrigels [32,33,34]. In collaboration with the Applied Physics Laboratory (APL), processing conditions were further optimized to reduce vitrification time and to increase mechanical strength and transparency of the gels [35], and exhibit biophysical properties superior to standard amorphous collagen gels. The fibrillar structure of the collagen vitrigel allowed cultured corneal keratocytes to maintain their *in vivo* phenotypes (defined by morphology and gene expression) more than amorphous collagen gels or tissue culture polystyrene, where cells typically became fibroblastic [33,36]. These vitrified collagen membranes also demonstrated biocompatibility *in vivo* in partial corneal defects in a rabbit model [37]. However, these membranes were thin (~50 μm), whereas the natural cornea is humans 500 μm.

1.7. Chaperone Molecules to Enhance Transparency

To create an implant with a thickness similar to the full-thickness cornea, cyclodextrin (CD) molecules were introduced. CD serves as an artificial proteoglycan chaperone substitute by interacting specifically with the amino acids on the collagen triple helices to control fibrillogenesis and ultimately their alignment and self-assembly into layers. CD-collagen interactions influence collagen ultrastructural self-assembly, similar to the role of chaperone molecules during natural corneal development, facilitating the formation of lamellae within the implant, as well as collagen alignment within each lamella. Here, we developed a CD-collagen (CD-Col) material to characterize and understand mechanistically how the biomimetic structure is created and to translate the technology in the development of a cornea implant.

2. Modulation of keratocyte phenotype by collagen fibril nanoarchitecture in membranes for corneal repair[1]

2.1. Introduction

The extracellular matrix (ECM) is a complex mixture of macromolecules that provides an environment for cellular development and homeostasis unique to each tissue and organ in the body[38,39,40]. The cornea, in particular, has a unique ECM structure that is primarily composed of type I collagen. The collagen molecules in the cornea are organized at many length scales from the aggregation of triple helices followed by fibril formation at the nanoscale. Collagen fibrils are then assembled into layered lamellar plates arranged in an orthogonal orientation[41]. This fibrillar lamellar organization in the cornea contributes to the unique clarity of the tissue[42].

One remarkable feature of the ECM is a continuous change of the hierarchical structures with time as cellular development or differentiation evolves. In the embryonic corneal stroma, the matrix begins as a water-rich state and then progressively transforms into a densely packed fibrillar ECM characteristic of adult corneas[43]. In contrast, progressive degeneration of the ECM in the corneal stroma leads to keratoconus. Associated with localized corneal thinning and protrusion, keratoconus represents a leading reason for corneal transplantation[44,45]. On the other hand, when the corneal stroma is injured, keratocytes, the corneal stromal primary cell type, respond readily but transition towards a fibroblast and myofibroblast phenotype and generate scar tissue[46,47]. Therefore, the ECM architecture is both a consequence and a cause for the development, degeneration, and regeneration of the tissue.

[1] Text and figures in this chapter reprinted from Biomaterials 2013, 34 (37), Guo, Q.; Phillip, J. M.; Majumdar, S.; Wu, P. H.; Chen, J.; Calderon-Colon, X.; Schein, O.; Smith, B. J.; Trexler, M. M.; Wirtz, D.; Elisseeff, J. H., Modulation of keratocyte phenotype by collagen fibril nanoarchitecture in membranes for corneal repair, 9365-72, (2013), with permission from Elsevier (Copyright license number: 4171410485526)

Maintaining the keratocyte phenotype during wound healing represents a significant challenge in corneal repair and regeneration[48,49]. Type I collagen is a natural choice employed frequently as an engineered ECM substitute for corneal repair[23]. However, conventional collagen gels are composed of loose networks of type I collagen fibrils with little organization, which is hardly comparable to the collagen structure in cornea. Compression of conventional collagen gels has been employed to increase collagen density and stiffness by applying a load onto the gel[50]. These plastically compressed collagen matrices improved cell expansion and stratification of corneal limbal epithelial cells, but still showed limited success in maintaining the cellular phenotype[51,52]. In contrast, amniotic membrane (AM), a naturally derived ECM product used clinically to aid in corneal re-epithelialization, was able to preserve the characteristic morphology and keratocan expression of keratocytes[53]. However, amniotic membrane lacks standardization in its sources and processing method[51]. Recently, we used vitrified collagen biomaterials (collagen vitrigel, CV) developed by Takezawa et al.[32] to culture various cell types found in the cornea with the ultimate goal of developing corneal substitutes[33,54]. CVs are synthesized from type I collagen, and could be standardized with straightforward manufacturing and handling procedures. During vitrification, collagen gels are exposed to a specific temperature and humidity that cause controlled evaporation of the water and organization of collagen fibrils. This vitrification process mimics, to some degree, the collagen maturation that occurs during the developmental formation of the corneal stromal ECM[43,55]. More recently, we completed a design-of-experiments to evaluate the effects of time, temperature and humidity variables on collagen fibril structure, optical, mechanical, and thermal properties of CVs[35]. Ultimately, a variety of fibrillar structures were obtained that had a significant impact on strength and transparency. However, the effects of collagen nanoarchitectures created through vitrification processing on keratocyte responses remain unknown.

The purpose of this study was to evaluate the biological response of keratocytes to CVs with varying fibrillar content and organization. We hypothesize that CVs with controlled fibrillar collagen may provide an optimal environment for maintaining the keratocyte phenotype. CV properties were manipulated by using different temperatures and processing times during vitrification. Keratocyte response was characterized by cell morphology and gene expression under either serum-free or serum-based cultures. Typically, in previous studies, keratocyte phenotype was analyzed qualitatively[48]. Here, we quantitatively examined keratocyte morphology in terms of cell size, protrusion number, and protrusion length, using a custom-designed program written in MATLAB (MathWorks, Natick, MA)[56,57,58].We also evaluated the effect of the CVs' collagen nanoarchitectures on various keratocyte gene expressions, including the expressions of keratocan, aldehyde dehydrogenase (ALDH), and biglycan.

2.2. Materials and methods

2.2.1. ***Preparation of collagen membranes***

Collagen membranes were prepared in a three-step procedure, as previously described[33]. First, conventional collagen gel was formed by mixing equal volumes of 0.5% type-I collagen solution (native collagen from bovine dermis, pH ¼ 3.0, AteloCell, Cosmo Bio Co., Ltd., Tokyo, Japan) and culture medium containing Dulbecco's Modified Eagle's Medium (DMEM), 10% fetal bovine serum (FBS), 20 mM hydroxyethyl piperazineethanesulfonic acid (HEPES), 100 units/mL penicillin, and 100 mg/mL streptomycin. The mixed solution of 2.0 mL was quickly poured into one well of a 6-well plate, and then incubated at 37 °C for 2 h to complete the gelation of the collagen. Second, the collagen gel was aseptically vitrified by drying under a controlled temperature and relative humidity for a prescribed time period from half week up to 8 weeks. The relative humidity of 40% was used unless otherwise specified. The collagen gel was first vitrified over 3 days and then rinsed thoroughly with PBS buffer three times for 10 min each to completely

remove the serum-based culture medium. The collagen gel was further vitrified until a predetermined time was achieved, leading to the formation of a rigid glasslike collagen membrane. Third, the collagen membrane was thoroughly rehydrated with PBS buffer before use. The thicknesses of CVs right before and after rehydration were calculated from measuring the weight and assuming a constant density of 1 g/mL.

2.2.2. ***Transmission electron microscopy (TEM)***

The nanostructure of collagen membranes was examined by TEM. Samples were fixed in 3% paraformaldehyde, 1.5% glutaraldehyde, 5 mM MgCl2, 5 mM CaCl2, 2.5% sucrose, and 0.1% tannic acid in 0.1 M sodium cacodylate buffer at pH 7.2 overnight at 4 °C. After buffer rinse, samples were post-fixed on ice in the dark in 1% osmium tetroxide for 1 h. Following a DH2O rinse, plates were stained with 2% aqueous uranyl acetate (0.22 mm filtered, 1 h, dark) and dehydrated in a graded series of ethanol before being embedded in Eponate 12 resin (Ted Pella, Inc., Redding, CA). Plates were polymerized for two to three days at 37°C before transferring them to 60 °C overnight. Thin sections, 60e90 nm, were cut with a diamond knife on the Reichert-Jung Ultracut E ultramicrotome and then placed on naked copper grids. Grids were stained with 2% uranyl acetate in 50% methanol. They were imaged with a Hitachi 7600 TEM at 80 kV. Images were captured with an AMT CCD (1k x 1k) camera (Advanced Microscopy Techniques, Woburn, MA). TEM images of both transverse and coronal planes in the CV central portions were obtained. ImageJ (NIH, Bethesda, MD) were used to analyze the collagen fibril organization in CVs, including the fibril diameter, fibril density, and D-periodicity of collagen banding. Specifically, both fibril diameter and D-periodicity of collagen banding were evaluated fromw50 collagen fibrils in the transverse plane view of the TEM images. The fibril density was obtained based on the measurements of four different locations in the coronal plane view of the TEM images.

*2.2.3.**Keratocytes isolation and culture***

Full-thickness corneas were harvested from bovine eyes within 36 h after slaughter. Keratocytes were isolated using a sequential collagenase (Type 2, Worthington Biochemical Corp., Lakewood, NJ) digestion. Specifically, bovine corneas were collected and cut into small pieces with a scalpel and then transferred to a 50-mL centrifuge tube containing 3 mg/mL collagenase in DMEM/F-12. The corneal pieces were incubated on a rotary shaker at 240 rpm at 37°C for 60 min and then collected using a 70 mm cell strainer (BD Falcon, BD Biosciences, San Jose, CA). The partially digested corneas were transferred to a fresh collagenase solution for a second digestion for 60 min. This process was repeated for a third digestion for 120 min, and the digested cells from the third digestion were collected and centrifuged at 1400 rpm for 10 min. The cell pellet was resuspended and cultured on general tissue culture plates (TCP) or CV-covered plates at 37°C and 5% CO2. Either serum-free or serum-based culture medium was used. The serum-free medium consisted of DMEM/F-12, 1% of 10 U/mL penicillin-streptomycin, and 0.5% of 1.25 mg/mL amphotericin B (Life Technologies, Carlsbad, CA). The serum-based medium contained DMEM/F-12, 10% FBS, 1% of 10 U/mL penicillin-streptomycin, and 0.5% of 1.25 mg/mL amphotericin B. The cells were plated at a concentration of 5000 cells/cm2 using the serum-free medium, while at a concentration of 1000 cells/cm2 using the serum-based medium. Before imaging and gene expression analyses, keratocytes were cultured over 3 weeks in serum-free medium or 6 days in serum-based medium. Keratocyte morphologies were examined by staining with the LIVE/DEAD Viability/Cytotoxicity Kit (Life Technologies).

*2.2.4.**AlamarBlue assay***

Proliferation of keratocytes was measured by AlamarBlue assay (Invitrogen, Frederick, MD). This assay employs a fluorometric/colorimetric growth indicator that changes from an oxidized (non-fluorescent, blue) form to a reduced (fluorescent, red) form when reduced by mitochondrial

respiration of the cells. In this assay, the percent reduction of AlamarBlue, which is determined by the ratio of the concentration of the reduced form to the total concentration of AlamarBlue, is proportional to the number of cells. Primary keratocytes were plated in 24-well plates at a concentration of 5000 cells/cm2 using the serum-free medium, or 1000 cells/cm2 using the serum-based medium. At predetermined time points, the medium was refreshed and cells were incubated with 10% AlamarBlue at 37°C and 5% CO2 for 4 h. A sample of 200 mL of AlamarBlue solution was then transferred into a 96-well plate for fluorescence reading. The absorbance was monitored at 570 nm and 600 nm using a fluorescence plate reader (Synergy 2, Biotek, Seattle, WA). The proliferation of keratocytes was determined by the increase of AlamarBlue reduction at Day 4 relative to Day 2. This assay was performed in four independent experiments.

2.2.5. ***Quantification of cellular morphology***

Image processing for quantification of the cellular morphological features from fluorescent images was carried out using a custom-designed program developed in MATLAB[57,58]. In brief, we first segmented individual cells in images and measured the cell spreading area. For the quantification of protrusion morphology, we first determined the morphological skeleton of individual cell contours and identified the main body region of cells[59]. The protrusions were identified as the skeleton structures that were extended beyond the main body region. The protrusions were further classified into two subtypes: 1st order protrusions and 2nd order protrusions. The 1st order protrusions were considered to be the protrusions stemming directly from the cell body, and 2nd order protrusions were the ones branching from other protrusions. The length of each protrusion was measured and the total number of protrusions for individual cells was determined as the summation of 1st order and 2nd order protrusions. The morphology of keratocytes, including cell size, total number of protrusions, mean length of protrusions, primary protrusion number, secondary protrusion number, and the ratio of secondary to primary protrusions, was evaluated based on the measurements of w60 cells.

2.2.6. ***Gene expression analysis***

Total RNA was isolated from cultured keratocytes using TRIzol reagent (Life Technologies) and reverse transcribed into cDNA using SuperScript II First Strand Synthesis Kit (Life Technologies). cDNA was used for real-time PCR reactions using a StepOnePlus Real-Time PCR System (Applied Biosystems, Life Technologies). The PCR primer sequences are listed in Table 1. GAPDH was used as a reference gene. The relative gene expression was determined using the 2eDDC(T) method[60].

2.2.7. ***Statistics***

Data were represented as averages +/- standard deviations, unless otherwise specified. Two-tailed unpaired t-tests were performed to determine significance using GraphPad Prism (GraphPad Software Version 5, GraphPad Software, Inc., La Jolla, CA). p value of <0.05 was considered statistically significant.

2.3. Results

2.3.1. ***Collagen vitrigel preparation and nanoarchitecture***

CVs were prepared following a three-stage sequence: gelation, vitrification, and rehydration (**Figure 2.1**A)[33,35]. When the collagen solution containing 2.5 mg/mL type I collagen was first gelled at 37°C for 2 h, it produced a collagen gel with a thickness of 2.0 mm. This collagen gel was translucent and soft. During vitrification, the collagen gel was dried slowly at a controlled temperature of either 5°C or 39°C under a relative humidity of 40%. This resulted in CV formation with a dramatically decreased thickness. After vitrification at 5°C for 2 wk, the vitrified gel had a thickness of 9 _ 1 mm, which is a 220-fold decrease in the thickness of the membrane. To compare, the CV vitrified at 39°C for 2 wk exhibited a smaller thickness of 6 _1 mm, which is a 330-fold

decrease in the thickness. After rehydration, the CV still maintained its shape and swelled in PBS buffer to form a hydrated membrane with a thickness of approximately 50 mm.

CVs reconstructed from highly hydrated collagen gels showed a distinctive nanoarchitecture. Fiber morphology depended on the CV conditions as visualized through TEM images in the middle portions. A three-dimensional view of a CV (5°C, 2 wk) is shown in **Figure 2.1**B. Unlike conventional collagen gel showing homogeneous distribution of the collagen fibrils, this CV demonstrated a random fibrillar organization in the transverse plane, but showed a layer-by-layer lamellar structure in the coronal and sagittal planes. Similar results were also observed in all the other CVs, even for the CV 5°C, 0.5 wk that was vitrified for a short time period (**Figure 2.2**A-H).

The organization of the collagen fibrils was strongly affected by the vitrification processing conditions, including the temperature and the vitrification time. First, no significant difference in collagen fibrillar diameter was observed in despite of varying vitrification temperature and vitrification time (**Figure 2.2**I). Second, all of the samples clearly showed the characteristic collagen banding with spacing around 60 nm (**Figure 2.2**J). No significant difference in D-periodicity was observed at different temperatures and vitrification times. Third, at a constant temperature, the collagen fibril density dramatically increased along with the vitrification time (**Figure 2.2**K). The fibril density of the CV at 5°C for 0.5 wk is as low as 5 fibers/ mm2. After vitrification at 5°C for 2 wk, the fibril density was dramatically increased to 95 fibers/mm2. For the CVs prepared at 39°C, the fibril density was very high and close to the maximum density of the fiber in the collagen matrix, which was estimated to be 180 fibers/mm2 based on an assumption of hexagonally arranged collagen fibrils with fibril diameter of 80 nm. Therefore, the collagen fibril density increased with vitrification temperature, which is consistent with the decreased membrane thickness as we observed above. Furthermore, collagen fibrils with large bending curvature decreased in the CVs prepared at a higher temperature and/or longer vitrification time when

comparing the CVs vitrified for 2 wk at 5°C vs. 39°C, vitrified at 5°C for 0.5 wk vs. 2 wk, and vitrified at 39°C for 1 wk vs. 2 wk (**Figure 2.2**A-D).

*2.3.2.**Morphology and proliferation of sub cultured keratocytes***

The CV nanoarchitecture modulated keratocyte morphological response. Typical morphologies of keratocytes cultured on these CVs are shown in **Figure 2.3**A-H. Characteristic stellar phenotype of cultured keratocytes was observed using serum-free medium (**Figure 2.3**A-D). Compared to the TCP control, the keratocytes cultured on CVs had more and longer protrusions, as well as more intercellular connections. The number and length of keratocyte protrusions increased on the CVs processed for longer vitrification times. Moreover, more pinning points were observed in the extended protrusions of the keratocytes cultured on the CV processed for a longer time, especially on the CV 39°C, 8 wk (**Figure 2.3**A-D). Keratocyte morphology under serum-free culture was analyzed quantitatively with a custom-designed program written in MATLAB [24,25]. **Figure 2.4**A-C illustrates an example of a keratocyte cultured on CV 39°C, 8 wk. Individual cellular contours were first obtained identification of the cell body and protrusions (**Figure 2.4**B). The cell size was determined as the area within the cellular contour, including cell body and protrusions. Based on the cellular contour, the morphological skeleton was determined and the protrusions were classified into two subtypes depending on their starting position. Primary protrusions, or 1st order protrusions, were defined as the longest protrusions stemming directly from the cell body, while secondary protrusions, or 2nd order protrusions, were those branching from the primary protrusions. Keratocyte morphologies were carefully quantified, including cell size, total number of protrusions, mean length of protrusions, number of primary protrusions, number of secondary protrusions, and the ratio of secondary to primary protrusions. The cell sizes of keratocytes cultured on CVs were significantly higher than those cultured on TCP (**Figure 2.4**D), which is related to the increased number and length of protrusions (**Figure 2.4**E-F). **Figure 2.4**E shows that the number of protrusions per each keratocyte increased with the vitrification time of the CVs. Keratocytes

cultured on CV 39°C, 8 wk exhibited on average 27 protrusions per cell, a 70% increase over the average number of protrusions of those cells cultured on TCP. A similar, but smaller trend was also observed in the mean length of keratocyte protrusions. Interestingly, no significant difference was observed in the primary, or 1st order, protrusion number of the keratocytes cultured on TCP and CVs (**Figure 2.4**G). In contrast, the average number of secondary, or 2nd order, protrusions of the keratocytes increased markedly from 7 protrusions in TCP, to 12 protrusions in CV (39°C, 1 wk), to 14 protrusions in CV (39°C, 2 wk), and to 18 protrusions in CV (39°C, 8 wk) (**Figure 2.4**H). A similar trend to the secondary protrusion number was also observed in the ratio of secondary to primary protrusions, further demonstrating that extent of branching/number of secondary protrusions per primary protrusion increased as a function of vitrification time (**Figure 2.4**I).

The cellular proliferation rate, determined by AlamarBlue, changed depending on the CV structure/morphology (**Figure 2.5**). Under serum-free culture and compared to the TCP control, a significant increase in the keratocyte population was indicated on the three CVs with highly condensed collagen fibrils, including CV (5°C, 2 wk), CV (39°C, 1 wk), and CV (39°C, 2 wk). Moreover, when comparing CV (5°C, 1 wk) vs CV (5°C, 2 wk), and CV (39°C, 1 wk) vs. CV (39°C, 2 wk), it is evident that the cells tended to proliferate more on the CVs that had a longer vitrification time. Under serum based culture, the keratocytes exhibit a fibroblastic phenotype (**Figure 2.3**E-H). No significant differences in the cellular morphology or proliferation were observed in any of CVs. Nevertheless, these keratocyte fibroblasts maintained their phenotypic markers to varying degrees based on the collagen nanoarchitectures of CVs.

2.3.3. ***Keratocyte gene expression dependence on collagen nanoarchitecture***

Keratocyte gene expression, including keratocan, ALDH, and biglycan, was tested using CVs with different nanoarchitectures. Under serum-based culture, keratocytes lost characteristics of their native phenotype in TCP. Compared to TCP, the gene expression of biglycan was reduced

significantly using all four types of CVs (**Figure 2.6**). For CVs prepared at 5°C, the expression of keratocan was slightly lower using the CV processed for half week than in TCP, but markedly increased when using the CV processed for a longer period of two weeks. The expression of ALDH in cells cultured on both CVs vitrified at 5°C were dramatically increased compared to those cultured on TCP. For CVs prepared at 39°C, the expression of ALDH was slightly lower when employing CV vitrified for one week than that on TCP, but markedly increased when using CV vitrified for a longer period of two weeks. The expressions of keratocan in cells using both CVs prepared at 39°C were greatly raised compared to those using TCP.

2.4. Discussion

Vitrification provides a convenient means to manipulate the nanoarchitecture of collagen membranes. Lamellar structures were formed in these vitrified collagen membranes. During vitrification, collagen fibril density was dramatically increased, which led to a decrease of fibril-to-fibril distance and contributed to the enhanced transparency and mechanical properties reported previously[35]. In addition, fewer collagen fibrils with large bending curvature were observed in the CVs prepared under longer vitrification times, indicating that the collagen fibrils became stiffer during vitrification. This may be explained by new and/or more stable interactions formed in the collagen fibrils through the vitrification process, which is consistent with our previous results showing increased thermal stability of CVs with vitrification time[35,61]. No significant difference was observed in the collagen fibril dimension and periodic banding distance. The maintenance of collagen banding periodicity suggests that the CVs were not denatured during the vitrification process, even under the high temperature of 39°C that is above the normal human body temperature range. This is because the denaturing temperatures of these CVs we observed previously were between 54 and 59°C, much higher than the CV processing temperature[35]. The processing of collagen membranes by vitrification likely resembled, to some extent, the collagen maturation in embryonic corneal stromal development because condensed collagen lamellae composed of

collagen fibrils were formed with new and stable interactions[43]. The flexibility in collagen ultrastructure of CVs provided a vehicle to investigate the effect of nanofibrillar matrix on cellular responses. In this study, the organized collagen membranes supported the growth of keratocytes in serum-free medium when cells generally do not proliferate. On the other hand, cells proliferating under serum-based culture on the CVs were able to maintain a keratocyte phenotype instead of dedifferentiating into fibroblasts. CVs prepared using longer vitrification times were preferable, as they offered an extracellular environment that more closely mimicked the natural corneal stroma. Human corneal stroma has been reported to consist of collagen fibrils with a diameter of 36 nm at a high density of about 700 fibers/mm2[62]. In our study, the highest collagen fibril density in the four CVs studied almost reached a maximum of 180 fibers/mm2, assuming no fibril-fibril spacing. Our fibril diameter, at about 80 nm or above (Fig. 2), was more than twice that in naturally occurring corneal stroma. Thus, creating a further increase in collagen fibril density will require significantly reducing the collagen fibril diameter. Collagen fibril condensation could also be achieved by plastic compression of conventional collagen gels, but to an even lesser degree as compared to vitrification[50].

Quantitative analysis of the effect of collagen nanoarchitecture on keratocyte phenotype is a potentially powerful method to correlate cell morphology and gene expression/phenotype. No systematic studies have been reported in which the effect of different extracellular environments on the keratocyte phenotype was quantified. This is important when designing and testing new biomaterials for corneal reconstruction. We found that the secondary protrusions of keratocytes played a critical role in defining the phenotype. In contrast, their primary protrusion numbers remained constant at different CV processing conditions. Both total protrusion number and length increased significantly with increased vitrification time. This suggests that the collagen membranes consisting of highly condensed collagen fibrils provided a proper environment for the formation of characteristic dendritic morphology of keratocytes. Keratocytes also maintained their phenotype

characteristics in CVs under serum-based culture. Typically, primary keratocytes express a low level of biglycan, but high levels of keratocan and ALDH. In particular, keratocan is one of the four proteoglycans found in the adult corneal stromal ECM that plays an important role in maintaining fibrillar ECM nanostructures and stromal transparency[43]. ALDH is the main water-soluble protein in mammalian corneas and provides protection against ultraviolet radiation and reactive oxygen-induced damages in ocular tissues[63]. In contrast, biglycan is a sensitive marker that is associated with the fibroblastic transition of the keratocytes during pathological remodeling of the corneal stroma[46]. Both down-regulation of biglycan and upregulation of keratocan and ALDH were observed using CVs, especially in those with longer vitrification times. The CVs prepared at 5°C promoted gene expression of ALDH higher than of keratocan, whereas the CVs prepared at 39°C favored the up-regulation of keratocan more than of ALDH. This may result from different types of interactions that were formed between the collagen molecules during the vitrification process at different temperatures, which is a unique phenomenon observed in collagen processing. Many techniques have been reported to manipulate collagen organizations. For instance, collagen matrix stiffness has been modified by changing collagen concentration[64], tuning crosslinking density[65,66], or employing a compressive load[52]. Collagen fibril alignment has been controlled by applying a shear force[49,67].

Nevertheless, none of these techniques mimic the process of collagen maturation as observed in vitrification of collagen membranes showing continuous formation of new interactions between collagen molecules inside collagen fibrils. The utility of vitrification processing to tailor the nanoarchitecture of ECM or biomimetic biomaterials may be useful for various clinical applications. For instance, keratoconus is a disease where the corneal stromal matrix becomes disrupted and loses this fine structural organization. The application of local vitrification in the diseased cornea might offer a route to reorganizing the stromal matrix and eliminating corneal protrusion. In addition, the CV with a biomimetic collagen nanoarchitecture holds great potential

as a corneal substitute that supports the growth of keratocytes and preserves the cellular phenotype. Similar biomaterials can also be designed to use as potential substitutes for other connective tissues such as cartilage, skin, and muscle.

2.5. Conclusion

This study fabricated CVs with unique engineered biomaterial scaffolds that provided an ex vivo template mimicking the native environment of corneal stroma. The well-organized collagen matrices developed in CVs were obtained through a highly controlled vitrification processing method. This collagen vitrification process resembled, to some extent, the normal collagen maturation in corneal stroma. This processing technique also provided collagen scaffolds with variable nanoarchitectures that may offer a method to study collagen degeneration and thereby be helpful in elucidating the etiology of the diseases related to a changing ECM. As illustrated in this study, the highly condensed collagen matrices in CVs allowed the proliferation of keratocytes, even without serum; and with serum, they helped to maintain the characteristic phenotypes of the cells. We suggest that with further development, CVs may be used to create a corneal substitute and guide corneal repair by placing an acellular scaffold into a defect, and allowing migration of the patient's cells into this nanostructure.

Table 2.1 RT-PCR Primer Sequences.

Gene	Sequence (5′-3′)	Annealing temp (°C)
ALDH		60.4
Forward	GGAAGCCATCCAGTTCATCA	
Reverse	GTCTCCGCGATCATCTTCTT	
Biglycan		62.4
Forward	ACCTCCCTGAGACCCTCAAT	
Reverse	TTGTTGTCCAAGTGCAGCTC	
Keratocan		60.4
Forward	TGACCTGCAGCACAATAAGC	
Reverse	TGAGTCTCAGGAAGGCCACT	
GAPDH		62.4
Forward	GGGTCATCATCTCTGCACCT	
Reverse	GGTCATAAGTCCCTCCACGA	

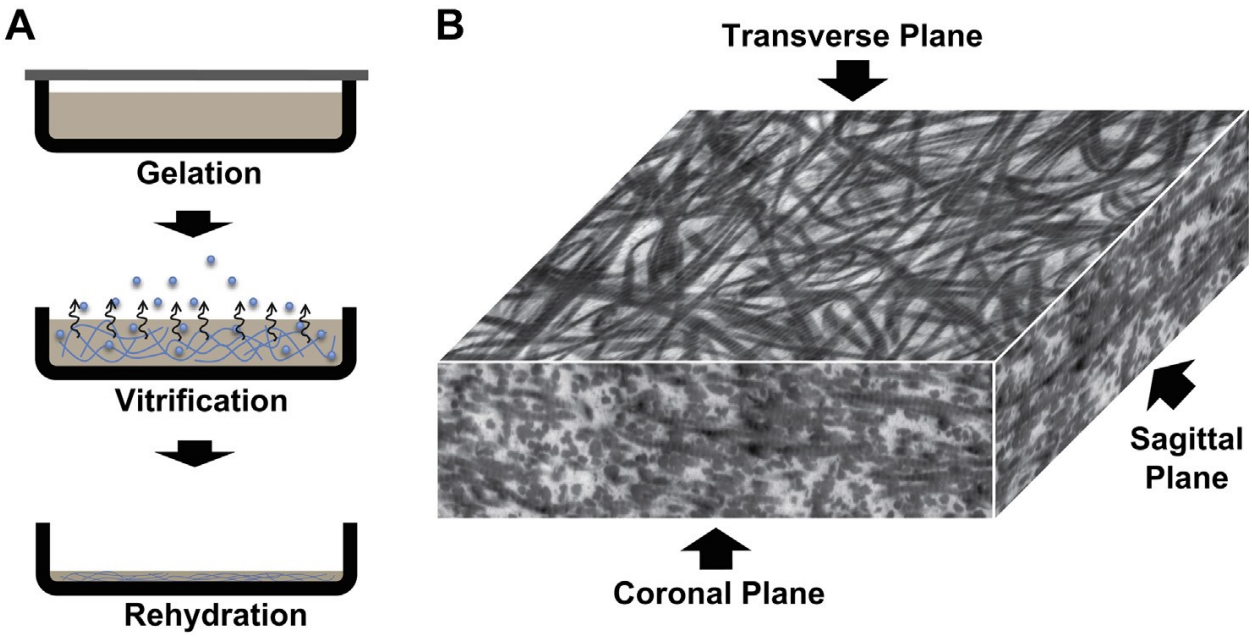

Figure 2.1 Collagen vitrigel preparation and alignment: (A) three-step procedures, and (B) TEM image of CV central portions showing 2D alignment of matured collagen fibrils by vitrification.

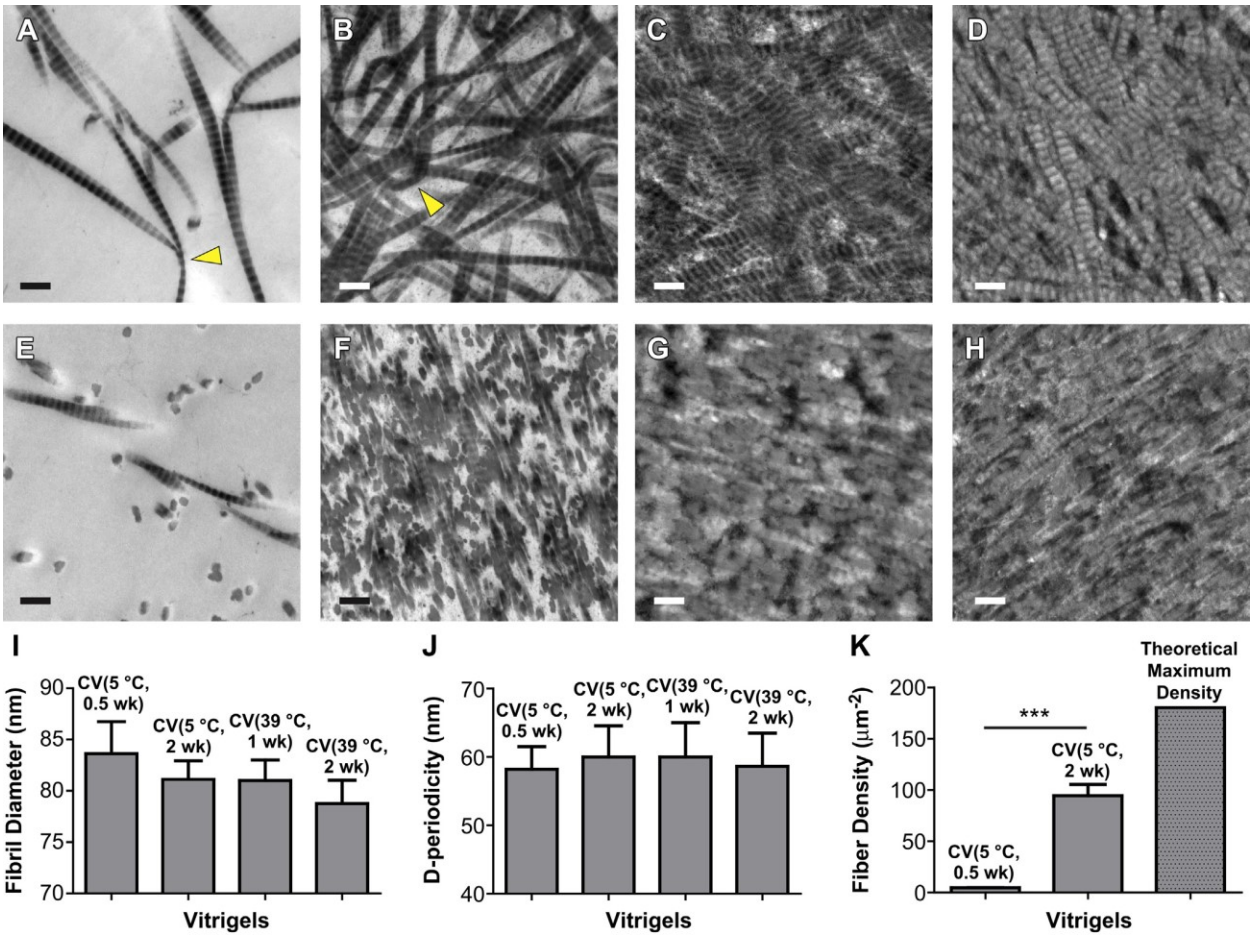

Figure 2.2 TEM images of CVs and collagen fibril analysis: (A-D) Transverse plane, (E-H) coronal plane, and (I-K) collagen fibril analyses. Four CVs were used: (A, E) CV 5°C, 0.5 wk, (B, F) CV 5°C, 2 wk, (C, G) CV 39°C, 1 wk, and (D, H) CV 39°C, 2 wk. Collagen fibril analyses include (I) fibril diameter, (J) d-periodicity (banding), (K) fibril density. The TEM samples were obtained from the center portions of the collagen membranes. Collagen fibrils with large bending curvature were indicated by triangle. The error bars in (I, J) represent the standard deviation of the mean. Scale bar in (A-H): 200 nm. ***$p < 0.001$.

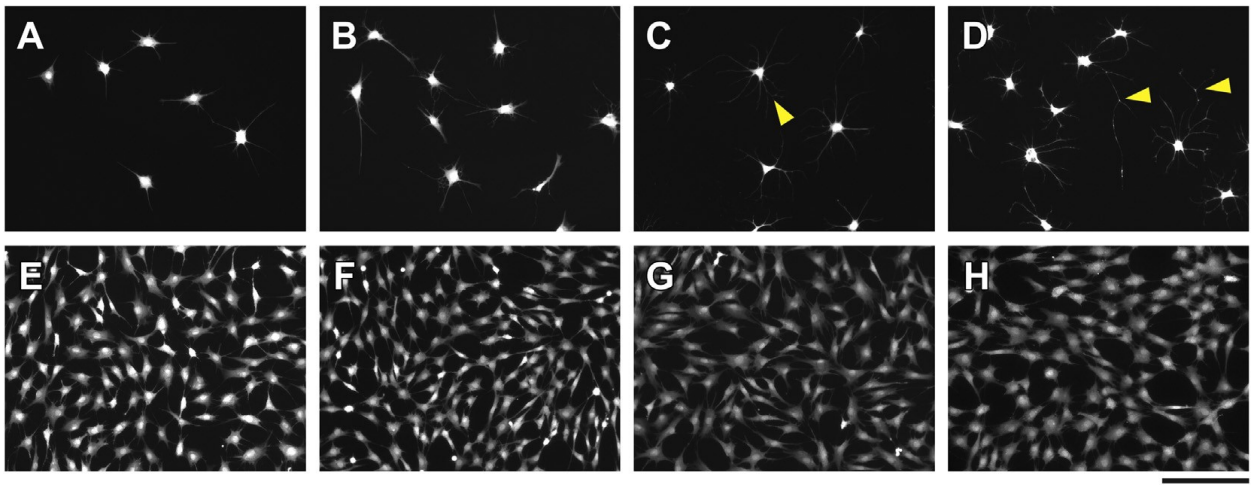

Figure 2.3 Keratocyte morphologies cultured on CVs using two different culture media: (A-D) serum-free culture medium, and (E-H) culture medium with 10% FBS. Four cell culture substrate conditions were used: (A, E) TCP control (B, F) CV 39°C, 1 wk, (C, G) CV 39°C, 2 wk, and (D, H) CV 39°C, 8 wk. Pinning points in cell extensions were highlighted by triangle. Scale bar: 200 mm.

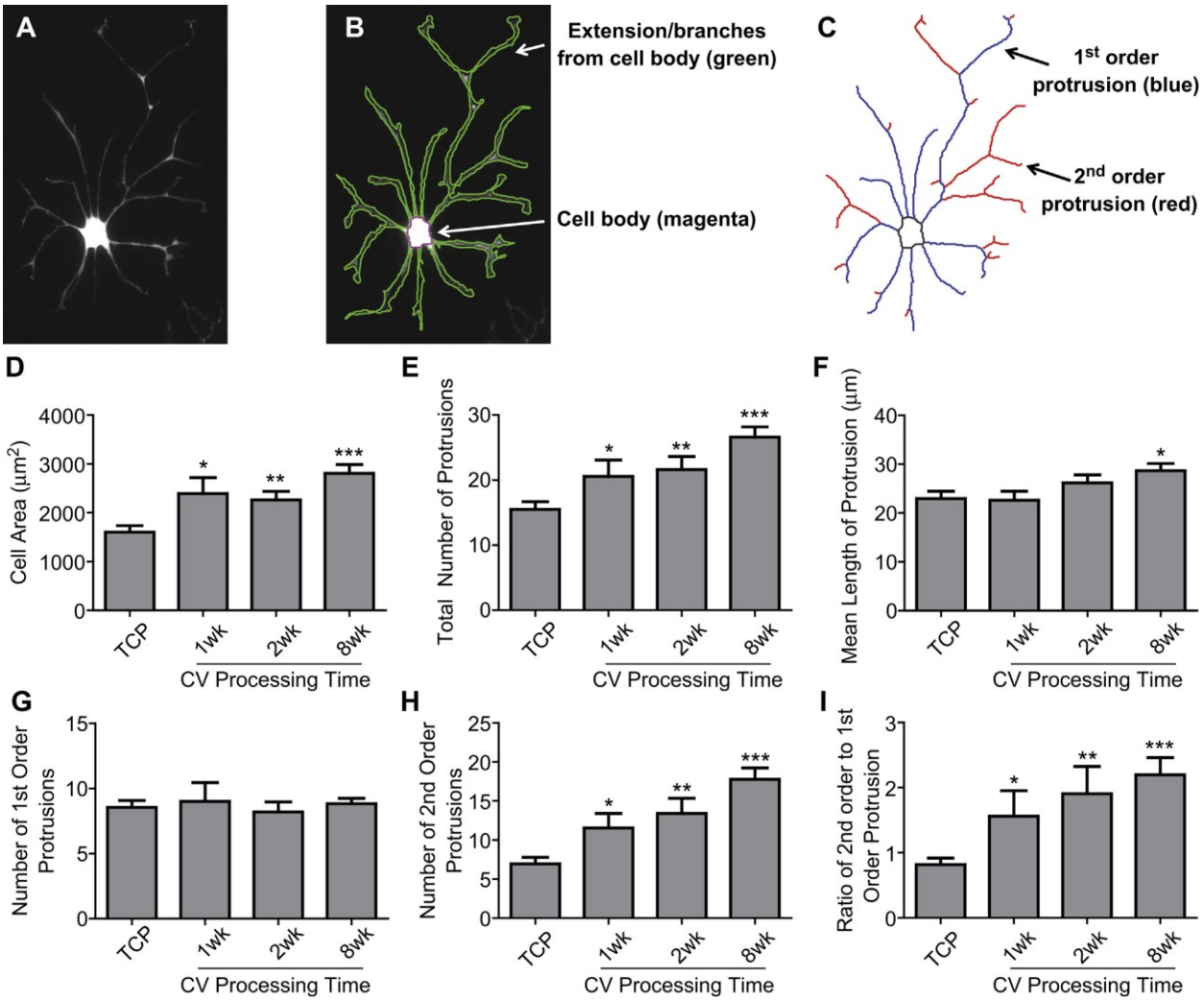

Figure 2.4 Morphological analysis of keratocytes cultured on CV vitrified at 39°C using serum-free medium. (A-C) A keratocyte example cultured on CV (39°C, 8 wk) (A) with cellular contour identified in (B) and morphological skeleton acquired in (C). Based on cellular contour and skeleton, the dependence of keratocyte morphologies on CV vitrification processing time was examined (D-I), including cell size (D), total number of protrusions (E), mean length of protrusions (F), primary protrusion number (G), secondary protrusion number (H), and the ratio of secondary to primary protrusions (I). The error bars in (D-I) represent the standard deviation of the mean. Keratocytes cultured on the TCP were tested as a control. All statistical differences against the TCP control are indicated. *$p < 0.05$, **$p < 0.01$, ***$p < 0.001$.

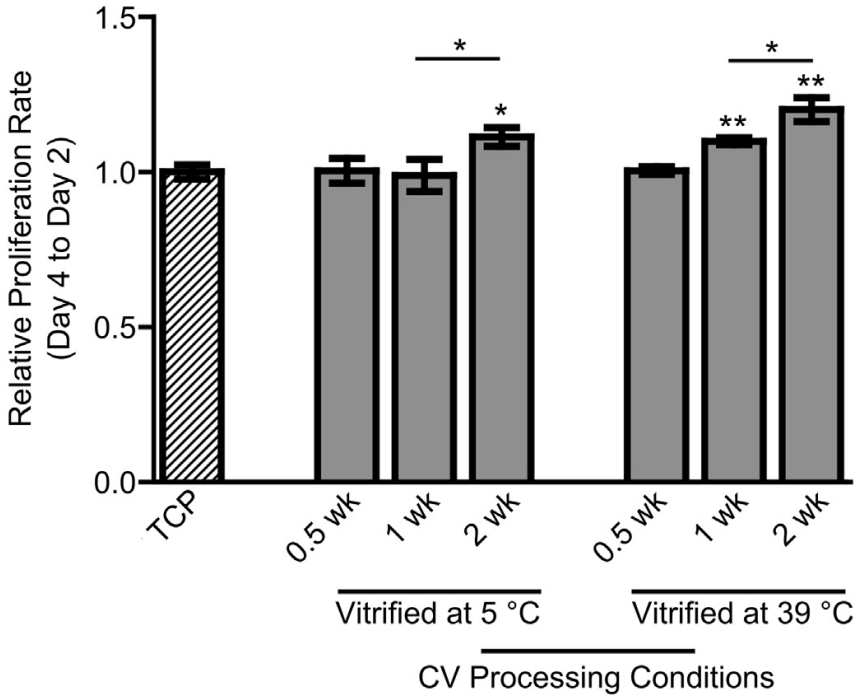

Figure 2.5 Effects of CV processing conditions on the proliferation of primary keratocytes cultured in serum-free medium. The CVs were processed from 0.5 wk up to 2 wk at two different temperatures (5°C and 39°C). The proliferation of keratocytes at Day 4 relative to Day 2 was assessed using an AlamarBlue assay and normalized by the TCP control. *$p < 0.05$, **$p < 0.01$.

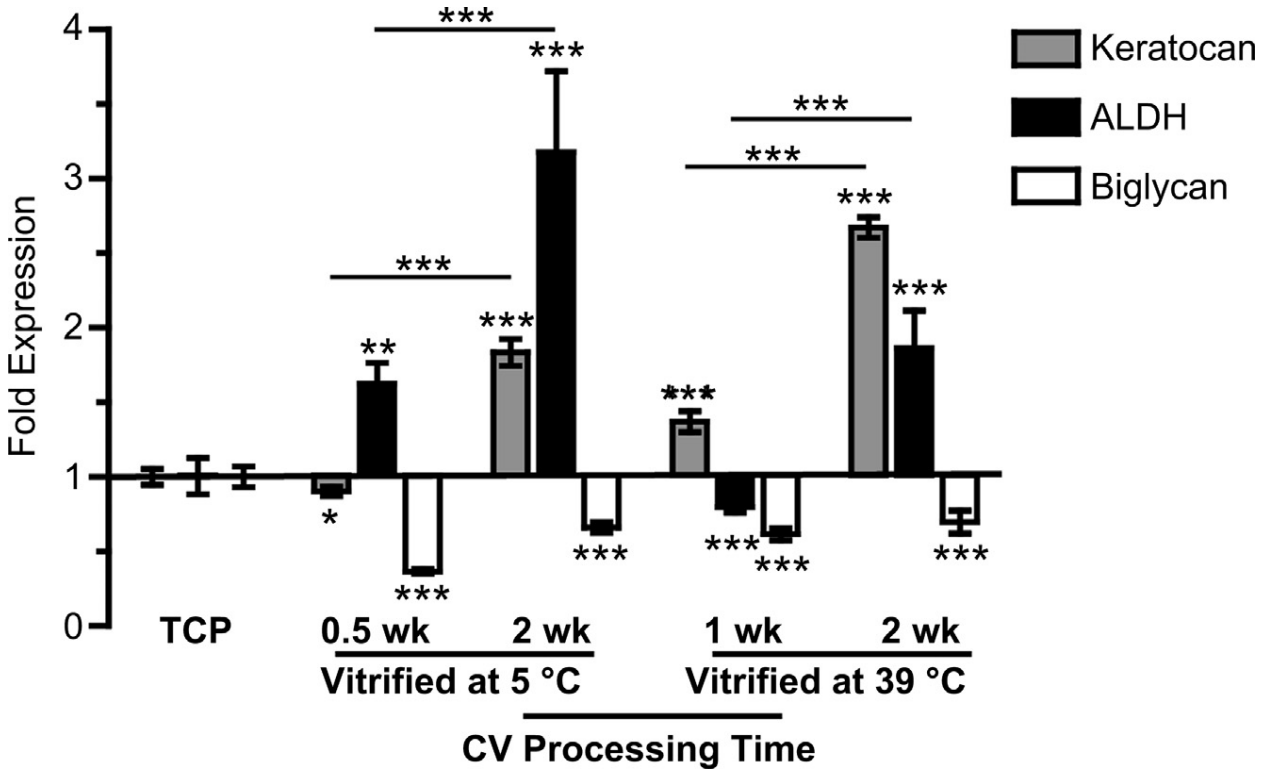

Figure 2.6 Gene expression of keratocytes fibroblasts seeded on CVs processed under different conditions and cultured in serum-based medium. All statistical differences are indicated with the ones against TCP control showing above each bar, and the others comparing CV groups portrayed on lines. *$p < 0.05$, **$p < 0.01$, ***$p < 0.001$.

3. Tissue Derived Extracellular Matrix stabilizes ectatic corneal biomechanics and ultrastructure[2]

3.1. Introduction

The cornea is the outermost layer of the eye, which functions as a protective and light-refractive tissue. Corneal stroma represents about 90% of the corneal in thickness, composed of a collagen-rich extracellular matrix (ECM) with highly aligned collagen fibrils formed densely packed lamellae [68]. This unique ultrastructure provides excellent transparency and mechanical stability to the cornea. Diseases or injuries of the cornea that cause changes in the ultrastructure negatively impact corneal mechanical and optical properties. Corneal ectasia, and more specifically keratoconus, is an ocular disorder caused by abnormal collagen degeneration that leads to weakening of the corneas, irregular astigmatism and vision loss [69]. The ultrastructural damage and disrupted collagen alignment in keratoconic eyes has been previously established [70,71]. The FDA approved clinical treatment to slow or halt the progression of keratoconus or post-LASIK ectasia is photochemical collagen crosslinking initiated by riboflavin (RF) under ultraviolet-A (UVA) irradiation [72]. While this high efficacy procedure significantly improves the mechanical characteristics of the corneas after treatment [73], exposure to UVA holds some risks. Prolonged UVA irradiation can cause extensive keratocyte loss or even corneal endothelial cell damage [74,75]. This method is therefore not suitable for patients with thin corneas (<280 μm).

As part of the natural aging process, corneal crosslinking occurs via the Advanced Maillard Reaction [76], which involves proteoglycan components in the cornea. Further, during prenatal corneal development and corneal wound healing, other ECM components such as proteoglycans

[2]Text and figures from this chapter adapted from a currently unpublished manuscript with permissions from authors. H. Yin*, X. Wang*, S. Majumdar, J. Sohn, W. Stark, J.H. Elisseeff, Tissue Derived Extracellular Matrix stabilizes ectatic corneal biomechanics and ultrastructure.

play an important role to regulate corneal fibril size and spacing, which has a critical impact on corneal optical and mechanical properties [77,78]. It has been reported that ECM proteins such as the decorin core protein, can reinforce porcine corneas *ex vivo* [79]. ECM is a collection of biological molecules secreted by the cells carrying structural and biological cues to regulate cellular activities. In regenerative medicine, ECM is typically used in the context of scaffolds for tissue engineering [80,81], and porcine bladder-derived ECMs are already available clinically as wound care products [82]. However, the functions of ECM surpass mere structural support, providing key biological cues to regulate cell behavior such as proliferation, migration and differentiation [83,84]. We have also recently demonstrated that ECMs exhibit an immune-regulatory role through the T-cell pathway in a mouse volumetric muscle loss model [85]. Tissue derived ECM materials such as amniotic membranes also have been applied in ophthalmological research, used for wound healing or as cell carriers for limbal stem cell deficiencies [86,87]. However, very few studies have focused on the impact of ECM on corneal biomechanics. To bridge this gap in literature, in our present study we evaluate the effect of tissue-derived ECMs on the reinforcement of corneal biomechanics and extent of restoration of native collagen ultrastructure in damaged corneas. We produced ECM microparticles from multiple organ sources, and studied their effect on an established enzyme-mediated *ex vivo* keratoconus model [88].

3.2. Materials and Methods

3.2.1. ***ECM conditioned medium preparation***

Porcine eye globes, knee joints and lymph nodes were purchased from local slaughter house. Corneas (COR) from the eyes, cartilage (CART) from the knee joints, and lymph node (LN) tissue were dissected from adjoining tissue. The tissues were thoroughly washed with tap water and frozen before decellularization. Using a standard decellularization process, the tissues were thawed and ground with knife mill, followed by treatment with 3% peracetic acid (Sigma Aldrich) on a stir

plate for 4 hours (500 ml 3% peracetic acid per 20 g of minced tissue). After acid treatment, the minced tissue was washed extensively with tap water followed by deionized (DI) water until the pH was neutralized. The samples were then treated with 5% Triton-X for 48 hours, followed by a final digestion with DNase (Roche) overnight. The decellularized minced tissue was lyophilized and then cryomilled into microparticles before use. To prepare ECM conditioned media, the ECM microparticles were suspended in full media (DMEM+10% FBS+1% antibiotic-antimycotic) at concentration of 1 mg/ml overnight, and then filtered through a 0.22 μm filter before use.

3.2.2. ***Ectatic corneal (KC) culture in ECM conditioned media***

Fresh albino rabbit eyes (Cat. #41211-2) were purchased from PelFreez Biologicals (Rogers, AR). To create the *ex vivo* keratoconus model (KC) corneas, the eyes were treated with 0.1 U/ml chondroitinase ABC (C36675U Sigma Aldrich) by immersing the anterior surface in enzyme solution for 2 hours. Following enzyme treatment, the eye globes were washed with full media several times. The corneas were then treated to the different ECMs, by submersing the anterior segment in ECM containing 4% dextran for 18 hours.

3.2.3. ***Optical coherent tomography (OCT)***

The *ex vivo* eye globes were imaged with Envisu R4110 SDOCT system (Bioptigen) with light source with an output power of 10 mW, and an effective bandwidth of 105 nm centered at 845 nm, which provides an axial resolution of 3.0 μm in air for the experiment. The transversal resolution is approximately 12 μm, assuming a Gaussian beam profile. The scanning area of each cornea had a width of 4.8 mm and depth of 1.2 mm.

3.2.4. ***Transmission electron microscopy***

Samples before and after ECM treatment were stored in 20% Dextran-500 overnight to minimize any swelling effects before fixation. The fixative contained 3% paraformaldehyde, 1.5%

glutaraldehyde, 5 mM $MgCl_2$, 5 mM $CaCl_2$, 2.5% sucrose, 0.1% tannic acid in 0.1 M sodium cacodylate buffer, at pH 7.2. Samples were fixed overnight at 4°C, then post-fixed in 1% osmium tetroxide, followed by staining with 2% aqueous uranyl acetate and dehydrated in increasing concentrations of ethanol (from 30% to 100%). Thin sections (60-90 nm) were cut and stained with lead and uranyl acetate. Sections were observed with Philips/FEI BioTwin CM120 Transmission Electron Microscope at 80kV.

3.2.5. ***Image analysis:***

TEM images were analyzed using MATLAB program, using code that was previously established [88]. Original images were binarized using an adaptive thresholding method. To estimate the density of fibers, a window of fixed size (300x300 dpi) was randomly localized. Within the window, the density (i.e. the number of fibers per unit area) was measured and recorded. This random procedure was repeated 200 times and the density of fibers was estimated using the median number.

3.2.6. ***Tensile test***

Uniaxial tensile testing was carried out to determine the stress-strain behavior of the corneas before and after ECM treatment. All samples for tensile testing were stored in 20% dextran-500 solution overnight to minimize swelling. Corneas were cut into 5 mm stripes, and the thickness of the stripes was recorded. Superglue was used to fix both ends of the corneas to sample clamps to avoid slippage. The tensile test was performed at the rate of 0.01 mm/s on Bose EnduraTEC ELF3200 using a 2 N load cell. Load and displacement were recorded by software WinTest.

3.2.7. ***Differential scanning calorimetry (DSC)***

The thermal stability of the corneas was assessed using the DSC 8000 (Perkin Elmer, Waltham MA). Three corneal samples from each treatment group were obtained using a 6-mm biopsy punch

and placed in 30 μL aluminum pans and crimp-sealed. An empty pan was used as reference in all samples. DSC was performed over a temperature range of 10°C to 95°C, at a rate of 5°C per minute under a 20 mL/min nitrogen flow. Denaturation temperatures were detected and analyzed with the Pyris software (Perkin Elmer) version 10.1.

3.2.8. ***Gene expression***

Corneas were flash-frozen in liquid nitrogen and broken into small segments using ceramic pestles. The corneal segments were treated with TRIzol (ThermoFisher) and the total RNA was collected with RNeasy Mini Kit (Qiagen). The mRNA concentrations were quantified by Nanodrop-1000 spectrophotometer (NanoDrop Technologies, Wilmington, DE), and then reverse-transcribed with High Capacity cDNA kit (Applied Biosystems). QPCR was performed with SYBR Green qPCR Mastermix (Applied Biosystems), and expression levels were normalized using housekeeping gene *Gapdh*. The primers of the targeted genes are listed in Table 3.1.

Table 3.1 Gene primers used to assess gene expression in ECM treated corneas.

Gapdh	Forward	5’-CTCTGGAGTGGATGTT-3’
	Reverse	5’-CCATGGGTGGAATCATACTG-3’
Tnfα	Forward	5’-GTAGTAGCAAACCCGCAAGT-3’
	Reverse	5’-GGTTGTCCGTGAGCTTCAT-3’
Keratocan	Forward	5’-AGTACCAACAAGCTTCAGCC-3’
	Reverse	5’-ACCCAGATGACGAAACATATT-3’
Aldh	Forward	5’-GACGATAACTGCAGAGCACG-3’
	Reverse	5’-ACTCATTCGACAAGCAGACAG-3’
Biglycan	Forward	5’-GCATCCCCAAAGATCTGCC-3’
	Reverse	5’-CAACTTGGAGTATCGGAGCAG-3’

*3.2.9.**Statistical Analysis***

Student's t-test was used to statistically examine differences between control, KC and ECM treated corneas in terms of collagen fibril diameter and density. Young's modulus, and gene expression were analyzed with Prism 6.01 (GraphPad Software, Inc., San Diego, CA) using one-way analysis of various (ANOVA). All experiments were repeated twice independently, with n=6 for each experimental group. P-values <0.05 were considered statistically significant.

3.3. Results

To determine the potential use of ECM treatment as an alternative to photo-crosslinking, we first enzymatically induced corneal weakening and degradation to simulate corneal ectasia and then treated the KC eyes to various ECM conditioned media to demonstrate restorative effects of ECM (**Figure 3.1**). We characterized changes in the corneas in terms of mechanical characteristics, thermal properties, ultrastructural organization and gene expression both pre- and post-treatment.

*3.3.1.**Corneal structural changes after ECM treatment***

As a convenient and non-invasive technique to visualize corneal cross sections, OCT was used to measure changes in thickness and light scattering after enzyme digestion and ECM treatment (**Figure 3.2**). Unwounded control corneas cultured in full medium (without ECM) for 18 hours, were measured at a thickness of around 500-600 μm. The typical rabbit corneal thickness is 350-370 μm, therefore despite presence of 4% dextran-500 in the culture medium, a certain extent of corneal swelling *ex vivo* is expected. Corneas after enzyme digestion (KC), despite the lower collagen/proteoglycan content, demonstrated thicknesses comparable to control cornea and hyper-reflection of light in the OCT images, indicating extensive swelling and reduced transparency after KC treatment. KC corneas which were treated with ECM however did not show the same swelling behavior and presented lower thickness values. ECM treated corneas also did not demonstrate the

hyper-reflection seen in KC corneas. Particularly, light reflection in the OCT images of the COR corneas was markedly similar to unwounded control corneas.

TEM was used to identify changes in collagen fibril density of the KC corneas before and after ECM treatment (**Figure 3.3**). Chondroitinase enzyme activity on the KC corneas degraded proteoglycan chains in the cornea, resulting in a lower fibril density compared to unwounded controls. The loss of proteoglycan content also contributed to a larger average fibril diameter, due to swelling during fixation. KC corneas had a larger average fibril diameter, lower fibril density and a similar pattern of fibril distribution compared to unwounded control corneas. Treatment of the KC corneas with ECM significantly increased fibril density, restoring the normal collagen architecture to varying extents. Collagen fibril diameter and density differed with different ECM treatments (COR, CART, LN). In comparison to unwounded controls, the COR group presented smaller median fibril diameter size but a larger fibril diameter distribution, CART group demonstrated similar fibril diameter, and LN group exhibited the smallest fibril diameters. Additionally, the LN group also exhibited the highest collagen fibril density.

3.3.2. ***Corneal mechanical properties and thermal stability after ECM treatment***

Mechanical properties and thermal stability of the KC corneas were evaluated following ECM treatment. Uniaxial tensile testing demonstrated significant reduction in the elastic modulus of KC corneas after enzyme treatment. Following ECM treatment, elastic modulus of the KC corneas is restored and there was no statistical significance between the moduli of different ECM treatments and the unwounded controls (**Figure 3.4**A). Representative stress-strain curves also demonstrate the effect of the reinforcement through ECM treatment at higher strain values (**Figure 3.4**B). Thermograms obtained using the DSC clearly display variations in the denaturation temperatures of control and KC corneas via broad peaks over the 60-70°C range (**Figure 3.4**C). While KC corneas had significantly lower mean denaturation temperatures (mean value+/-°C) as compared

to the control corneas (mean value+/-°C), the ECM treatment restored thermal denaturation temperatures in all three groups (**Figure 3.4**D).

3.3.3. ***Gene expression***

To evaluate the impact of various treatments on corneal stromal cells, qRT-PCR was performed on the corneas following culture in ECM conditioned media (**Figure 3.5**). The enzyme digestion significantly upregulated the pro-inflammatory marker *Tnfa* in KC corneas. In contrast, after KC corneas were treated with ECM conditioned media, *Tnfα* expressions were significantly down-regulated to levels lower than control group. Keratocyte markers *keratocan*, *Aldh* and *biglycan* were also evaluated. KC groups demonstrated significant down-regulated expression of all keratocyte markers evaluated. Following treatment of KC corneas with ECM conditioned media, key keratocyte marker expressions were restored.

3.4. Discussion

ECM proteins are known to play a significant role in the maintenance and preservation of tissue ultrastructure and biological function. This study investigates the potential application of leveraging these roles of ECM for structural reinforcement of the cornea to tackle the clinically relevant challenges of corneal ectasia. We evaluated the benefits of ECM via biomechanical, thermal, ultrastructural and gene expression characterization, by treating enzyme digested corneas with ECM conditioned media. ECM treatment demonstrated an increase in Young's modulus on the KC corneas. Moreover, it restored thermal stability, and regulated gene expression of corneal stromal cells. We have therefore conclusively established that tissue-derived ECM can significantly and beneficially impact corneal mechanics, stability and cell behavior.

Rabbit corneas are prone to swelling immediately post-enucleation, despite intact epithelial and endothelial cell layers. The swelling is exacerbated if any damage to the collagen structure occurs.

The enzyme chondroitinase ABC specifically targets chondroitin sulfate, which is a glycosaminoglycan in the cornea, thereby weakening the collagen-proteoglycan ECM network in the corneal stroma. Therefore, after enzyme digestion, KC corneas contain a lower collagen/proteoglycan content. Despite the collagen/proteoglycan loss, the average thickness of modeled KC corneas was comparable to unwounded control corneas. Additionally, hyper-reflection of light in the OCT images was observed in KC corneas. Both these findings indicate extensive swelling occurred after enzyme digestion, disrupting the collagen/proteoglycan organization of the stroma. ECM treatment of KC corneas demonstrated a decrease in overall thickness and in the hyper-reflection compared to KC corneas, indicating stabilization of the corneal stromal architecture. TEM images also demonstrated that ECM treatment of KC corneas restored damaged ultrastructure and significantly condensed the collagen fibril spacing. The increase in collagen density corresponded with the reduction in thickness observed from the OCT images. In the native cornea, the proteoglycans containing chondroitin sulfate chains plays an important role on regulating collagen size and inter-fibrillar spacing [43]. In this *ex vivo* model, KC corneas have larger inter-fibrillar spacing and fibril diameter, which could be attributed to the degradation of chondroitin sulfate chains via enzymatic action, thus weakening inter- and intra-fibrillar collagen binding. The loss of inter-fibrillar collagen binding results in lower collagen fibrillar density. Meanwhile, the weakened intra-fibrillar collagen binding causes loosening of the tight packing in individual collagen fibrils, thereby changing the collagen fibril diameter distribution. ECM treatment restored the fibril density and altered the fibril diameter distribution. Treatment with different ECM groups (COR, CART, LN) resulted in different fibril sizes and density distributions. The differences observed after treatment could potentially be attributed to the varying biological components in the tissues from which the ECMs were extracted. While dissimilar in the ultrastructures produced, all ECM treatment groups restored mechanical properties of the cornea equally.

Tensile strength is an important parameter for evaluating crosslinking efficiency, to ensure that the corneal stroma can resist deformation due to intraocular pressure. The enzyme activity decreased the tensile strength of KC corneas due to the degradation of proteoglycans, similar to the loss of mechanical integrity in keratoconic corneas. ECM treatment of the KC corneas increased the Young's moduli in all ECM treated groups by 50% compared to the untreated KC group, statistically comparable to the modulus of unwounded controls.

Thermal denaturation temperature of the corneal stroma is another critical characteristic to assess stability of the corneas. Typical type I collagen based tissues have thermal denaturation temperatures ranging from 50-90°C[89], depending on various factors such as other extracellular matrix components and water content . We have previously reported denaturation temperatures of healthy rabbit corneas stored in 20% dextran-500 to be around 70°C[88]. In this study, unwounded control corneas (with 4% dextran-500) denatured at approximately 68°C. The lower dextran concentration allows tissues to possess a higher water content, which in turn drives down the denaturation temperature. Enzyme treatment resulted in significantly lower denaturation temperatures of the KC corneas, indicating the weakening of hydrogen bonds which stabilize the collagen triple helix. COR, CART and LN ECM treatment restored the denaturation temperatures of the treated corneas to the values of unwounded control corneas. This demonstrates that ECM treatment is effective in significantly improving thermal stability of weakened corneas.

Previous studies indicate that pro-inflammatory genes are associated with keratoconus. Balasubramanian SA *et al.* [90] have reported that several pro-inflammatory markers such as *Il-6* and *Tnfα*, and enzymes such as matrix metalloproteinase 9 (*Mmp9*) are elevated in the tear fluids of keratoconus patients. More recently, Pahuja N *et al.* [91] found that inflammatory genes were expressed by the corneal epithelium and stromal keratocytes at the corneal cone apex of keratoconus patients. Moreover, a marked reduction in consecutive enzymes and proteoglycans such as alcohol dehydrogenase (*Aldh*) [92] and *keratocan* [93] was found in cultured keratoconic

stromal cells. Thus, the pro-inflammatory response along with the alteration of keratocyte phenotype plays an important role in the collagen degeneration of the keratoconic stroma. In the field of regenerative medicine, ECM components have been shown to impart certain biological cues when used as scaffolds, to help with regulating inflammatory response [85] or promoting local cell differentiation and maintaining phenotypes [83]. In our current study, we demonstrated that ECM treatment is also beneficial to the cellular environment of the corneal stroma. ECM treatment significantly down regulated the pro-inflammatory marker *Tnfα*, enhanced the *Aldh* production and maintained the *keratocan* and *biglycan* levels in the *ex vivo* organ culture corneas. In contrast to photochemical crosslinking which causes keratocyte apoptosis and potential damage to the endothelium, an ECM based corneal crosslinking treatment which reinforces corneal biomechanics while reducing inflammation and helping maintain healthy keratocyte phenotype in the stroma has the potential to be of significant value for keratoconus patients.

3.5. Conclusion

We studied the crosslinking effects of ECM microparticles in culture media on corneas. ECMs from three distinct tissue types - cornea, cartilage and lymph nodes - all significantly enhanced corneal biomechanics, thermal stability and reduced swelling. However, ECMs from different organs affected corneal ultrastructure and gene expression differently. Thus, in future studies, the biological impact of a variety of different tissue sources will be investigated. In summary, we demonstrate that ECMs alone can significantly improve corneal biomechanics to provide reinforcement for ectatic symptoms in corneas with potential additional biological benefits of reduced inflammation and maintenance of healthy phenotypes. These findings demonstrate the benefits of tissue-derived ECM microparticles and demonstrate a potential application as biological crosslinkers to treat or prevent corneal ectasia.

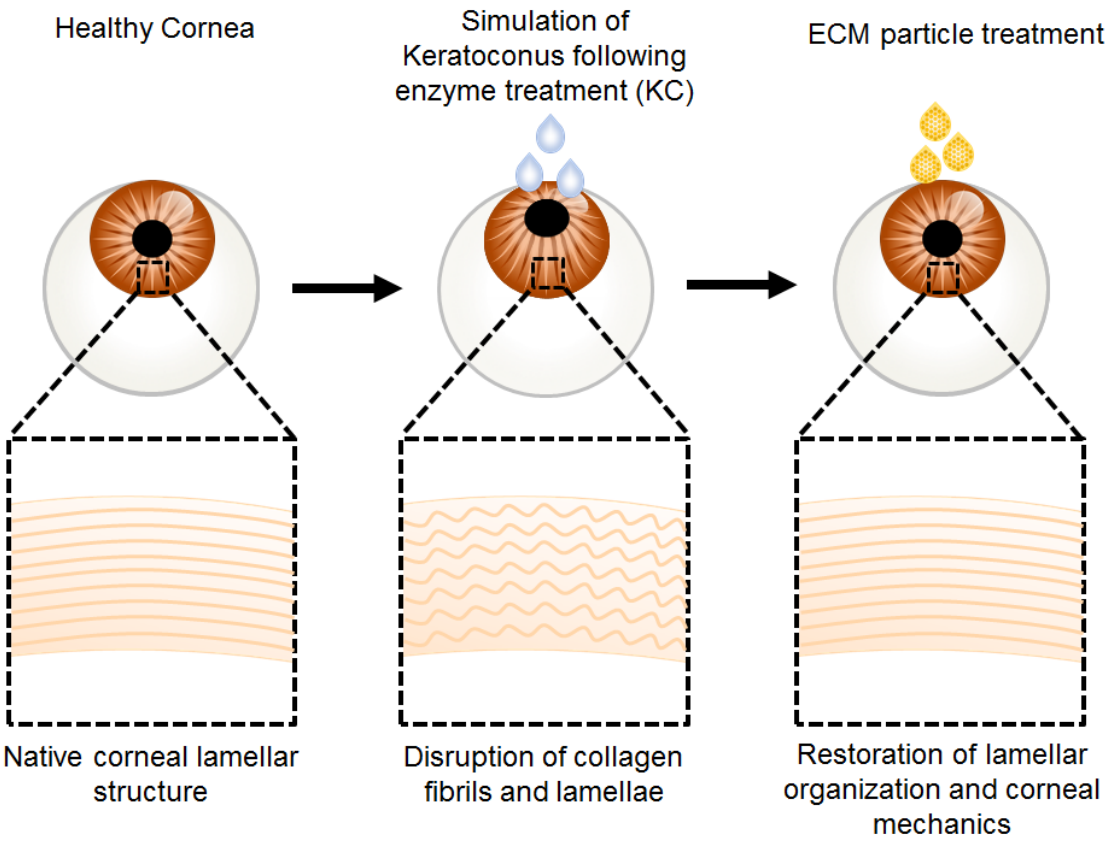

Figure 3.1 Schematic demonstrating ECM treatment and effect on cornea ultrastructure. Enzymatically induced corneal weakening and degradation to simulate corneal ectasia followed by treatment of KC eyes to various ECM conditioned media to demonstrate restorative effects of ECM.

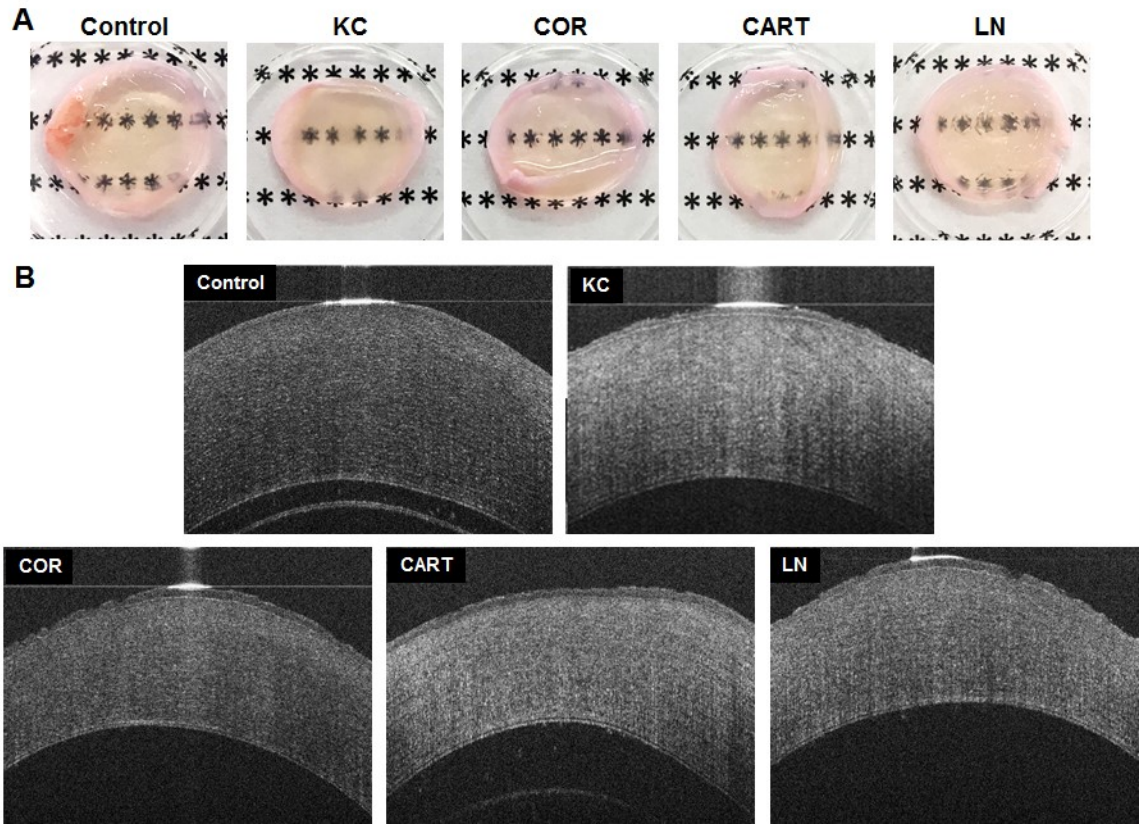

Figure 3.2 Gross changes observed following ECM treatment. A) Gross pictures of rabbit corneas subjected to various ECMs and the effect of treatments on clarity of the corneas. B) OCT images to determine changes in thickness and hyper-reflection of the corneas post-treatment.

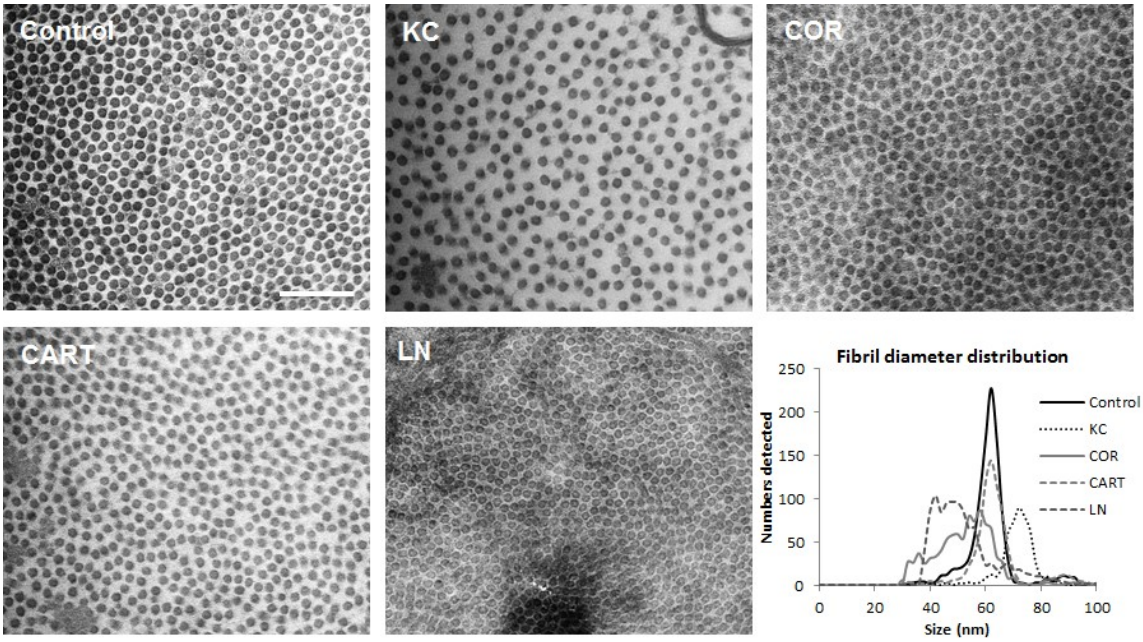

Figure 3.3 Changes in fibrillar packing of corneal collagen. Visualization of collagen fibril density of unwounded control corneas, enzymatically degradaded KC corneas and ECM treated KC corneas through transmission electron microscopy,with accompanying graph showing results of calculation of fibril diameter distribution after each treatment.

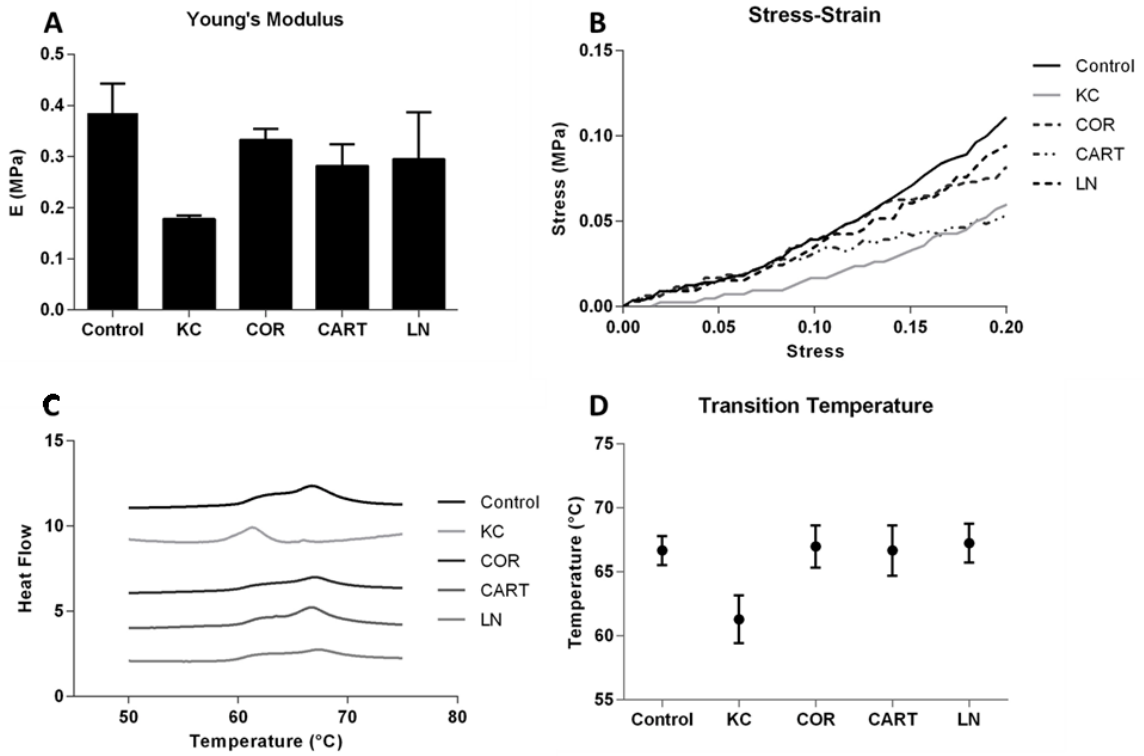

Figure 3.4 Influence of ECM treatment of physical and thermal properties of cornea. A) Visualization of collagen fibril density of unwounded control corneas, enzymatically degradaded KC corneas and ECM treated KC corneas through transmission electron microscopy,with accompanying graph showing results of calculation of fibril diameter distribution after each treatment.

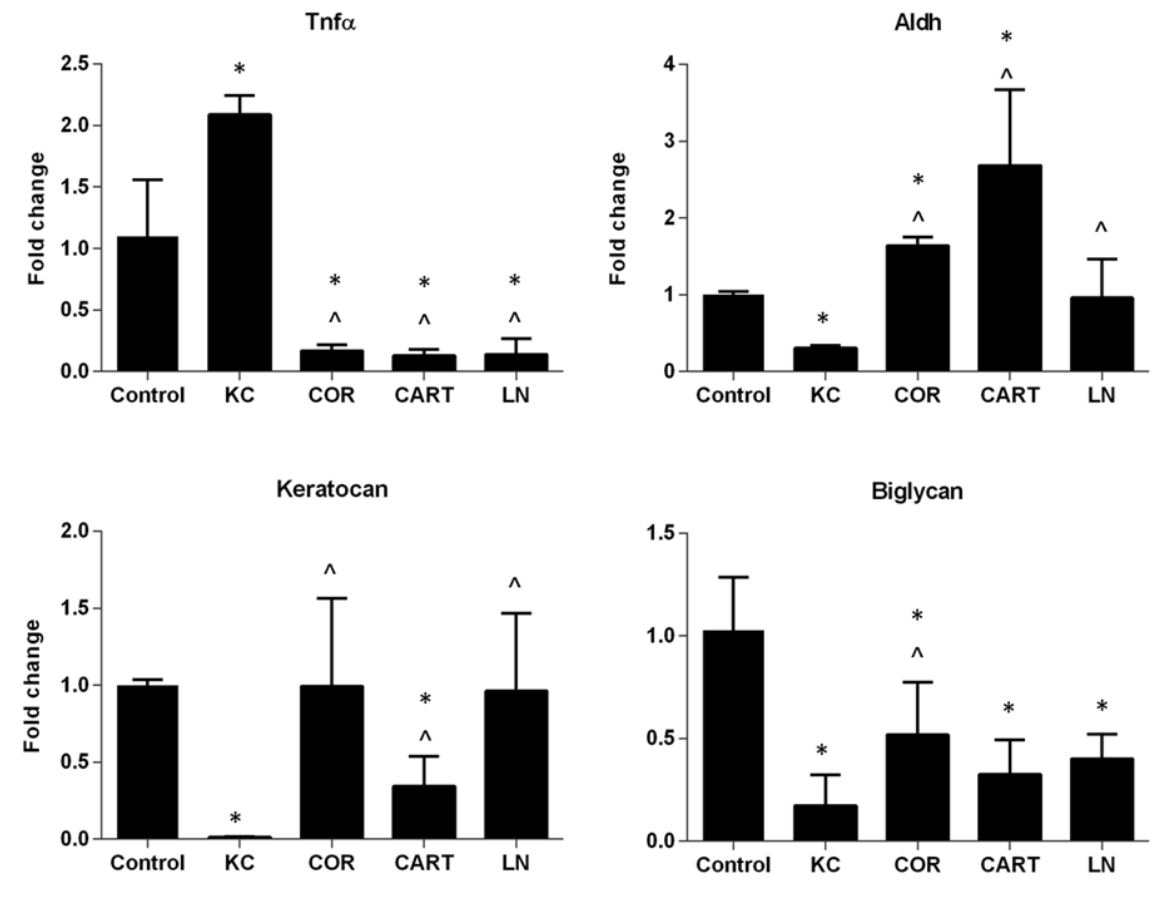

Figure 3.5 Gene expression of keratocytes after crosslinking. Inflammatory marker Tnfα, keratocyte markers Aldh, Keratocan and Biglycan were evaluated among normal, KC and ECM treated corneas. N=6 in each group, * refers to $p<0.05$ compared to normal corneas, and # refers to $p<0.05$ compared to KC corneas.

4. Chondroitin Sulfate-based Biocompatible Crosslinker Restores Corneal Mechanics and Collagen Alignment[3]

4.1. Introduction

Corneal ectasia is a corneal disorder characterized by progressive corneal axial thinning, which results in irregular astigmatism and decreased vision[94]. The progression of corneal ectasia is more rapid in younger patients and greatly impairs vision and quality of life[95]. Corneal ectasia may result from corneal diseases, for example keratoconus (KC), or is a complication of photorefractive surgery. It is a consequence of disruption of the normal corneal extracellular matrix (ECM) composition and organization. More than 75% of the corneal stroma is composed of type I collagen, with small amounts of collagen types II, III, V, VI, and XI, and various proteoglycans (PG), which form parallel fibers organized into orthogonally stacked lamellae[96]. In ectatic corneas, complex mechanisms, including abnormal collagenase activity, result in degradation of collagen and loss of proteoglycans, characterized by fibril loosening and weakened mechanics[97].

Collagen crosslinking is an effective method to slow or halt the progression of corneal ectasia; for example, riboflavin 5'-phosphate (RF) sodium (Photrexa, Avedro, Inc, Waltham, MA, USA) crosslinking[98] was recently approved by the FDA as a clinical treatment for keratoconus. This system uses ultraviolet-A (UVA) irradiation to initiate a radical reaction with RF. Riboflavin generates free radicals with UVA irradiation and initiates the formation of carbonyl-based covalent bonds within collagen fibrils and proteoglycans. Numerous studies have demonstrated that collagen crosslinking improves vision quality and slows disease progression[99]. However, UVA irradiation

[3] Text and figures in this chapter reprinted from Investigative Ophthalmology and Visual Science, X. Wang, S. Majumdar, et al. G. Ma, J. Sohn, S.C. Yiu, et al., Chondroitin Sulfate-based Biocompatible Crosslinker Restores Corneal Mechanics and Collagen Alignment, (2017). This work is licensed under the Creative Commons Attribution-NonCommercial-NoDerivatives 4.0 International License. To view a copy of this license, visit http://creativecommons.org/licenses/by-nc-nd/4.0/ or send a letter to Creative Commons, PO Box 1866, Mountain View, CA 94042, USA.

can cause clinical complications, such as keratocyte apoptosis, temporary corneal haze, and, in more serious cases, corneal melting and permanent corneal scarring[75]. Alternative treatments now aim to avoid UV light exposure to the eye. These include rose Bengal-green light crosslinking[100] and core protein decorin crosslinking that does not require any light exposure[101].

Collagen based biomaterials also frequently require structural reinforcement through chemical crosslinking. Small molecule chemical crosslinkers, such as paraformaldehyde and glutaraldehyde are highly efficient but are also toxic. Their use necessitates additional biomaterial processing steps to ensure complete elimination of these toxic crosslinkers before application in biological systems or for internal use. Carbodiimide bioconjugation, involving 1-ethyl-3-(3-dimethylaminopropyl) carbodiimide hydrochloride (EDC) and N-hydroxysuccinimide (NHS), is also widely used in the biomaterials community[102]. The NHS group interacts with the carboxyl group of the target molecule and can then react with amine groups.

Proteoglycans play an important role in collagen fibril formation and lamellar assembly during corneal development[103]. They are composed of glycosaminoglycan (GAG) chains and core proteins. Chondroitin sulfate is one of the most abundant GAGs in the natural extracellular matrix throughout the body, with various biological functions, such as regulating inflammation[104], reducing collagenase activity[105], and controlling collagen fiber spacing in the cornea[106]. Chondroitin sulfate is frequently incorporated into biomaterials with collagen[107] or gelatin[108] to fabricate scaffolds for cartilage or corneal substitutes[108,109]. Contact lenses that had CS loaded into them enhanced healing of corneal lesions[110], purportedly through collagen fibrillogenesis. In this study, CS was functionally modified with a highly reactive amine group, which was then used in conjunction with NHS to form crosslinks with collagens and proteoglycans present in the cornea. This crosslinking process creates strong covalent networks that ultimately stabilize the corneal structure without the use of UV radiation or other radical-initiated chemical

reactions. The CS crosslinker was applied to an ex vivo corneal ectatic model developed in the lab, and the resulting biological and structural changes were evaluated.

4.2. Methods

4.2.1. ***Synthesis of Amine-Reactive Chondroitin Sulfate***

CS-NHS was synthesized as described previously[111]. Briefly, 10% CS (w/v) (25 kDa, New Zealand Pharmaceuticals Ltd, Palmerston North, New Zealand), 67% EDC (w/v), and 25% NHS (w/v) were combined in a 7:1.5:1.5 (v/v) ratio of CS:EDC:NHS in phosphate-buffered saline (PBS) and allowed to react for 10 min at 37 °C. The mixture was flash frozen to -80 °C and then subjected to several rounds of extensive washing with -20 °C ethyl alcohol (EtOH). The final CS-NHS product was dried under argon gas flow for 2 h and subsequently placed in a vacuum desiccator overnight.

4.2.2. ***Corneal Ectatic Model and Crosslinking***

One hundred and forty-four fresh albino rabbit eyes (Cat. #41211-2) in Dulbecco's Modified Eagle Medium (DMEM) were purchased from PelFreez Biologicals (Rogers, AR, USA). Corneas with no treatment (normal) were maintained in DMEM for further crosslinking and characterization. Other corneas were treated with an enzymatic digestion solution for 1 h at 37 ℃ to create a model for KC. The digestion solution contained 10 U/ml collagenase type II (LS004177, 280 U/mg, Worthington Biochemical Corp, Lakewood, NJ, USA) and 0.1 U/ml chondroitinase ABC (C36675U Sigma Aldrich, St Louis, MO, USA) in PBS. The digestion was halted by rinsing the corneas in DMEM with 10% fetal bovine serum (Gibco, Thermo Fisher Scientific, Waltham, MA) multiple times.

Normal corneas were crosslinked by submersing the anterior segment (placing the whole eye globe upside down) in 2, 5, or 10 mg/ml CS-NHS (CS2, CS5, and CS10) solutions at room temperature

for 30 or 60 min. The KC model corneas were crosslinked in 5 mg/ml CS-NHS solution for 60 min. For comparison with other crosslinking techniques, normal and KC model corneas were pre-saturated for 20 min in a 0.1% RF, 15% dextran-500 (Sigma Aldrich) and crosslinked using a 365 nm UVA light source (F15T8/BL lamp) at 3 mW/cm2 for 30 min. One drop of RF was supplemented every 10 min.

4.2.3. ***CS-NHS Penetration into Corneal Tissue***

To track the depth of penetration of CS-NHS into the corneal stroma, the CS-NHS molecule was labeled with tetramethylrhodamine-PEO3-amine (TAMRA-PEO3-amine) (Biotium, Inc, Freemont, CA, USA) dye by mixing 10% CS-NHS and TAMRA-PEO3-amine in PBS in a 1:1 molar ratio for 5 min. CS-NHS-TAMRA was washed with -20 °C EtOH and dried under argon. The anterior region of each eye globe was immersed in 2 mg/ml TAMRA dye-only solution (background control) for 30 min, or varying concentrations (2, 5, or 10 mg/ml) of CS-NHS-TAMRA solution for 60 min (n=3 for each test condition). Corneas were subsequently rinsed repeatedly in PBS to minimize non-specific binding of the dye. Penetration of CS-NHS-TAMRA was observed through fluorescent confocal microscopy (Zeiss LSM 510, Carl Zeiss AG, Jena, Germany). The mean fluorescent intensity was calculated by subtracting the background control intensity at 100 µm depth. The Z-stacking step size was set at 25 µm/section. Penetration depth was calculated by adding the number of Z sections with higher fluorescent intensity compared to the background control.

4.2.4. ***Corneal Swelling Ratios***

Normal, CS2, CS5, and CS10 corneas were stored in 15% dextran-500 PBS solution overnight prior to measurement (n=6 for each test condition). An 8-mm biopsy punch was used to extract the central corneal button. Corneal buttons were weighed and then transferred to PBS. Change in

weight due to swelling caused by water uptake was recorded every 30 min, up to 120 min. The swelling ratio was calculated using the equation:

$q=W_s/W_o$,

where W_s represents the weight after swelling and W_o represents the original weight before swelling.

4.2.5. ***Transmission Electron Microscopy (TEM)***

After enzyme treatment and crosslinking, cornea samples were stored in 15% dextran-500 overnight before fixation. Samples were fixed in 3% paraformaldehyde, 1.5% glutaraldehyde, 5 mM $MgCl_2$, 5 mM $CaCl_2$, 2.5% sucrose, and 0.1% tannic acid in 0.1 M sodium cacodylate buffer, pH 7.2, overnight at 4 °C. They were post-fixed in 1% osmium tetroxide. Samples were stained with 2% aqueous uranyl acetate, dehydrated through treatment in increasingly concentrated ethanol, and then embedded in Eponate 12 (Ted Pella, Inc, Redding, CA) resin. Thin sections were cut and grids were stained with 2% uranyl acetate in 50% methanol and visualized with a Philips/FEI BioTwin CM120 TEM at 80 kV. Image analysis was carried out using MATLAB (MathWorks, Inc, Natick, MA) as described previously[88]. Original images were binarized using an adaptive thresholding method. Fibril diameter and density were estimated within a randomly localized window (300 x 300 dpi). The number of fibers per unit area was measured and recorded. We repeated this random procedure 200 times and estimated the density of fibers using the median number.

4.2.6. ***Live-Dead Staining***

Fresh corneas (3 corneas in each group) were dissected and submersed in PBS, 2, 5, and 10 mg/ml CS-NHS, respectively, for 60 min. Positive control corneas were treated with standard RF-UV crosslinking as described previously in “Corneal Ectatic Model and Crosslinking”. After treatment,

the corneas were stained with LIVE/DEAD® Viability/Cytotoxicity Kit (Thermo Fisher Scientific L3224) according to standard protocol. The samples were extensively washed in PBS for 5-8 times to minimize background fluorescence in the stroma. Corneas were laid flat with epithelium layer facing down, mounted with PBS, and imaged using Zeiss Inverted Fluorescence microscope.

4.2.7. ***Hematoxylin and Eosin (H&E) Staining***

Normal, KC model, UV-crosslinked KC model (KC-UV), and 5 mg/ml CS-NHS-crosslinked KC model corneas (KC-CS5) were stored in 15% dextran-500 overnight to minimize swelling, and then fixed overnight with 10% formaldehyde, followed by graded dehydration with 70% to 100% ethanol, and embedded in paraffin. Sections (5 μm) were cut and stained with H&E (Sigma Aldrich) according to standard protocol.

4.2.8. ***Tensile Testing***

Uniaxial tensile testing was carried out on a Bose EnduraTEC ELF3200 (Bose ElectroForce, Framingham, MA, USA) to determine the stress-strain behavior of the corneas before and after crosslinking. All test samples for tensile testing were stored in 15% dextran-500 solution overnight to minimize swelling. Corneas (n=6 in each test group) were cut into strips of around 5 mm each, and the exact width and thickness of each strip was recorded. The corneal strip ends were affixed to the clamps on the tensile tester using super glue to avoid slippage. Load and displacement measurements were recorded by WinTest software (TA Instruments, New Castle, DE, USA).

4.2.9. ***Quantitative Real-Time Reverse Transcriptase Polymerase Chain Reaction***

Immediately following enzyme digestion for KC model corneas and treatment via crosslinking, corneas (n=6 for each test condition) were flash-frozen in liquid nitrogen and ground using pre-cooled ceramic mortars and pestles. The powdered corneal tissue samples were treated with TRIzol (Thermo Fisher Scientific) and total RNA was collected using the RNeasy Mini Kit (Qiagen, Venlo,

The Netherlands). The mRNA was quantified using a Nanodrop-1000 spectrophotometer (Thermo Fisher Scientific), and then reverse-transcribed using a High Capacity cDNA Kit (Thermo Fisher Scientific). Quantitative Real-Time Reverse Transcriptase Polymerase Chain Reaction (Q-RT-PCR) was performed with the SYBR Green qPCR Master Mix (Applied Biosystems), and expression levels were normalized using the housekeeping gene *Gapdh*. The primers of the targeted genes are listed below.

Gapdh forward: 5'-CTCTGGAGTGGATGTT-3',

Reverse: 5'-CCATGGGTGGAATCATACTG-3';

Tnfα forward: 5'-GTAGTAGCAAACCCGCAAGT-3'

Reverse: 5'-GGTTGTCCGTGAGCTTCAT-3'

Mmp9 forward: 5'-AGTACCGAGGAAAGCCTACTT-3'

Reverse: 5'-TGCAGGATGTCAAAGTCTAC-3'

Aldh forward: 5'-GACGATAACTGCAGAGCACG-3'

Reverse: 5'-ACTCATTCGACAAGCAGACAG-3'

Biglycan forward: 5'-GCATCCCCAAAGATCTGCC-3'

Reverse: 5'-CAACTTGGAGTATCGGAGCAG-3'

4.2.10. ***Statistical Analysis***

Student's t-test was used to statistically examine differences between normal corneas and cross-linked corneas in terms of collagen fibril diameter and fibril density. Swelling ratio, Young's modulus, and gene expression were analyzed with Prism 6.01 software (GraphPad Software, Inc,

San Diego, CA, USA) using one-way analysis of variation (ANOVA). All experiments were repeated twice, with n=6 corneas in each experimental group. P-values <0.05 were considered statistically significant.

4.3. Results

4.3.1. CS-NHS Penetration into the Cornea

As CS is a large molecule (~25 kDa molecular weight), it was important to validate its penetration capability into the corneal stroma before assessing its crosslinking efficacy. The -NHS group in CS-NHS and the amine group in the fluorescent dye TARMA react to form the TAMRA-labeled CS-NHS entity (**Figure 4.1**A), which allows visualization of the penetration depth and intensity of CS-NHS in the corneal stroma. Corneas treated with CS-NHS-TARMA had a clear fluorescent band. The fluorescent intensity was stronger with longer treatment durations and higher CS-NHS concentrations (**Figure 4.1**B). The mean fluorescent intensity at 100 μm in stroma increased significantly with crosslinking time and concentration (**Figure 4.1**C). At 60 min of crosslinking, the penetration depth reached up to 275 μm (2 mg/mL crosslinker), 375 μm (5mg/mL crosslinker), and 400 μm (10 mg/mL crosslinker) respectively (**Figure 4.1**D), with an average total corneal thickness of over 700 μm resulting from swelling.

4.3.2. Impact of CS-NHS Crosslinking on Corneal Swelling and Biomechanics

CS-NHS reacts with amine groups in collagen and proteoglycans in the cornea, forming crosslinked covalent networks (**Figure 4.2**A). Therefore, the effectiveness of the crosslinking treatment can be estimated by differences in corneal swelling ratios. The decrease in corneal swelling ratios after CS-NHS treatment indicated that CS-NHS was able to effectively crosslink corneal ECMs (**Figure 4.2**B). A 30-min treatment with 2 mg/ml and 5 mg/ml CS-NHS slightly reduced the swelling ratio, while a 15% decrease in swelling ratio was observed with 10 mg/ml CS-NHS treatment. A 60 min

crosslinking treatment with CS-NHS significantly decreased the swelling ratio in all treatment groups. A decrease in swelling ratio of up to 35% in CS5 and CS10 groups was observed (**Figure 4.2**C). To further characterize the enhancement of corneal mechanics through corneal crosslinking, Young's modulus of treated and untreated corneas was evaluated by tensile testing (**Figure 4.2**D). After 60 min of crosslinking treatment, CS5 and CS10 groups demonstrated significantly higher Young's moduli that was up to 20% greater than groups that did not receive crosslinking treatment.

4.3.3. ***Normal Corneal Ultrastructure After Crosslinking***

Normal corneas were crosslinked to determine the optimal treatment time and crosslinker concentrations. Following CS-NHS crosslinking, treated corneas exhibited larger fibril diameters and densities compared to normal corneas (**Figure 4.3**, Table 4.1). The formation of a tighter covalent network after CS-NHS crosslinking increased fibril density when compared to normal corneas. CS5 and CS10 crosslinking demonstrated a significant increase in fibril density, even at lower crosslinking durations (30 min). Following crosslinking for 60 min, CS5 and CS10 groups also presented a larger mean fibril diameter of 55±13.40 and 59±11.56 nm, respectively, compared to 44.24±11.89 nm in the untreated normal group. Overall, higher crosslinker concentrations and crosslinking time significantly increased fibril diameter and density. The morphological and mechanical data taken together suggest that CS5 (60 min) crosslinking provided significant mechanical reinforcement, while minimally changing the collagen fibrillar dimensions compared to the native cornea. Therefore, CS5 was chosen as the optimal crosslinking condition for treatment of KC model corneas.

4.3.4. ***Cell Viability in CS-NHS Crosslinking***

Corneal cells maintained viability after 60 min of crosslinking with few apoptotic cells (**Figure 4.4**, red arrow) in all CS-NHS crosslinking concentrations used, as evidenced by qualitative live-dead staining. No visible difference among 2 mg/ml, 5 mg/ml, and 10 mg/ml CS-NHS crosslinking

concentrations was observed, and there were no significant differences in cell viability compared to non-crosslinked cornea controls. Only positive dead cell staining was presented in RF-UV corneas due to the autofluorescence of riboflavin in 488 nm channel. The positive control demonstrated considerable cell apoptosis compared to the rest of the groups.

4.3.5. ***Ectatic Corneal Morphologies and Biomechanics Following CS-NHS Crosslinking***

The efficacy of CS-NHS crosslinking versus the gold standard UV crosslinking was evaluated in an ectatic cornea model. KC model corneas exhibited damaged lamellar structures after enzyme treatment. Following CS-NHS crosslinking treatment, the corneas recovered the compact stromal structure seen in native tissue (**Figure 4.5**A, B). No major histological differences were observed between UV and CS-NHS crosslinked explant corneas (**Figure 4.5**A).

TEM imaging (**Figure 4.5**B) corroborated that collagen fibers in KC model corneas were disrupted, with decreased fiber diameter and increased interfibrillar spacing. Treatment with CS-NHS and UV increased collagen fibril density and restored lamellar spacing. Analysis of TEM images of ectatic corneas demonstrated the efficacy of UV versus CS-NHS crosslinking. The standard 30 min UV irradiation increased collagen density with no significant change in fibril diameter. On the other hand, 60 min of 5 mg/ml CS-NHS crosslinking increased corneal collagen fibril diameter and density (Table 4.1).

Stress-strain curves from uniaxial tensile testing demonstrated that, on average, KC model corneas had a 40% lower Young's modulus value when compared to normal corneas. Efficacy of UV crosslinking and CS-NHS crosslinking was comparable and both treatments increased the Young's moduli of KC model corneas by approximately 40% (**Figure 4.5**C, D).

4.3.6. ***Keratocyte Gene Expression After Crosslinking***

Maintaining keratocyte phenotype without triggering proinflammatory gene activation is important to minimize clinical complications, such as corneal haze and scarring. The proinflammatory genes, *Tnfα* and *Mmp9*, as well as the keratocyte marker genes, *Aldh* and *Biglycan,* were evaluated in *ex vivo* rabbit corneas after UV, and CS-NHS crosslinking (**Figure 4.6**). Enzyme treatment (KC) did not significantly affect inflammatory gene expression, however it downregulated keratocyte marker expression. UV crosslinking substantially upregulated inflammatory gene production *Tnfα* and *Mmp9* in both normal and KC model corneas. Conversely, CS-NHS crosslinking did not upregulate *Tnfα* expression, and, moreover, significantly down-regulated *Mmp9* expression. Both UV and CS-NHS crosslinking enhanced *Aldh* expression in KC model corneas. Crosslinking and enzyme treatment reduced *Biglycan* expression, but CS-NHS crosslinking preserved higher *Biglycan* expression as compared to UV crosslinking in KC model corneas (**Figure 4.6**). Therefore, CS-NHS crosslinking induced less inflammation and better preserved keratocyte phenotype when compared to UV crosslinking.

4.4. Discussion

UV light-initiated corneal crosslinking, the leading clinical strategy to delay or even halt keratoconus progression[112], utilizes photo-generated free radicals to strengthen intrafibrillar binding within collagen fibrils[112]. However, the cytotoxicity owing to extended periods of UV irradiation causes keratocyte depletion and can also potentially harm corneal endothelial cells[113,114]. Glycosaminoglycans, such as CS, have been proved to provide biological benefits in corneal tissue engineering, such as promoting corneal wound healing[110]. Therefore, CS was designed to be the backbone of the biocompatible crosslinker by modifying it with -NHS, an amine-

reactive moiety, which allowed us to apply CS-NHS for collagen fibril crosslinking in animal corneas.

Corneal ectasia causes stromal thinning, resulting in weakening and distortion of the underlying stromal collagen ultrastructure[69]. Therefore, a major indicator for successful crosslinking is the restoration of the collagen fibril arrangement and spacing in diseased corneas[115]. The mechanism of UV crosslinking has been reported to be mostly intra-fibrillar, as evidenced by previously reported small and wide angle X-ray scattering results, demonstrating no changes to interfibrillar spacing after crosslinking., Thus, crosslinking occurred predominately at the collagen fibril surface and in the protein network surrounding the collagen[116]. UV crosslinking slightly increased fibril diameter, but did not reduce swelling ratio[116]. In our present study, after 60 minutes of CS-NHS crosslinking, the swelling ratio was reduced and more importantly, when carried out with high crosslinker concentrations, collagen fibril diameter and fibril density were significantly increased. This indicates that with multiple -NHS functional groups on a single CS chain, crosslinks between CS-NHS and collagen fibrils occur at both intrafibrillar and interfibrillar levels.

Our previously established KC model[88] demonstrated that controlled enzymatic treatment of the corneal ECM triggers collagen fibril degradation, resulting in an increase in interfibrillar spacing and corneal thinning. The KC model corneas also showed lamellar undulations representing disruption in corneal collagen organization, mimicking physical and ultrastructural changes in severely ectatic corneas. Tissue stiffness of normal corneas increased significantly after crosslinking with CS-NHS, particularly at high crosslinker concentrations. CS-NHS crosslinking also largely ameliorated the loss of mechanical integrity of enzymatically weakened KC model corneas, as observed via mechanical testing. Therefore, covalent crosslinking at the fibrillar level, which decreases interfibrillar spacing and increases fibril diameter, led to an increase in bulk stiffness. Histological analysis confirmed that increase in fibril thickness and tighter packing of collagen fibrils resulted in corneal densification, as evidenced by change in the gross thickness.

Since the reinforcement of corneal biomechanics is the overarching goal of corneal crosslinking, it was important to compare CS-NHS crosslinking with traditional UV-based crosslinking, which demonstrated some of the same outcomes[115]. UV and CS-NHS crosslinking treatments on KC model corneas resulted in a statistically significant increase in tissue stiffness compared to untreated KC model corneas. Moreover, the difference between efficacy of treatment between UV and CS-NHS crosslinking was not significant.

Nevertheless, any improvement to mechanical stability or vision is of no clinical value if the safety of the treatment is not ensured. Although keratoconus is generally considered a noninflammatory disease, previous studies have shown that the levels of degradative enzymes, such as Mmp9, were elevated in keratoconic corneas[117]. Moreover, UV crosslinking also triggers pro-inflammatory cytokine production, including Tnfα, which affects cell signaling in corneal stroma and eventually induces keratocyte apoptosis and, in severe cases, permanent corneal scarring[118,119]. We therefore examined the expression of proinflammatory markers Tnfα and Mmp9, as well as key keratocyte markers Aldh and Biglycan in normal and KC model corneas subjected to the different crosslinking techniques. UV crosslinking treatment in both normal and KC model corneas elicited drastic Tnfα and Mmp9 upregulation, direct evidence of the inflammatory response caused by UV irradiation. In comparison, CS-NHS crosslinking did not show upregulation of these inflammatory markers and, in fact, elicited a downregulation of Mmp9. Furthermore, CS-NHS crosslinking was able to protect the keratocyte phenotype by maintaining Aldh expression. Biglycan was downregulated in all crosslinked and KC model groups, but CS-NHS crosslinked corneas had higher Biglycan expression in comparison to UV crosslinked corneas. The gene expression results demonstrate the biocompatible and potentially protective nature of CS-NHS as a corneal crosslinker.

In summary, CS-NHS provides a safe and effective potential alternative option to treat or prevent corneal ectasia. Several caveats to the KC model exist that may preclude its ability to mimic in vivo

function and efficacy of CS-NHS crosslinking. Keratoconus is an idiopathic disease and can have several potential pathophysiologies. The enzyme-mediated *ex vivo* model which we utilized to characterize crosslinking efficacy presented a loss of mechanical strength, loss of total protein and ultrastructural damage, which represented several characteristics of keratoconus. However, this ex vivo model still provides an affordable and versatile approach to evaluate new crosslinking methods before initiating preclinical animal studies. Additionally, enucleated ex vivo eyes undergo swelling, which may impair the epithelial barrier function, allowing deeper CS-NHS penetration. Furthermore, CS-NHS also potentially binds to the epithelial layer ECM. Therefore, although the study was carried out without epithelial cell removal, the transepithelial penetration of CS-NHS needs further examination in vivo. Finally, due to the high reactivity of the –NHS functional group, CS-NHS has to be prepared fresh before use and could be challenging to maintain on the eye for an extended duration. Future in vivo studies will be designed after careful evaluation of the transepithelial diffusion rate and crosslinking efficiency of CS-NHS.

4.5. Conclusions

The ability to slow corneal ectasia and keratoconus progression should not come at the cost of damage or injury to healthy cells in the cornea. To circumvent potential harm from exposure to UV in traditional UV crosslinking techniques, we developed a safe and biocompatible crosslinking approach that maintains the efficacy standards of the traditional treatment. CS-NHS induced both intrafibrillar and interfibrillar crosslinking, promoted lamellar stabilization, restored mechanical properties in disease model corneas and reduced proinflammatory gene (*Tnfα* and *Mmp9*) expression, while maintaining higher levels of keratocyte marker gene expression compared to UV crosslinking. In conclusion, the CS-NHS crosslinking technique was demonstrated to be an effective tool to repair tissue degeneration in an *ex vivo* rabbit model, presenting several potential

advantages over current and traditional therapies. Future studies of the CS-NHS crosslinking method will be carried out to test the efficacy of the crosslinking technique and safety *in vivo*.

Table 4.1 Ultrastructural analysis of corneas before and after crosslinking

	Fibril diameter (nm)	Density of fibril (per 300x300 dpi)
Normal	44.24±11.89	16.6±0.55
CS2 30min CS2 60min	45.76±10.57 52.37±9.42	17.2±0.53 18.4±1.10*
CS5 30min CS5 60min	49.32±12.43 55.77±13.40*	20.3±0.74* 20.9±0.98*
CS10 30min CS10 60min	52.78±13.23* 59.51±11.56*	28.0±1.02* 22.8±0.89*
KC	45.38±14.66	14.1±0.68*
KC-UV 30 min	46.42±11.39	19.1±0.97#
KC-CS5 60 min	50.35±13.74	19.6±1.07#

Normal group refers to rabbit corneas without any treatment. Data presented as means ± standard deviation. Student's t-test was used to statistically examine differences.

*$p<0.01$ compared with the Normal corneas

#$p<0.01$ compared with the KC corneas

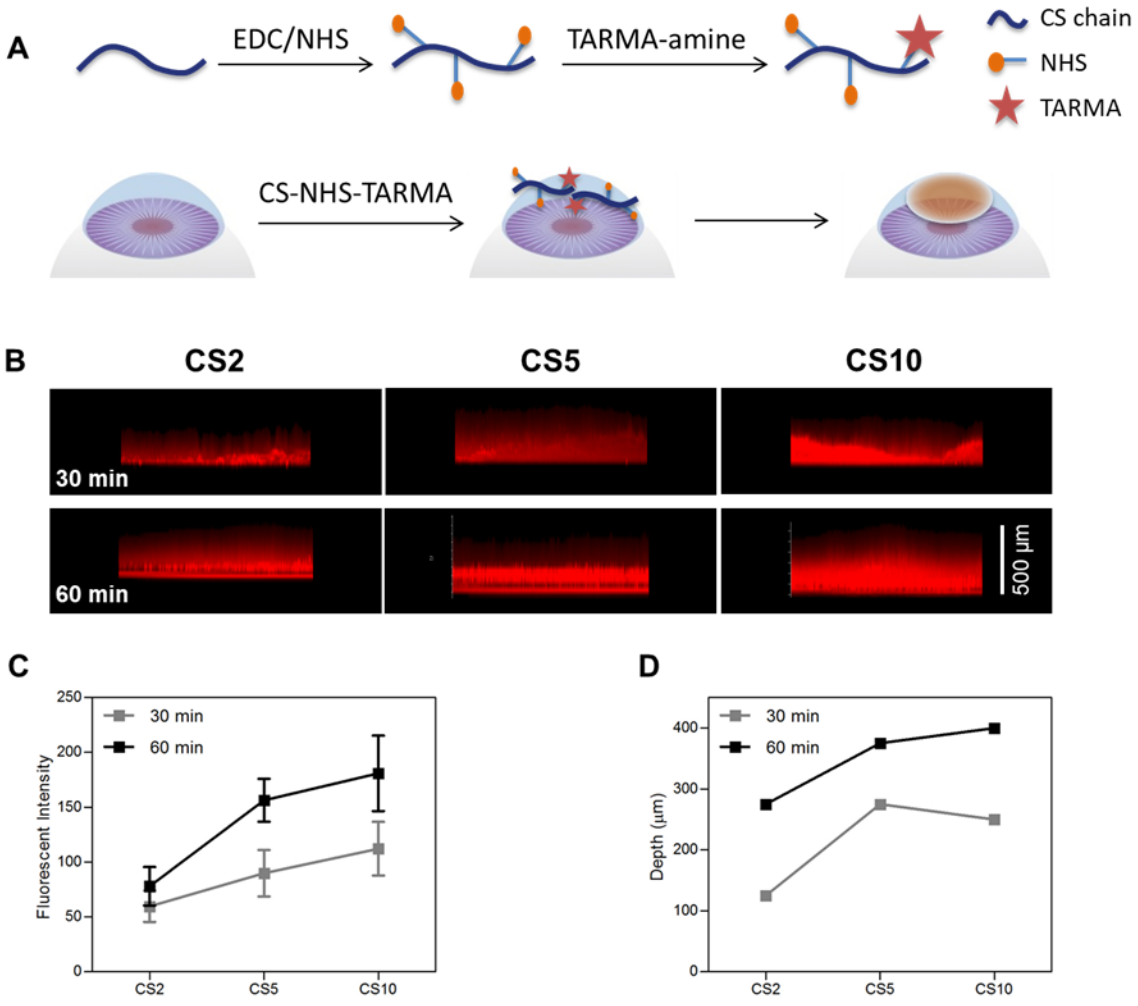

Figure 4.1 Chemical design and penetration of CS crosslinker through the cornea. (A) CS-NHS is labeled with TARMA dye by covalently reacting with amine groups in TARMA-$(PEO)_3$-amine to track penetration depth. (B) Corneal explants were immersed in varying concentrations of fluorescently labelled crosslinker for 30 and 60 min to visualize CS-NHS penetration. Image analysis quantified the (C) intensity at 100 µm depth (related to concentration) and (D) depth of fluorescently labeled CS-NHS crosslinker. The CS-NHS crosslinker penetrated approximately 250-400 µm into the corneal tissue after 60 min of exposure.

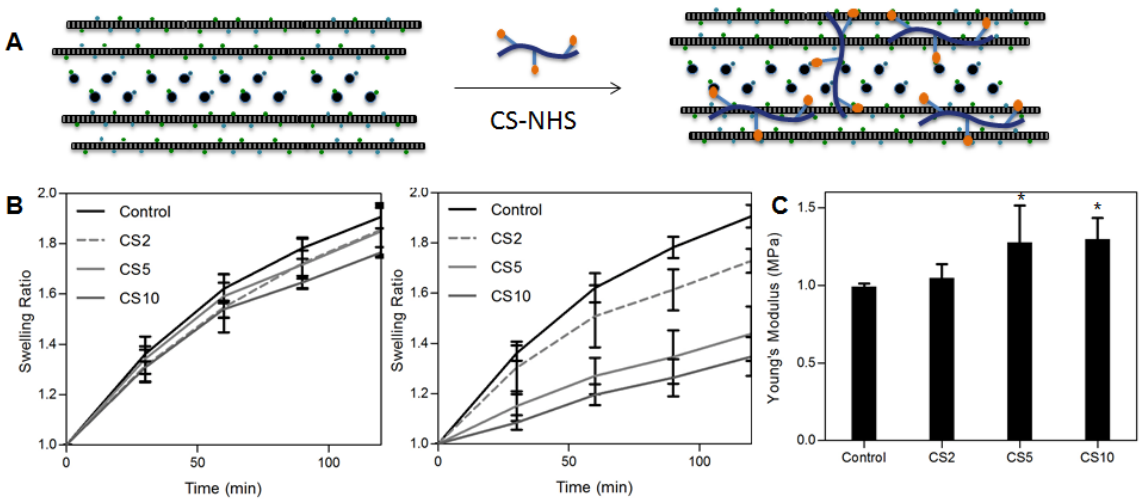

Figure 4.2 Normal corneal swelling and biomechanical properties after crosslinking. (A) CS-NHS reacts with collagen molecules and forms a strong covalent network. (B) The decrease of swelling ratio was in direct response to crosslinking time and CS-NHS concentration after 30 min and 60 min of crosslinking; (C) the enhancement of corneal biomechanics was demonstrated with Young's modulus increase after 60 min of crosslinking. N=6 in each group and *p<0.05 compared to control corneas.

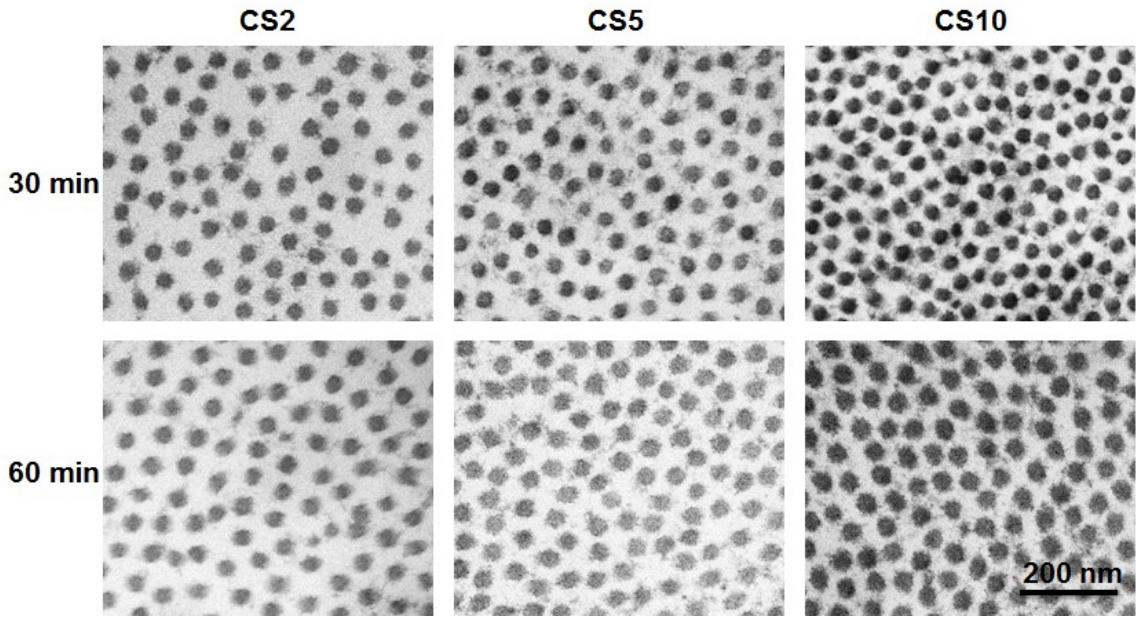

Figure 4.3 Normal corneal ultrastructures after crosslinking. Crosslinking time and crosslinker concentration have significant impacts on corneal ultrastructure. Collagen diameter and fibril density increased gradually with the increase of crosslinking time and concentration.

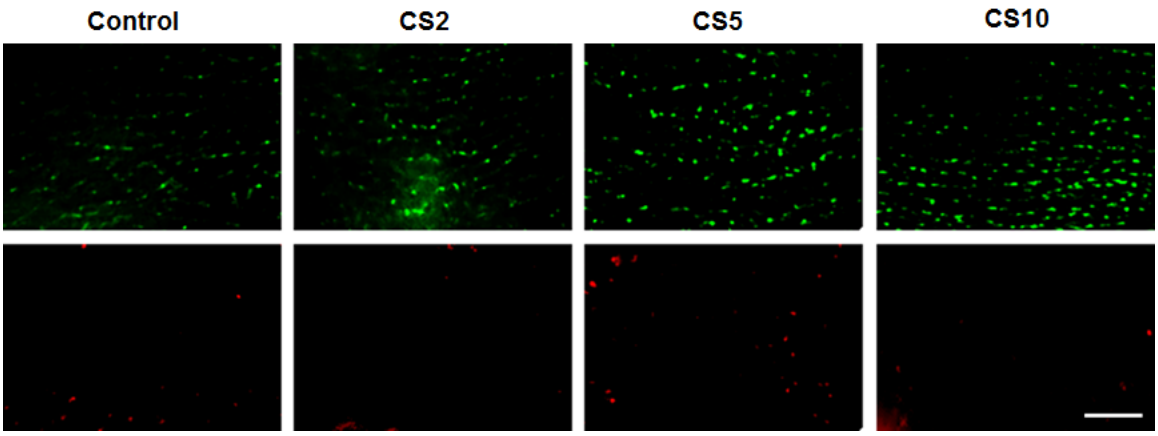

Figure 4.4 Cell viability after crosslinking. Keratocyte viability after CS-NHS crosslinking was evaluated with live-dead staining. White arrows indicate corneal epithelial cells, dashed arrows indicate keratocytes, and red arrows indicate apoptotic cells. No significant cell apoptosis occurred after 60 min of crosslinking.

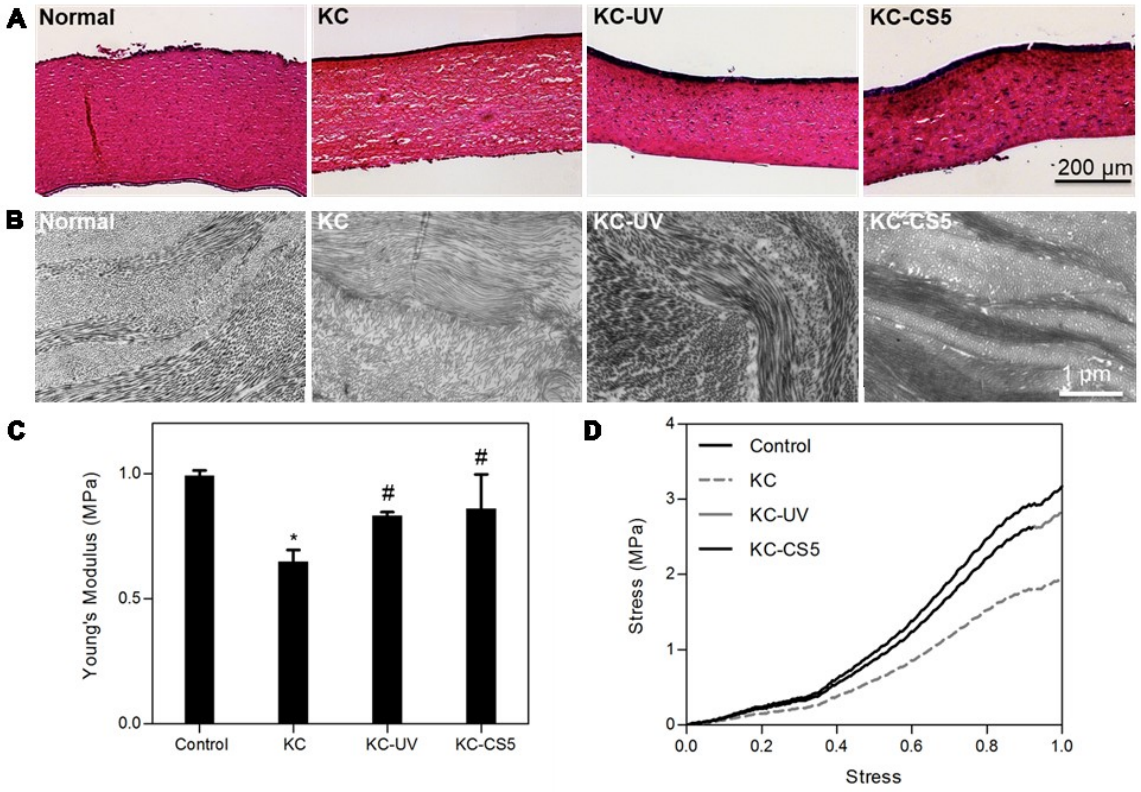

Figure 4.5 Ectatic corneal morphology and biomechanics after crosslinking. (A) Histological images of corneas undergoing different treatments, and (B) TEM images at 9700x magnification of KC corneas after crosslinking. Images from left to right represent normal, enzyme treated (KC), UV crosslinked KC (KC-UV), and 5 mg/ml CS-NHS treated KC (KC-CS5) corneas. (C) Young's modulus and (D) stress-strain curves of normal and ectatic corneas after crosslinking. N=6 in each group, * refers to $p<0.05$ compared to normal corneas, and # refers to $p<0.05$ compared to KC corneas.

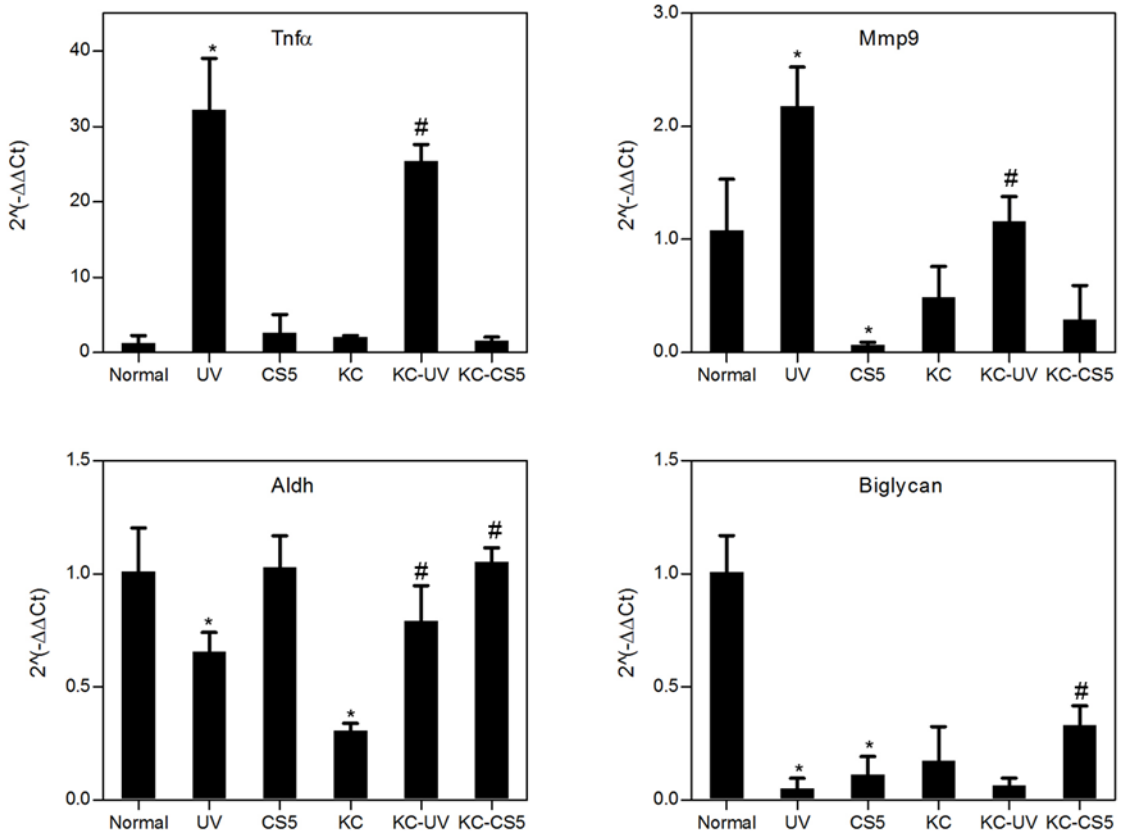

Figure 4.6 Gene expression of keratocytes after crosslinking. Inflammatory markers Tnfα and Mmp9, keratocyte markers Aldh and Biglycan were evaluated among normal, KC and crosslinked corneas. N=6 in each group, * refers to $p<0.05$ compared to normal corneas, and # refers to $p<0.05$ compared to KC corneas.

5. Artificial chaperone driven collagen self-assembly to engineer a biomimetic cornea implant

5.1. Introduction

Collagen is the most common protein found in the body[120]. While present in various chemical and physical forms, it serves a critical role as a structural building block in many tissues. Collagen's self-assembly properties allow it to spontaneously form triple helices that can assemble into larger fibrils. Further organization of collagen fibrils, such as parallel alignment, provides additional mechanisms for controlling mechanical properties that can also impact biological responses[121,122,123]. Fibril diameter alone can impact cell adhesion, migration and phenotype[36]. These structural features and self-assembly properties of collagen can be leveraged to create biomaterials with unique physical and biological properties for studying cell-matrix interactions and for engineering functional biomaterials.

In the cornea, collagen has a particularly unique structural and functional organization that is responsible for creating a transparent tissue[18]. Collagen fibrils found in the cornea have a small diameter (30-35 nm) and these fibers are aligned in parallel in sheets or lamellae, each 2 μm thick[124]. Furthermore, the parallel alignment of the collagen fibrils in each lamella run orthogonal to adjacent layers, providing anisotropic mechanical integrity. The lamellae and collagen fibrils are spaced in a highly regular arrangement, that allows light to pass through the tissue without scattering or diffraction[125,126], creating a transparent structure that serves as the window to the eye[20,43]. The complex matrix organization in the cornea is formed during embryological development. SLRP chaperones such as decorin, biglycan and lumican bind collagen and guide the self-assembly process by maintaining collagen alignment and spacing[127,128,129]. When the adult cornea is damaged, local biological cues drive repair mechanisms and rapid collagen extracellular matrix formation. Without molecular chaperones

guiding matrix assembly, the original lamellae and aligned collagen structures of the cornea cannot reform. Instead, scar tissue develops after injury, which is not transparent and impairs vision.

There is a significant clinical need to create corneal substitutes as an alternative to human cadaveric transplantation. While in many respects a successful surgery, allograft corneal transplantation requires donor tissue and suffers from slow, chronic mechanical failure and immune rejection. When transplantation fails, as in up to 70% of cases in high-risk patients with vascularization or previous transplant rejection history[5,6,7,8], few alternatives exist today. Early attempts to create an off-the-shelf cornea substitute utilized synthetic polymers such as poly (methyl methacrylate) and poly [2-hydroxyethyl methacrylate]. Cornea implants derived from these synthetic materials, however, do not integrate with the surrounding tissue, stimulate inflammation with neovascularization, and are often ultimately extruded from the eye through a process called corneal melting[22]. More recently, biological corneal substitutes have been synthesized from collagen[24,26,29,130,131]. These collagen implants are more biocompatible than synthetics but generally lack structural organization and thus functional properties of native tissue. Without the native corneal structure, it is challenging to simultaneously achieve both the mechanical properties adequate for suturing and the transparency for vision. Methods to concentrate collagen can produce orthogonal lamellae similar to the native tissue[27,28,132,133] but the materials do not reach the thickness of the human cornea relevant for clinical transplantation.

Here, we create a collagen-based biomaterial implant that mimics the native cornea structure and demonstrates functionality as a corneal patch. Artificial chaperones, in the form of cyclodextrins (CD), were combined with collagen gels[134] in a vitrification process[32,34,35,135,136], to promote and guide fibril formation and assembly into parallel aligned, orthogonal lamellae similar to tissue development. Biocompatibility and surgical performance of the biomimetic CD/collagen implants were validated in a rabbit partial keratectomy cornea model.

5.2. Methods

5.2.1. ***Synthesis of CD/Col corneal implants via vitrification***

Equal volumes of 5 mg/ml pH 3 acid solubilized Type I collagen solution and CD solution, containing 20 mM HEPES buffer at pH 11 were mixed at 4ºC and poured into hydrophilic culture dishes. The solution was then incubated at 37ºC and 5% CO_2 for 2 hours to complete gelation. The resulting gel was then placed in a sterile humidifying chamber (vitrifier) at 5ºC and 40% relative humidity (RH) for 1 day. Gels were further dehydrated in a second vitrifier at 40ºC and 40% RH for 1 week to form transparent, rigid vitrigel materials. The resultant vitrigel materials were rehydrated in DPBS overnight to form transparent, flexible, robust hydrogels prior to characterization, cell culture or in vivo application.

5.2.2. ***Electron microscopy (EM)***

Samples were fixed in 3% paraformaldehyde, 1.5% glutaraldehyde, 5 mM_2, 5 mM $CaCl_2$, 2.5% sucrose, and 0.1% tannic acid in 0.1 M sodium cacodylate buffer, pH 7.2. After buffer rinse, samples were post fixed in 1% osmium tetroxide for 1 h on ice in the dark. Following a rinse with distilled water, the samples were stained with 2% aqueous uranyl acetate (0.22 μm filtered) for 1 h in the dark, dehydrated using a graded series of ethanol, and embedded in Eponate 12 resin (Ted Pella, Redding, CA). Samples polymerized for 2–3 days at 37°C and were stored at 60°C overnight. Thin sections, 60-90 nm, were cut at a depth of 50 μm from the surface with a diamond knife using a Reichert-Jung Ultracut E ultramicrotome and placed on naked copper grids and were stained with 2% uranyl acetate in 50% methanol, and observed using a Philips CM120 TEM at 80 kV. SEM samples were fixed as described above and affixed to SEM stubs. A Leo FESEM was used to observe the samples. Lamellar thickness was determined using Image-J software for Windows (US National Institutes of Health, Bethesda, MD) on the TEM and SEM photomicrographs.

5.2.3. ***Atomic Force Microscopy (AFM)***

Dried and rehydrated Vitrigel samples were imaged by AFM. All data presented here have been acquired on a commercial Cypher S system (Asylum Research, Santa Barbara, CA, USA) under ambient conditions. Commercially available silicon nitride cantilevers with a nominal resonance frequency of 70kHz (AC240TS-R3, Olympus, Tokyo, Japan) were used. Each probe was individually calibrated for spring constant and sensitivity using the Sader method[137]. Typical k values ranged between 0.9nN/nm and 1.10nN/nm.

Imaging was conducted in intermittent contact mode (AC or "tapping"), in Amplitude Modulation (AM) mode. The phase was left to vary freely. The cantilevers were oscillated at 7.0-8.5nm, with a work to free amplitude ratio, A/Ao, kept between 0.8 and 0.9, in order to minimize damage to the gels' surface. Under these operating conditions, the net dominant forces experienced by the oscillating cantilever are attractive. Local force variations can be visualized as a phase shift, where a larger attractive force leads to a larger phase shift[138]. Image analysis was performed using IgorPro (WaveMetrics, Lake Oswego, OR, USA).

5.2.4. ***Physical characteristics measurements***

Transparency was measured by placing fully rehydrated materials on 24-well plates, using the area scanning modality on a Biotek Synergy 2 microplate reader in the visible light wavelength range of 300-700 nm with 50 nm intervals.

Tensile testing was performed on hydrated materials using dog-bone shaped tensile test strips, each 5mm in width. Digital Vernier calipers were used to measure the individual thickness of the CD/Col materials between two glass slides. Thickness was measured at six different points for each sample. CD/Col materials were then loaded onto a Bose EnduraTec (Minnetonka, MN) mechanical tester and stretched at a speed of 0.02 mm/s using a 225 N load cell for native cornea, and 250g load cell

for CD/Col materials. To maintain hydration, the hydrated samples were saturated with PBS prior to load application. Load vs displacement values were obtained and fracture strain was recorded. Stress-strain curves were calculated using Microsoft Excel.

Rheology was performed with an Ares G2 rheometer (TA Instruments New Castle, DE). Experiments were conducted at physiological temperatures (37°C). Eight mm diameter samples of 500 μm thickness were loaded on the rheometer stage (8 mm geometry, serrated) and axial force was set to 1 N. The experimental design followed a frequency sweep from 0.1 Hz to 100 Hz (2% strain), strain sweep from 1% to 100% (2 Hz frequency), oscillation time (5 min, 2 Hz, 2% shear). Three samples per group, per experiment were tested under the same rheological protocol. Sample hydration was maintained using a solvent trap.

Differential scanning calorimetry (DSC) was performed using a DSC 8000 (Perkin Elmer, Waltham, MA) to determine the denaturation temperature of the cornea and CD/Col materials. Pre-weighed hydrated samples were prepared and placed in aluminum sample pans and crimp-sealed with aluminum lids supplied by the manufacturer. Temperature ramp of 5ºC/min over a range of 10ºC to 90ºC was run. DSC thermograms were analyzed using PyrisSeries Thermal Analysis software (Perkin Elmer) version 10.1.

5.2.5. ***Biophysical studies on mechanism of CD/collagen binding and ultrastructure formation***

UV/Vis absorption was measured by mixing CDs at 0.5 mg/ml in 1 mg/ml acidic collagen solution at pH 3. Following mixing, solution was degassed and 1 mL of each solution was pipetted into wells of 24 well plates and Biotek Synergy 2 microplate reader was used to measure absorbance of wavelengths in the 250-300 nm range.

Circular dichroism spectra of collagen solution at 0.125 mg/ml at pH 3, over the range 190-250 nm were obtained using Aviv Biomedical spectrometer. Collagen was brought to pH 7 using 20 mM HEPES buffer, with or without the presence of CDs at 0.0625 mg/ml. Circular dichroism was recorded at 222 nm (absorption bands of the collagen triple helix) for different solutions over a temperature gradient of 30ºC to 60ºC.

A quartz-crystal microbalance (QCM, Qsense E4, Biolin Scientific Inc, Glen Burnie MD) was used to detect binding of CDs onto a physisorbed collagen surface. Collagen at 1 mg/ml in 1 mM HCl was adsorbed over pristine gold surface until saturation. Following this, a stable baseline was acquired with 1 mM HCl flow, without collagen. Then, CDs dissolved in 1 mM HCl at a concentration of 0.44 mM and passed through a 0.22 μm filter, were pumped at flow rate of 0.05 mL/min through the measurement chambers. Following signal stabilization, pure 1 mM HCl was flowed through the chambers again. The instrument was used to record changes in resonance frequency (fundamental resonance frequency was 5 MHz, overtones recorded were n = 3, 5, 7, 9, 11).

To quantify the βCD binding affinity to collagen molecules, isothermal titration calorimetry (ITC) was used. Collagen (5 mg/ml) were dialyzed in 3 liters of 1 mM HCl (pH=3) buffer for 24 hours, and diluted to 1 mg/ml with the dialysis buffer. Concentrated βCD at 15mg/ml (13.2 mM) was prepared using the same dialysis buffer to avoid generation of any heat of mixing. All binding parameters were measured at 20ºC using 1.4 ml of 1 mg/ml collagen sample in the cell titrated with 25 injections 10 μl 13.2 mM βCD solution each. The injections were separated by 300 seconds. The duration of each injection was 12 seconds and the filter period 1 seconds. The stirring speed and Feedback Mode/gain option were set up to 300 rpm and high respectively. The sample and reference cells were cleaned extensively before each run. Protein solutions were degassed for at least 20 min. The isothermal curve was obtained by integration of individual peaks and after subtracting the average heat of dilution. Binding parameters were determined from titration binding

curves using the one site model from the software MicroCal Data Analysis (Malvern, Westborough, MA).

5.2.6. ***Cell culture, PCR and biological assays***

Corneal epithelial cells were isolated from fresh rabbit eyes (PelFreez Biologicals, Rogers, AR). Excised corneas were incubated overnight at 4°C in 1 mg/ml of Dispase II (Roche) in supplemented EpiLife medium (Thermo Fisher). The loosened epithelial sheets were gently scraped off and transferred to Accumax (Innovative Cell Technologies, San Diego, CA) at 37°C for 30 minutes to disrupt junction proteins, and mechanically agitated followed by filtering through 70 μm cell strainer to create a cell suspension. Primary epithelial cells were seeded on CD/Col substrates at 10,000 cells/cm^2 in Human Corneal Growth Supplement (HCGS) supplemented EpiLife medium. Cell on various substrates reached confluence by day 5. Confluent cell layer was fixed in 4% paraformaldehyde for 15 min, and morphology and marker expressions were observed via immunostaining for Mouse anti-human Cytokeratin 14 (K-14) (CHEMMICON) at 1:100, followed by secondary staining of 1:100 AlexaFluor594 goat anti-mouse IgG (Life Technologies), and counter staining of DAPI (Life Technology)

Cells were harvested for qPCR at confluence. In brief, epithelial cell layers were washed with PBS for 3 times and digested with Accumax for 15 min. Cell suspension was collected and centrifuged to form cell pellet. Cell pellet was lysed with 500 μl Trizol (Thermo Fisher) and processed for RNA isolation. The mRNA was purified by RNeasy mini kit (Qiagen), quantified by nanodrop and reverse transcript by High Capacity cDNA reverse transcription kit (Thermo Fisher). Gene expression of epithelial cell markers p63, K3, CX43, were characterized by qPCR. The primer sequences (Table 5.1) were designed using Primer-BLAST (NCBI, https://www.ncbi.nlm.nih.gov/tools/primer-blast/).

Table 5.1 Primer sequences for qPCR

Gene	Primer sequence (5'-3')	Ref. sequence number	Amplicon length (bp)
GAPDH	Forward CTC TGG CAA AGT GGA TGT T Reverse CCA TGG GTG GAA TCA TAC TG	NM_001082253	90
K3	Forward GGG GGT CGC ATA GGA GTC Reverse TAT CTG GAG TAG CGC TGG G	XM_002711005	101
P63	Forward GTC TCA GTC TTC ATA CGG TAA C Reverse GCT GCT GAG GTT TGA TAA G	XM_002716509	98
CX43	Forward TAC ACC TGC AAA AGA GAC CC Reverse GAC ACC ACC AGC ATG AAG AT	NM_001198948	98

*5.2.7.**In vivo surgical procedures and post-operative care***

All experimental procedures in this study were performed in accordance to the Association for Research in Vision and Ophthalmology Statement for the Use of Animals in Ophthalmic and Visual Research, and were approved by the Institutional Animal Care and Use Committee at Johns Hopkins University. Anterior lamellar keratectomy was performed on male New Zealand albino rabbits (weight 2.5 - 3.5 kg) under general anesthesia by intramuscular administration of ketamine (35 mg/kg of body weight) and xylazine (5 mg/kg of body weight). Topical anesthesia (Proparacaine, Akorn, Lake Forest, IL) was administered on the corneal surface prior to surgical procedure. A 6 mm Hessburg-Barron vacuum trephine (Barron Precision Instruments LLC, Grand Blanc, MI) and a crescent knife (LaserEdge, Bausch&Lomb, Rochester, NY) were used to remove approximately 150 μm of anterior corneal tissue. βCD/Col corneal substitutes (approximately 125 μm thickness, 6.25 mm diameter and 7.5 mm curvature) were molded to corneal curvature and implanted using 12-14 interrupted 10-0 nylon sutures. A mixture of steroid and antibiotic ointment (Pred-G, Allergan, Irvine, CA) was applied for 21 days as a post-operative treatment. Gross

observations, including ophthalmomicroscopy and fluorescein staining were performed at day 3, 7, 14, 21 and 31 days after surgery. All animals received the same treatment, therefore no randomization was used to determine implant survival in rabbits. Consequently, researchers were not blinded. Corneas were harvested at 31 days post-surgery for pathological examinations, fixed in formalin and processed for histology. The corneal tissue was removed from the globe, dehydrated using graded ethanol solutions and treated with xylene followed by paraffin infiltration. Tissue sections were embedded in paraffin blocks and sectioned using a microtome, at 5 μm thickness. Sections on slides were then processed for standard histological Hematoxylin and eosin (H&E) staining, Masson's Trichrome staining and for immunohistochemical staining of Rat anti-Mouse CD11b (BD Biosciences)

*5.2.8.**Statistical analysis***

All experimental analyses were performed samples of at least n = 3, representative of two or more independent studies. No statistical method was used to predetermine sample size in animals. Data are expressed as mean +/− standard deviation and statistical significance (p value) between conditions was determined by One-way analysis of variance (ANOVA) with the Bonferroni post hoc test using GraphPad Prism 5.

*5.2.9.**Data availability***

The data that support the findings of this study are available upon reasonable request from the corresponding author.

5.3. Results and Discussion

*5.3.1. **CD artificial chaperones modulate collagen self-assembly***

To determine the potential use of CD as a molecular chaperone for collagen assembly, we screened CDs with varying size and functionality for their ability to control collagen self-assembly and form biomaterials with an architecture similar to the native cornea (**Figure 5.1**). CDs are circular oligosaccharides with varying internal diameter depending on the number of sugars (αCD, βCD, γCD) (**Figure 5.2a**). For example, βCD consists of seven glucopyranoside units creating an internal diameter on the order of 0.65 nm (**Figure 5.1b**). The hydrophobicity of the CD interior core[139], allows the formation of complexes with hydrophobic compounds. The CD exterior is hydrophilic and the base alcohol groups can be replaced with various functional groups such as phosphate(-PO_4), succinyl (-CO-CH_2-CH_2-CO_2H, abbreviated as -S), methyl(-CH_3), thiol(-SH), butyl(-C_4H_9), and amine (-NH_2). To generate the composite materials, CDs were dissolved in buffer and then combined with collagen to form a gel using standard conditions (CD/Col)[35]. The CD/Col gels were subsequently vitrified, a process that provides a slow, controlled dehydration under defined temperature and humidity conditions that facilitates a gradual concentration of collagen[36]. As collagen concentrations increase during vitrification, a nematic liquid crystal phase of collagen can be formed that causes molecular crowding effects and ultimately self-assembly **Figure 5.3a**).

Incorporation of CD into the collagen gelation and vitrification process produced materials with varying ultrastructure depending on the CD size and functionality (**Figure 5.3b** and **Figure 5.2b, c**). Specifically, fiber diameter, orientation and lamella development depended on the size and chemical functionality of the CD. Collagen fibers with visible banding in TEM ranged from barely detectable in gels with αCD, βCD, and γCD, to moderately visible in αCD-SH, αCD-NH_2, βCD-C_4H_9 and readily observable in TEMs of Col, αCD-Suc, αCD-PO_4, and βCD-Suc. The orientation of the fibers observed by SEM were either randomly oriented (αCD-SH, αCD-PO_4, βCD-C_4H_9,

αCD-NH_2) or aligned in parallel over large regions (αCD-Suc, βCD-Suc), similar to the native cornea. Finally, lamellae of collagen were visible grossly (**Figure 5.1d**) and in TEM of βCD and βCD-Suc containing materials, however the layers were random in thickness, ranging from 0.5 μm to 5 μm compared to the native cornea where they are consistently 2 μm. Formulations synthesized with αCD-SH and αCD–CH_3 did not form structured materials that could be handled and those with αCD-PO_4 and αCD-NH_2 were opaque. Further characterization was then performed only on formulations containing αCD, βCD, γCD, αCD-Suc and βCD-Suc, which all produced materials that were grossly transparent and could be handled.

The size and functionality of the CDs incorporated into the collagen gels impacted the bound water and thus water evaporation during the vitrification process. While all formulations started with similar liquid volumes and concentrations of collagen, the resulting CD/Col materials varied in water content (**Figure 5.4a**), and thus collagen concentration (**Figure 5.4b**) after vitrification. βCD/Col materials had the highest collagen concentration and lowest swelling ratio after vitrification, most similar to the native cornea while αCD/Col and γCD/Col had the lowest collagen concentration and highest swelling ratio (**Figure 5.4a, b**). This varying concentrating of collagen can thus influence the assembly through molecular crowding effects to produce unique ultrastructures.

Transparency is critical to the functionality of a cornea mimetic and is related to the collagen concentration and organization. Collagen materials without CD had the lowest transparency values (**Figure 5.3c**). These implants were thin (~150 μm) and were 88% transparent at 550 nm (average wavelength of white light) and only 62% when normalized to a 400 μm thickness. Therefore, achieving a minimum functional transparency at a thickness of native human cornea would be impossible with these materials. Addition of βCD produced materials with the greatest transparency, 77% at 550 nm normalized to 400 μm (**Figure 5.3c**). However, there was no

statistical significance between the transparency of different CD/Col materials (**Figure 5.3c** and **Figure 5.4c, d**).

To further evaluate the physical properties resulting from the addition of CD to collagen vitrification, we characterized the mechanical properties using a variety of methods. Shear and tensile mechanical forces impact the cornea from blinking and the intraocular pressure pushing the cornea outwards. Moreover, surgical implantation of a cornea substitute requires tensile strength to hold sutures similar to the native tissue. Finally, elasticity is needed to avoid cracking from brittleness during suturing and after implantation. Therefore, we tested and compared tensile, rheological (viscoelasticity), and compression properties of the implants with CD compared to collagen alone and the native cornea. The Young's modulus (stress/strain) was greatest for the collagen gel, however the strain at fracture was the lowest of all of the groups (**Figure 5.3d** and **Figure 5.4e, f**). This fracture at lower strain suggests lower suture hold strength. Implants containing βCD had a similar Young's modulus compared to the native cornea. The native cornea had a greater fracture strain compared to the βCD, but the difference was not significant. Cornea and βCD/Col both demonstrated significantly lower Young's modulus and strain at break than Col materials. Viscoelastic properties of the materials, measured by rheology, were significantly different between the groups and did not follow the same trends as the tensile properties. The collagen and βCD materials had the greatest storage modulus, or in other words they exhibited the ability to store a higher quantity of deformation energy elastically (**Figure 5.3e, Figure 5.4g**). The tan δ (ratio of loss modulus and storage modulus) of βCD and the cornea were similar with no statistical difference, and these lower values representing higher elastic component in the viscoelastic behavior. Thus, the βCD/Col materials exhibited tensile properties that would support suturing, and cornea-like viscoelastic properties.

To further compare the bulk properties of the CD/Col materials with the native cornea, we evaluated the denaturation temperature using differential scanning calorimetry (DSC). The specific heat

required to denature βCD/Col and the native cornea were similar and significantly greater than all of the other formulations (**Figure 5.3f** and **Figure 5.4h**). The higher value of denaturation temperature correlates with greater interfibrillar interactions between the collagen fibrils. Taken together, these morphological, mechanical, and functional data suggest that βCD/Col materials provide the best mimic of the native cornea and satisfy the design criteria of transparency and mechanical integrity required for a cornea substitute.

*5.3.2.**βCD molecular interactions with collagen***

The bulk properties of the βCD/Col materials suggested a molecular interaction between the CD and collagen molecules that impacted assembly. To explore the mechanisms of these interactions, we first considered the impact of CD on the collagen secondary structure and fibril formation using circular dichroism. The typical collagen triple helix signal in circular dichroism over the wavelength spectrum has a positive band at 222 nm and a negative band at 200 nm[140]. Addition of CD to a collagen solution increased the stability of the collagen triple helix, measured at 222 nm, demonstrated by an increased temperature required to induce protein unfolding and denaturation (**Figure 5.5a,** and **Figure 5.6a**). Further, the addition of CD changed the characteristic collagen triple helix curve of a strong negative peak at 200 nm (**Figure 5.5b** and **Figure 5.6b**). As collagen gelation occurs with neutralization, the characteristic collagen triple helix signal from circular dichroism is attenuated as the helices combine to form larger fibrils. Addition of CD reduces this signal attenuation suggesting a direct molecular interaction that suppresses fibril formation that results in the reduced fibril size that was observed in the SEM and TEM images.

To determine potential specific interactions between the CDs and collagen molecules, we evaluated the UV absorbance of solutions of collagen with αCD, βCD, γCD and βCD-Suc. βCD is known to bind with polypeptides[141] containing aromatic groups[141,142] such as tyrosine[143], as measured by a shift in wavelength and increase in peak absorbance of the characteristic UV

absorbance peak of tyrosine at 275 nm. Collagen was combined with the CDs at pH 3 so no gelation would occur and the potential interactions of CD with collagen could be isolated. The UV-Vis absorbance profile of collagen increased with the addition of CD, with βCD inducing the largest shift (**Figure 5.5c** and **Figure 5.6c**). This result suggests that the CD molecules interact with the aromatic amino acids in collagen such as tyrosine, phenylalanine and tryptophan.

CD/collagen binding was further confirmed using Quartz Crystal Microbalance (QCM). Collagen was deposited on a gold substrate after which a solution of CD was introduced (dotted line A, **Figure 5.5d**). The resonance frequency of the crystal changes when the mass of the coating changes, in this case when CD binds to collagen. Both βCD and βCD-Suc induced a frequency change in contrast to a control sucrose solution that cannot bind to collagen. When the CD solution is replaced by buffer (**Figure 5.5d**), the frequency (correlated with adsorbed mass) partially and completely returns to the initial levels for the βCD-Suc and βCD suggesting a reversible interaction. The reversibility of the CD/collagen interactions was therefore further investigated by evaluating the remaining CD in the bulk materials. When CD/Col materials were rehydrated after vitrification, an initial burst release of excess CD was observed followed by slow release of more closely bound CD quantity over 48 hours (**Figure 5.6d**).

The strength of the collagen interaction with βCD was quantified by isothermal titration calorimetry (ITC). βCD forms aggregates at concentrations higher than 2-3 mM in neutral and acidic solutions[144,145], and titration of a concentrated βCD solution at 13.2 mM into control solution (1 mM HCl, no collagen) presented a typical heat of dilution curve seen in an aggregate-monomer dissociation model. βCD (13.2 mM) was then titrated against a 1 mg/mL collagen solution in 1 mM HCl (pH3). Large exothermic peaks indicate that CDs bind to the collagen and the attenuation of the endothermic peaks from control conditions (1 mM HCl, no collagen) confirm that the βCD aggregate equilibrium shifts in favor of dissociation, and interaction with collagen (**Figure 5.5e**). The simulated binding affinity was calculated to be 511±27.4 M^{-1}, implying dissociation constant

of 1.96±0.10 mM, and the approximate number of binding sites was 10±3 per collagen molecule. This is below the estimated number of aromatic amino acids in collagen[146].

Following gelation and during vitrification, the CD molecules in the collagen gel concentrate to form aggregates as the material dehydrates. These aggregates were visible as hydrophilic regions close to collagen fibrils in the phase shift channel of atomic force microscopy (AFM) in vitrified materials with CD (**Figure 5.7**, dry state). However, once rehydrated, the CD aggregates dissolve into the rehydration buffer and these regions are no longer observed (**Figure 5.7**, rehydrated and dried state). This implies that the CD aggregations may be responsible for the enhanced structural lamellation observed in the CD/Col materials after vitrification. This lamellar configuration is preserved even after removal of the excess CD.

Taken together, the characterization of bulk properties and molecular interactions found that βCD binds with tyrosine and other hydrophobic amino acids on collagen with a dissociation constant of 1.96+0.10 mM (**Figure 5.5f**). This interaction leads to a reduced fibril diameter during gelation. In βCD-Suc, hydrophilic succinyl groups may interfere with the hydrophobic interactions between the aromatic groups on collagen and the CD inner core (**Figure 5.5g**). The succinyl groups may potentially also interact with positively charged amino acids, or form hydrogen bonds with other amino acids. The concentration of collagen during vitrification creates a liquid-crystalline phase allowing the formation of lamellae. The CD-collagen interaction is reversible and therefore the majority of the CD molecules can be removed after assembly. The resulting βCD/Col biomaterial has local fibril alignment and organized lamellae that provide increased mechanical strength and transparency, with many similarities to the native cornea.

5.3.3.βCD/Col biomimetic cornea compatibility and surgical performance

We evaluated corneal epithelial cell proliferation and biocompatibility on CD/Col implants using immunocytochemistry and gene expression (**Figure 5.8**). Primary rabbit corneal epithelial cells

proliferated and formed a monolayer on the CD/Col implant materials within 72 hours. Keratin 14 (K14, epithelial cytoskeleton protein) staining revealed that primary corneal epithelial cells maintained epithelial morphology on all materials, and expressed limbal stem cell specific protein p63 (**Figure 5.8a** and **Figure 5.9a-g**). Gene expression for p63, Connexin 43 (CX43, gap-junction protein), and Keratin 3 (K3, corneal epithelium specific cytokeratin protein) were evaluated to determine maturity of corneal epithelial cells (**Figure 5.8c** and **Figure 5.9h**). Epithelial cell gene expression on Col and βCD/Col vitrigels was similar to tissue culture polystyrene (TCPS). Epithelial cells on βCD/Col vitrigel expressed significantly higher expression of K3 compared to Col vitrigels. Concurrently, epithelial cells on βCD-Suc Col vitrigel presented significantly higher expressions of p63 and CX43, indicating maintenance of healthy epithelial cell phenotype and stem cell niche on CD/Col materials.

To translate the βCD/Col materials to applications in corneal repair, curved implants were engineered to fit the anterior corneal surface. Custom designed plastic molds were used (**Figure 5.8d**) to create lenticular implants (**Figure 5.8e**). Manufacturing protocols were developed that supported homogenous mixing of the CD and collagen along with vitrification in the curved molds. Resulting βCD/Col materials were implanted in a partial keratectomy corneal defect surgically created in a rabbit model (6 mm diameter, 150 μm depth, n=4) (**Figure 5.8f**). The βCD/Col implants were sufficiently strong to be held in place using simple interrupted sutures. Re-epithelialization across the implant and integration with the adjacent host corneal tissue was followed over 31 days (**Figure 5.8g** and **Figure 5.10**). Progress of epithelial cell migration was observed using fluorescein staining on the ocular surface under blue light. Epithelial defects are observed as fluorescent regions, while a contiguous healthy epithelium remains unstained. Sutures were removed on day 21 post-surgery, by which time the implant had successfully integrated with surrounding tissue. Over 90% re-epithelialization was achieved by the last time point for the animal study. Masson's Trichrome histological staining of the excised rabbit corneas at day 14 (**Figure 5.8h**) and day 31

(**Figure 5.10**) demonstrated the presence of the implant and epithelial cell coverage over the βCD/Col material. Further, laminin proteins, which are expressed by epithelial cells post-maturation, were detected on the re-epithelialized implant using immunohistochemistry (**Figure 5.8i** and **Figure 5.8j**). The ability to suture the βCD/Col material, its reepithelialization capacity and tissue integration, demonstrates its potential viability as a biomimetic corneal substitute.

5.3.4. ***Artificial chaperones for controlling collagen assembly and development of functional biomimetic implants***

Tissues throughout the body depend on collagen molecules assembled into complex ultrastructures relevant to their required structural and functional properties. Frequently, these tissue architectures are established during development and are unable to be recapitulated when damaged in adult tissue. Moreover, this complexity in assembly remains challenging to replicate using today's materials science techniques. Here, we demonstrated the use of cyclodextrins as an artificial chaperone to assemble collagen during gelation and vitrification. Cornea substitutes were engineered using βCD and collagen to achieve an ultrastructure similar to the native cornea with transparency and mechanical integrity required for application. Elucidation of the mechanisms in self-assembly enables the further application of the artificial chaperones for materials design that is relevant to multiple biomedical applications.

Figures and figure legends:

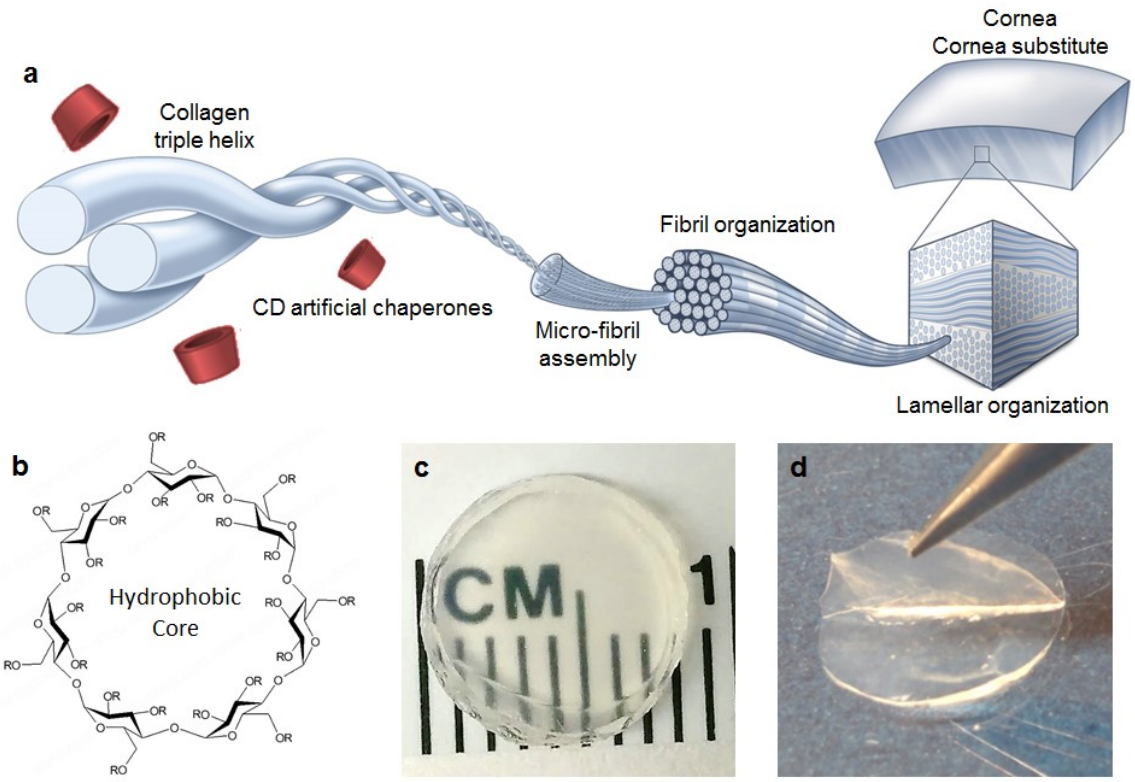

Figure 5.1 Cyclodextrin artificial chaperones modulate fibril formation and alignment in vitrified collagen cornea substitutes via interactions with collagen. a) Schematic demonstrating cyclodextrin-collagen binding, ultimately influencing collagen ultrastructural organization and spacing. b) General chemical structure of beta-cyclodextrin depicting the 7-sugar cyclic oligosaccharide with modifiable functional groups (-R). c) Gross image of 500 µm thickness implants manufactured using βCD-Suc and collagen to demonstrate optical clarity. d) Evidence of macroscale lamellar structures in the implants as evidenced by careful peeling of individual layers.

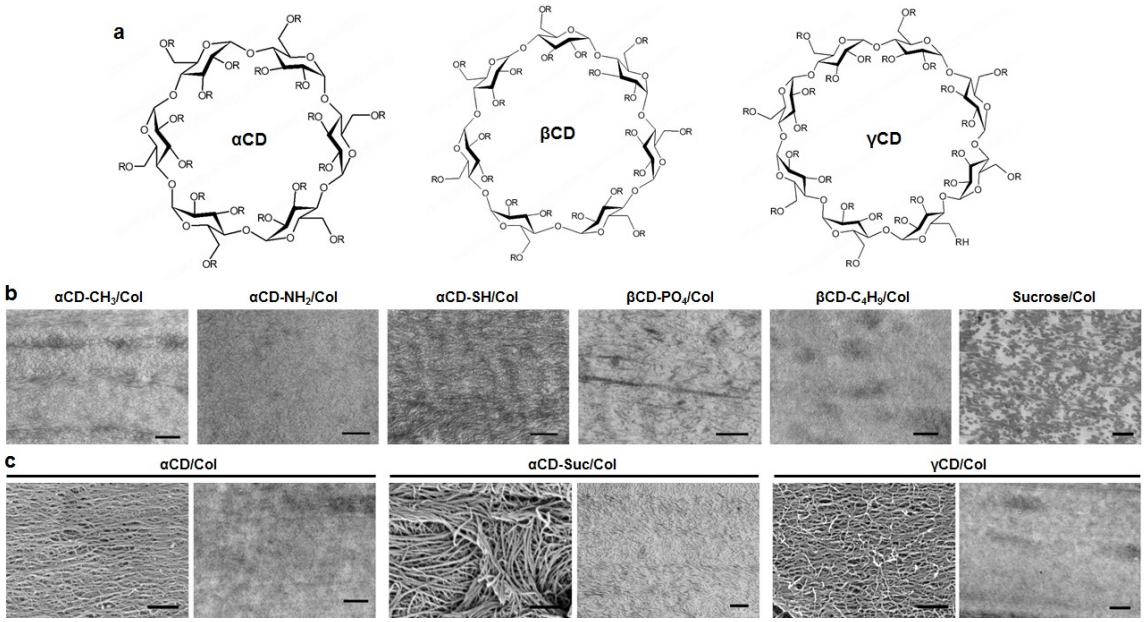

Figure 5.2 Screening CDs with varying size and functionality for ability to control collagen self-assembly. a) Molecular structures of the 6-sugar cyclic oligosaccharide α cyclodextrin, the 7-sugar cyclic oligosaccharide β cyclodextrin, and the 8-sugar cyclic oligosaccharide γ cyclodextrin. R- represents modifiable functional groups. **b)** Transmission electron microscopy of cross sections of several CD/Col materials with different cyclodextrins, during initial screening process to determine notable differences in collagen fibril formation and organization. Scale bar = 500 nm **c)** Scanning electron microscopy (left) and transmission electron microscopy (right) images to elucidate ultrastructures of αCD/Col, αCD-Suc/Col and γCD/Col respectively. Scale bar = 100 nm

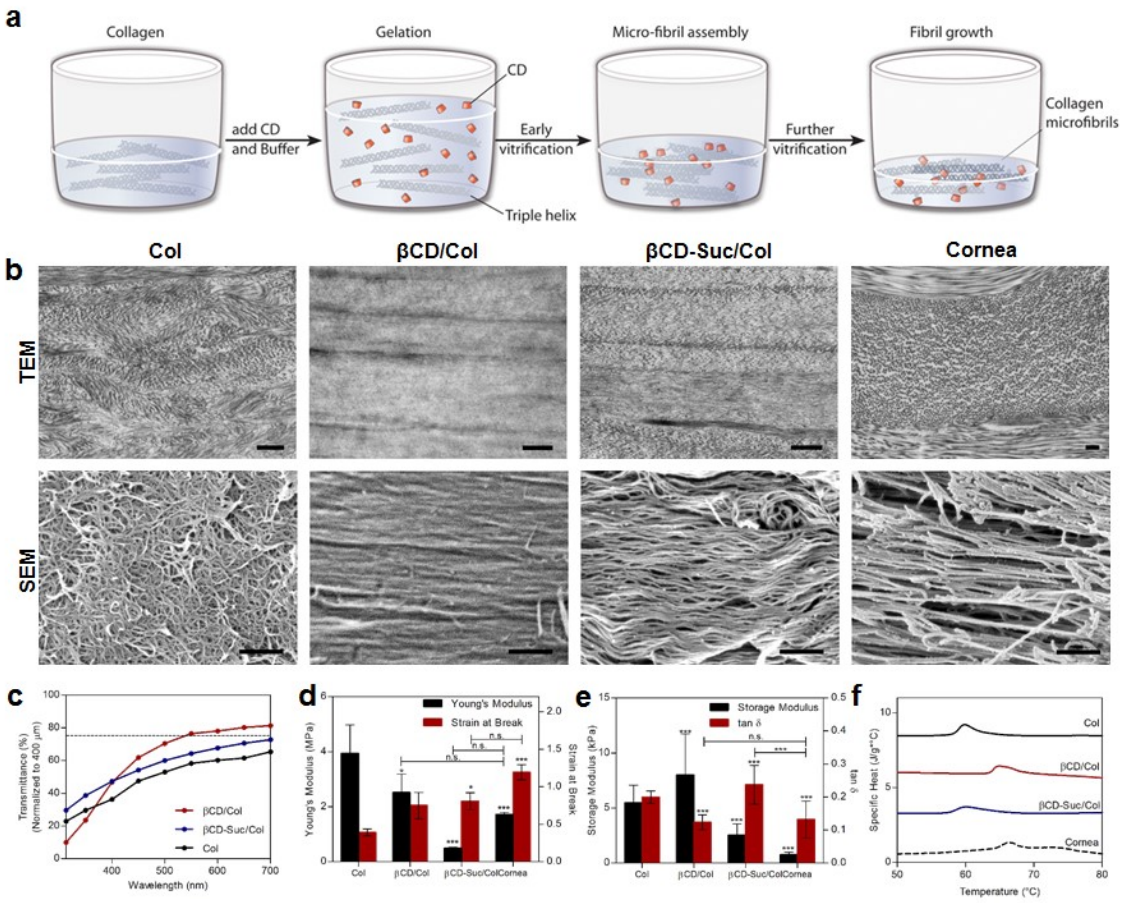

Figure 5.3 Cyclodextrin functional groups define collagen fibril organization, transparency and mechanical properties. a) Vitrigels manufactured by mixing equal volumes of collagen and CD-buffered solution causing gelation and micro-fibrillar assembly followed by fibril growth and reorganization during controlled dehydration (vitrification). **b)** Transmission electron microscopy and scanning electron microscopy of Col, βCD, and βCD-Suc and native rabbit cornea, to demonstrate effect of CD functionality on collagen ultrastructure organization. Scale bar = 500 nm **c)** Light transmission over visible light spectrum of vitrigel formulations (normalized to 400 μm) with and without incorporation of cyclodextrins, **d)** Young's modulus and strain at break measurements to monitor tensile properties of vitrigels following cyclodextrin incorporation. **e)** Oscillatory rheological properties of vitrigel formulations with cyclodextrin functionalization. **f)** Differential scanning calorimetry thermograms to determine thermal stability of vitrigels following incorporation of CD. Data are means ± SD, $n \geq 3$ (representative of at least two independent experiments), analysis of variance (ANOVA) with Bonferroni's post-test [(d) and (e)]: ***$P < 0.0001$, **$P < 0.001$, *$P < 0.01$ compared against Col unless otherwise specified.

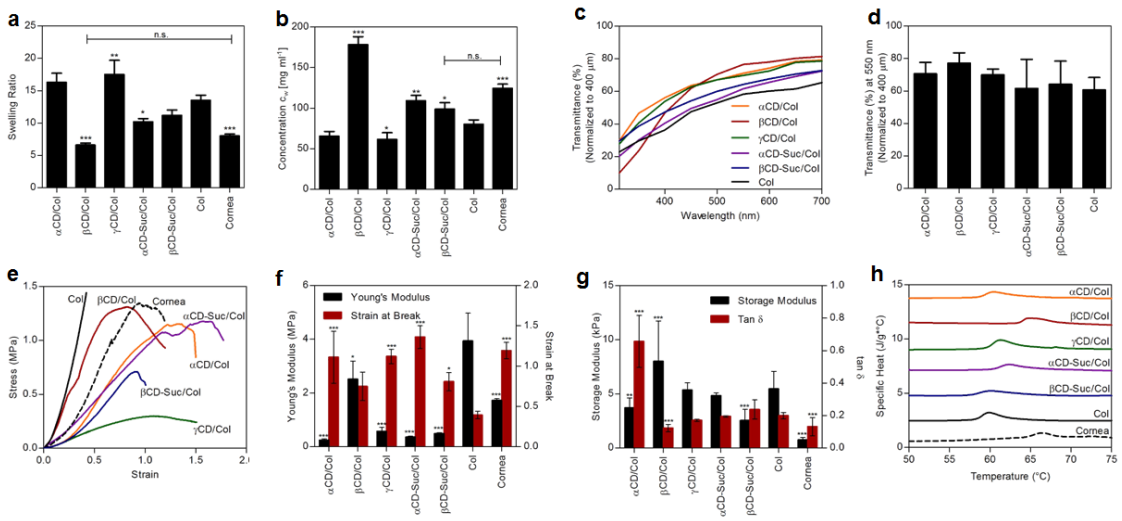

Figure 5.4 Further physical characterization of selected CD/Col materials. a) Swelling ratio determined as a ratio between fully hydrated vitrigel weight and weight following lyophilization. **b)** Theoretical collagen concentration in final vitrified product. **c)** Light transmission over visible light spectrum of vitrigel formulations with and without incorporation of cyclodextrins after initial screening, normalized to 400 µm. **d)** Light transmission values of the materials at 550 nm. **e)** Tensile stress-strain curves of vitrigel strips to evaluate elastomeric behavior following CD incorporation. **f)** Simultaneous comparisons of elastic modulus and strain at break for each vitrigel formulation to assess viability as corneal substitutes. **g)** Oscillatory rheological analyses of CD incorporated vitrigels to determine viscoelastic properties, **h)** DSC thermograms to quantify thermal stabilization following incorporation of various CD molecules. Data are means ± SD, $n \geq 3$ (representative of at least two independent experiments), analysis of variance (ANOVA) with Bonferroni's post-test: ***$P < 0.0001$, **$P < 0.001$, *$P < 0.01$, compared against Col unless otherwise specified.

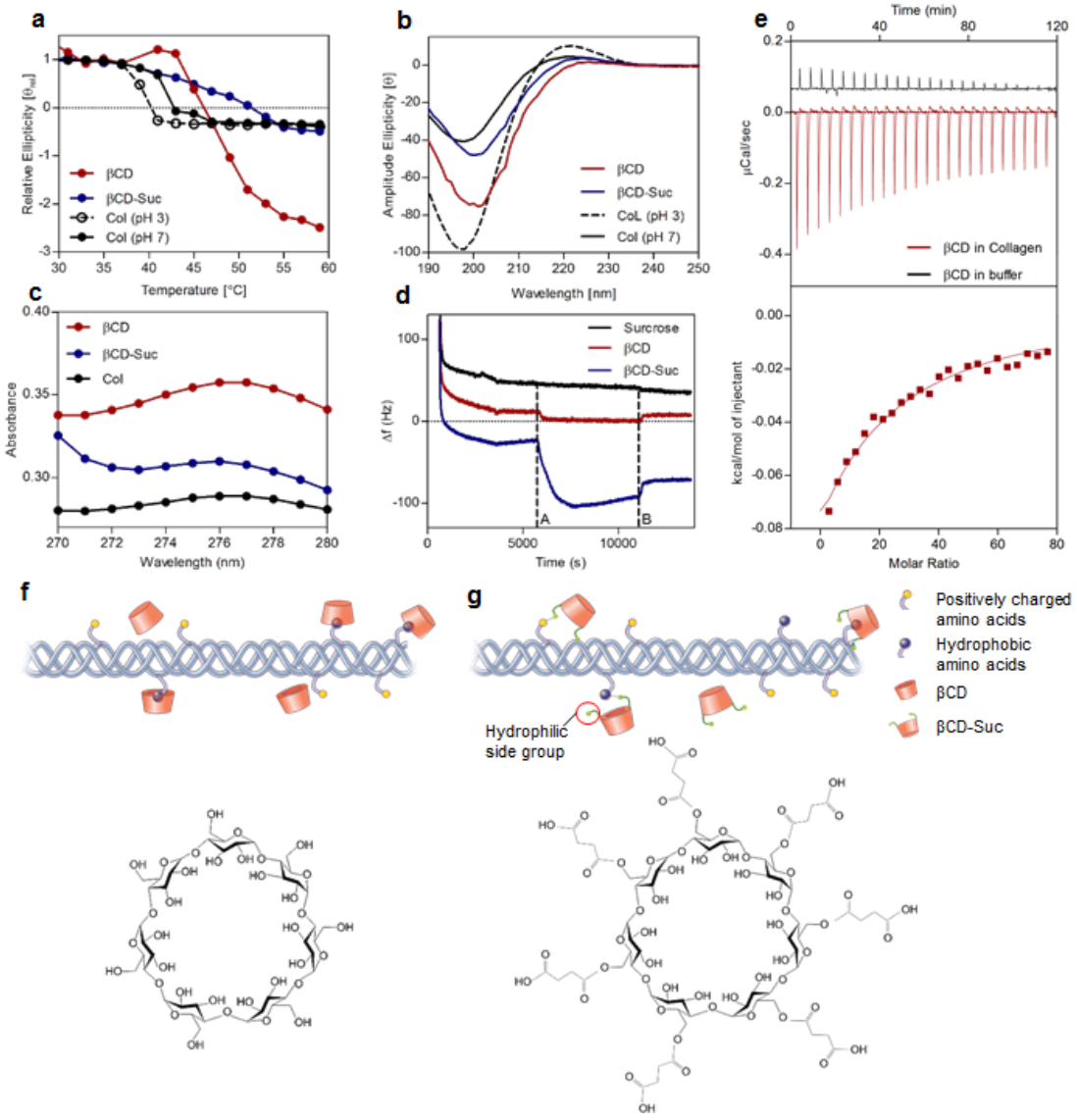

Figure 5.5 Collagen-cyclodextrin molecular interactions and effect on fibril formation. a) Circular dichroism spectroscopy among groups to demonstrate changes in thermal stability following molecular interactions between soluble collagen and βCD, **b)** CD spectrum of collagen triple helix with and without CD at a temperature of 5ºC. **c)** Shift in UV-visible light spectrum absorbance peak following incorporation of βCD and βCD-Suc into soluble collagen. **d)** Frequency change associated with βCD and βCD-Suc deposition and binding to collagen coated substrate via QCM analyses (frequency overtone n=5). **e)** Quantification of binding affinity of βCD with collagen via ITC at 20ºC. **f)** Schematic showing interaction of collagen hydrophobic groups with hydrophobic inner core of βCD and chemical structure, **g)** Incorporation of βCD-Suc in collagen involves additional interaction of the highly hydrophilic succinyl side chains and βCD-Suc chemical structure.

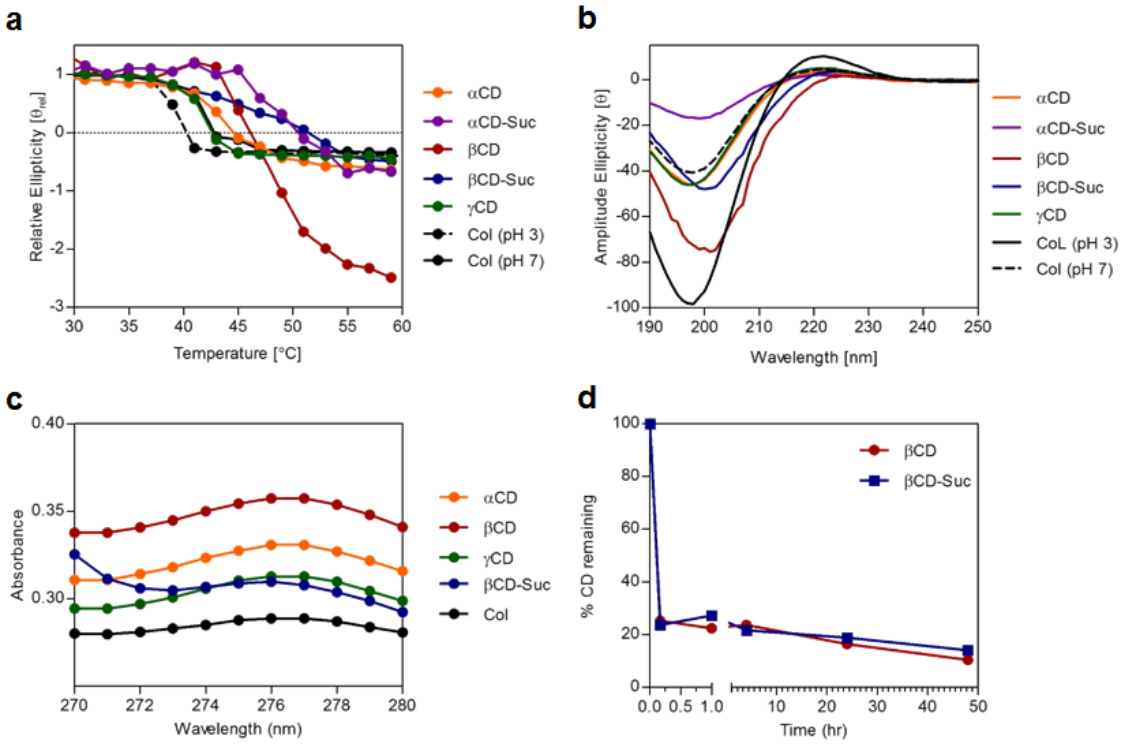

Figure 5.6 Selected CD/collagen molecular interactions and consequent release from bulk material. a) Circular dichroism spectroscopy demonstrates temperature shifts when following interactions of collagen with different CDs. **b)** CD spectrum signal of the characteristic collagen triple helix curve is suppressed to various levels with different CDs indicating potentially limited fibril formation. **c)** CD interacts with collagen aromatic groups causing a blue-shift in wavelength and an increase in absorbance peaks, observed in the UV-visible wavelength spectrum. **d)** Majority of βCD and βCD-Suc release from vitrified implants on rehydration, indicating stable structural/chemical changes caused by CDs during vitrification.

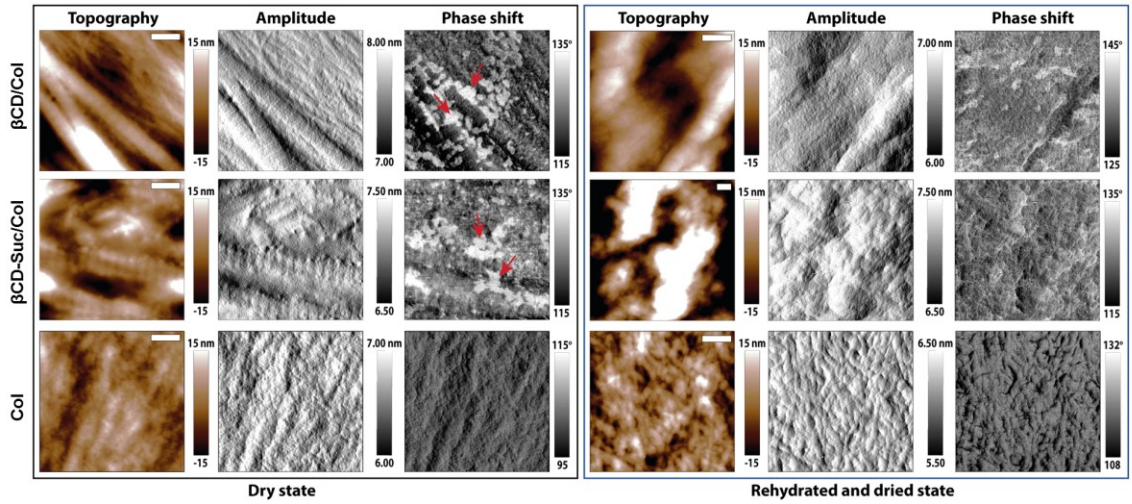

Figure 5.7 Topography, amplitude and phase shift response of cornea mimetic material observed by AFM for dried and rehydrated samples. Hydrophilic areas (indicated by arrows) close and around collagen fibers can be observed in the phase shift channel of the dried samples. These areas, present only in the samples with CD addition, cannot be observed in the equivalent rehydrated samples. Scale bar 200 nm.

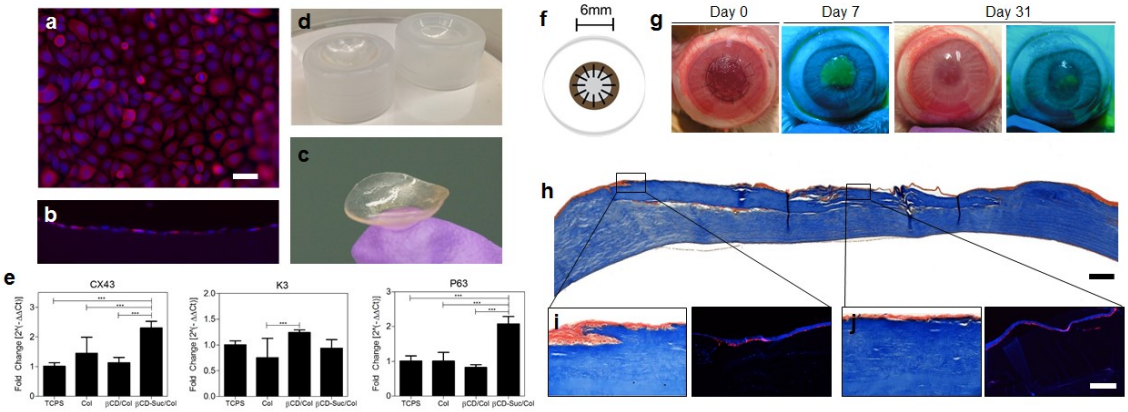

Figure 5.8 Cellular compatibility and surgical in vivo performance of biomimetic collagen-CD implants. a) Proliferation of primary rabbit corneal epithelial cell on CD/Col materials and staining for K14 (red) and DAPI (blue) on βCD/Col vitrigels. Scale bar = 20 µm **b)** Cross-section of in vitro epithelial cell culture on βCD/Col with K14 and DAPI staining, **c)** Custom molds used for manufacturing implants with desired curvature. **d)** Lenticularly shaped βCD/Col corneal implants with curvature of healthy cornea. **e)** qPCR with epithelial cell culture on vitrigels to determine regulation of genetic markers CX43, K3 and P63. **f)** Schematic of in vivo implantation of corneal implant and affixation using interrupted sutures. **g)** Gross images of the in vivo ocular surgery in the rabbit model over 31 days and fluorescein staining (under blue light) to monitor progress of reepithelialization over βCD/Col implant. Yellow staining under blue light indicates regions of the implant without epithelial cell coverage. **h)** Histological analysis of sections stained using Masson's Trichrome to visualize implant after 14 days. Scale bar = 100 µm. **i-j)** Immunostaining for laminin (red) and DAPI (blue) in peripheral and central wound regions. Laminin proteins are expressed by epithelial cells after maturation. Scale bar = 50 µm. Data are means ± SD, n = 6 (representative of at least two independent experiments), analysis of variance (ANOVA) with Bonferroni's post-test [(e)]: ***P < 0.0001

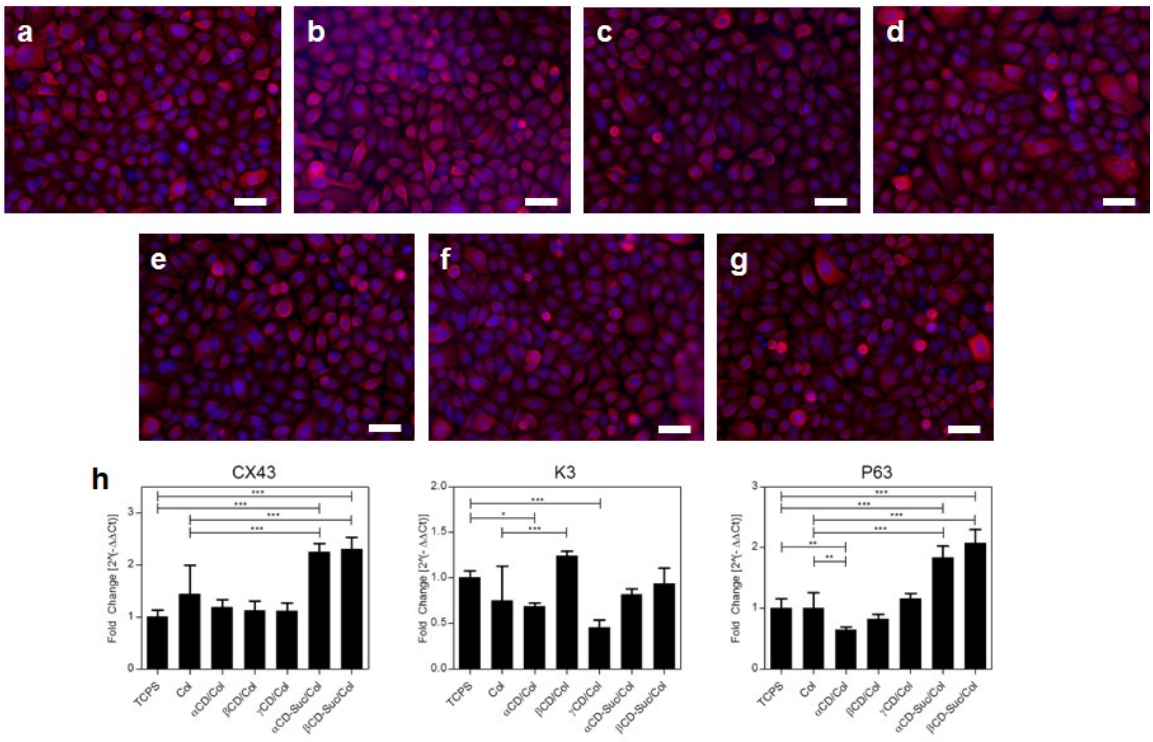

Figure 5.9 Immunocytochemistry and qPCR of rabbit corneal epithelial cells grown on several different CD/Col substrates with staining for K14 counterstained with DAPI as indicated for a) αCD/Col, **b)** βCD/Col, **c)** γCD/Col, **d)** αCD-Suc/Col, **e)** βCD-Suc/Col, **f)** Col only, **g)** Tissue culture treated polystyrene (TCPS). Scale bar: 20 μm. **h)** qPCR of key epithelial markers CX43, K3, and limbal stem cell marker P63. Data are means ± SD, n = 6 (representative of at least two independent experiments), analysis of variance (ANOVA) with Bonferroni's post-test [(e)]: ***$P < 0.0001$

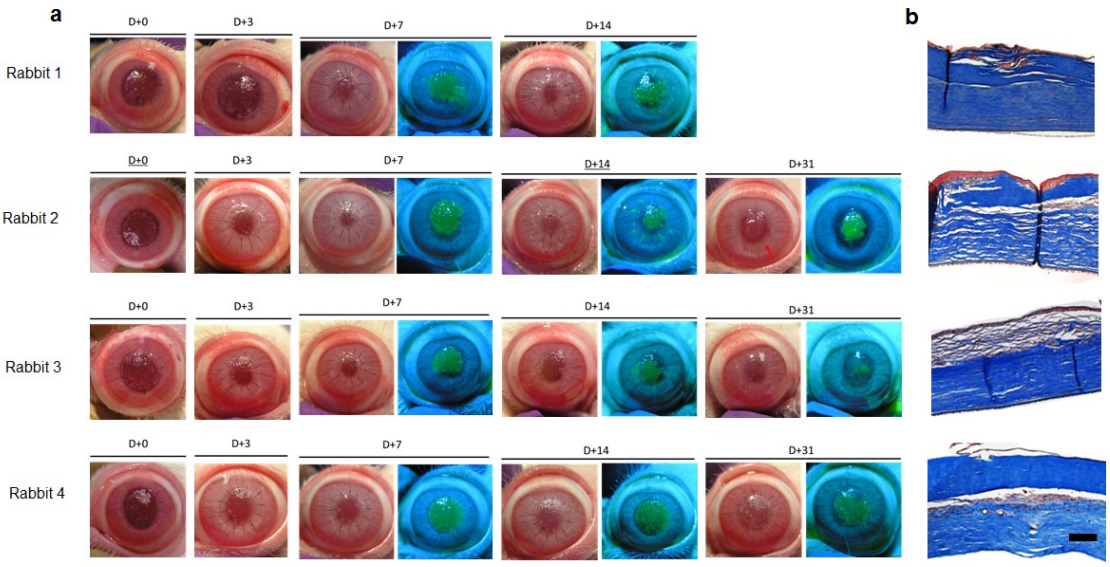

Figure 5.10 In vivo surgical compatibility of βCD/Col implants in rabbits. a) Implantation of CD vitrigels as corneal implants via anterior lamellar keratoplasty using interrupted sutures, and observation of healing process (gross images) and reepithelialization (using fluorescein dye, under blue light) over 31 days. **b)** Histological sectioning and staining using Masson's Trichrome to demonstrate survival and integration of the implants. Scale bar = 100 µm.

6. A versatile approach to modulate collagen fibrillogenesis to alter optical and biological properties of corneal implants.

6.1. Introduction

The cornea is primarily made of collagen and is uniquely transparent owing to a highly organized and complex structure. It is an avascular tissue consisting of three major layers: the outermost epithelium, the stroma, and the innermost endothelium, which regulates the water content of the stromal layer through an active pumping mechanism [147]. The stroma represents over 90% of the total cornea, sparsely populated with keratocyte cells and composed mainly of type I collagen extracellular matrix molecules and smaller percentages of type V collagen and proteoglycans. The corneal stroma also has a unique structural organization of approximately 200 lamellae, each 2-μm thick, which contribute to the mechanical strength and transparency of the tissue [18]. Although corneal transplants are considered successful surgical procedures for many indications, rejection and mechanical failure (non-immunologic loss of corneal clarity over time) are common, especially for younger patients and those with ocular comorbidities. Furthermore, the pool of donor tissue is decreasing globally owing to the increased rates of surgery for refractive correction. Alternative options for repairing corneal injury and scarring are needed, and an off-the-shelf material that mimics the native cornea would be transformational.

Using a collagen vitrification process, we created synthetic corneal implants with increased mechanical strength and beneficial cellular interactions compared to standard collagen gels. Specifically, collagen membranes with fibrillar structures were developed in collaboration with Dr. Toshiaki Takezawa, the inventor of collagen vitrigels [32,33,34]. The vitrification process cures collagen gels at a defined humidity and temperature to control water evaporation so that collagen macromolecules can organize into fibrils. In collaboration with the Applied Physics Laboratory (APL), processing conditions were further optimized to reduce vitrification time and to increase

mechanical strength and transparency of the gels [35,136], and exhibit biophysical properties superior to standard amorphous collagen gels. Furthermore, the fibrillar structure of the collagen vitrigel allowed cultured keratocytes to maintain their in vivo phenotypes (defined by morphology and gene expression) more than amorphous collagen gels or tissue culture polystyrene, where cells typically became fibroblastic [33,36]. These vitrified collagen membranes also demonstrated biocompatibility in vivo in partial corneal defects in a rabbit model [37]. However, these membranes were thin (~50 μm), whereas the natural cornea is humans 500 μm.

The next challenge was therefore to create an implant with a thickness similar to the full-thickness cornea. Unfortunately, if we simply extended the vitrification process to larger collagen gels on the order of the thickness of the human cornea, the implants would lose clarity due to light scattering by the unevenly distributed fibril diameters, lack of fibril alignment, and non-physiological interfibrillar spacing. During corneal development, collagen fibrillogenesis is a multiple-step process that is tightly regulated by the interaction of many molecules. In this process, small leucine-rich proteoglycans (SLRPs) bind to the collagen protofibril surface to regulate linear and lateral fibril growth during maturation, thus resulting in a "corneal block," wherein fibril diameters are limited and organization occurs in such a way to allow for proper refraction of light and transparency [128,148,149,150]. Therefore, we developed a strategy to create a full-thickness corneal implant that would have adequate mechanical properties for suturing and maintenance in the eye, as well as transparency and biocompatibility. The novel material is based on the vitrification of collagen combined with cyclodextrins (CD), which are small cyclic oligosaccharides that comprise a family of cyclic oligomers containing a ring of six to eight glucose molecules. These ring molecules feature an inner hydrophobic core and an outer hydrophilic ring that can form complexes with small molecules or portions of large compounds [151,152]. The CD molecules play a role similar to SLRPs during development, chaperoning collagen fibers during the vitrification process. CD serves as a proteoglycan substitute by forming specific interactions

with the collagen triple helices to control fibrillogenesis, but not fully interrupt fibril formation. CD also facilitates the formation of lamellar layers with thicknesses close to that observed in native cornea. Here, we propose to develop a library of CD-collagen (CD-Col) materials to characterize and understand mechanistically how the biomimetic structure is created and to translate the technology in the development of a cornea implant.

While preliminary in vitro and in vivo experiments demonstrate biocompatibility of the biomaterial, there are several challenges that needed to be addressed. The lamellar nature of the CD Col implants could allow epithelial migration into the lamellae instead of over the implant. Re-epithelialization over the implant may be impaired, which could eventually cause material loss, degradation and corneal graft failure. To bolster epithelial cell migration, several strategies may be used including material surface modification by chemically crosslinking cell attachment peptides such as RGD, and modification of implant design and surgical strategies to better fit or cover the surface. The CD Col material formulation also demonstrated surface roughness which could potentially slow down epithelial migration speed. While these properties were excellent for a corneal stromal substitute, they may not be ideally suited for enhanced reepithelialization.

Several factors such as pH, temperature and ionic strength help modulate collagen gelation and fibril formation. CD-Col materials were originally prepared by increasing the pH of the collagen solution to pH 7 by mixing in a buffer, followed by vitrification and rehydration. In this current chapter, we aim to influence fibrillogenesis in ‘vitrigel’ biomaterials through alternative gelation techniques using ammonia gas permeation, and assess the role of fibrillar networks in optical and biological properties and performance in vivo. This dramatically decreases the required starting volume of the collagen (no buffer mixing required) as well as decreases the vitrification/dehydration time for thicker implants. Additionally, the buffer mixing process could amount to some human error and potentially results in formation of bubbles or uneven gelation, in addition to being a highly labor-intensive process. The use of ammonia to neutralize acidic collagen

solution, allows for a one step process that does not involve mixing of multiple solutions and maintains high starting concentration of collagen in the initial mixture. CD can be pre-dissolved in the acidic collagen solution as required.

Previous studies which dealt with gelation of collagen through ammonia vapors expose collagen to ammonia for an approximate amount of time until gelation is complete, followed by equilibration in buffer, most often for periods of 24 hours or more[153,154]. However, we have delved into exploring the effects of ammonia over- and under-exposure on collagen in the formation of gels. Moreover, we have studied the biomaterials thus formed in the context of vitrification, following the ammonia mediated collagen (AMC) gelation. The changes in exposure time was able to confer control over the fibrillar structures formed during gelation. These fibril structures were further amplified during the vitrification process and resulted in transparent, strong and flexible sheets of collagen. Using the AMC gelation technique, we were able to control the optical properties of the collagen biomaterials thus formed. Highly transparent AMC materials were then successfully used as corneal transplant materials.

6.2. Methods

6.2.1.AMC vitrigel preparation

Acidic collagen type I (CosmoBio) at 5 mg/mL concentration and pH 3 was used. Specified volumes of collagen solution were dispensed into plastic molds maintained at 4°C. In a closed chamber, ammonium hydroxide maintained at 25°C was allowed to interact with degassed collagen solution. Collagen was exposed to ammonia vapors in desiccation chamber at room temperature for 3 min, 30 min and 2 h. Collagen gels were then removed from ammonia chamber and incubated in 5°C vitrification chamber for 90 minutes, followed by a 30-minute incubation (gelation) at 37°C. Samples were vitrified in a 5°C vitrification chamber overnight followed by a 37 °C and 40% RH for 3 days. The biomaterials were then rehydrated in 20 mM HEPES for 24 hours.

6.2.2. ***Second Harmonic Generation Microscopy***

To observe fibrillogenesis of AMC vitrigels, two-photon microscopy was performed using a Zeiss LSM-710 microscope (Carl Zeiss, Jena, Germany. Illumination was performed at a wavelength of 790 nm. Collagen fibrils were detected by its second-harmonic generation (SHG) signal below 480 nm. Images were recorded as z-stacks overarching the whole membrane with 1 μm Z-spacing using Zen software 2009 (Carl Zeiss).

6.2.3. ***Light Transmission***

AMC vitrigels were cast in microplate wells, vitrified, rehydrated and measured using a standard multi-plate reader Synergy 2 (Biotek). Area scan measurements were made at over the visible spectrum at 50 nm intervals. Data was compiled and analyzed in Excel.

6.2.4. ***Scanning Electron Microscopy***

AMC vitrigels were fixed with 4% PFA, gradually dehydrate with 30%-100% ethanol, and dried with HMDS overnight. Samples were sputter coated with 20 nm AuPd and imaged with Leo FESEM.

6.2.5. ***Tensile Testing***

A Bose EnduraTEC ELF3200 (Bose ElectroForce, Framingham, MA, USA) was to determine the stress-strain behavior of AMC materials. Samples (n=6 for each group) were cut in 5mm strips, and sample width and thickness was measured. The AMC materials were affixed using super glue and sandpaper to prevent slippage. Load /displacement measurements were recorded and analyzed.

6.2.6. ***Ex vivo migration model for tracking corneal reepithelialization***

Implants of 6 mm diameter were surgically inserted into an *ex vivo* cornea after creation of a partial pocket model with a 4-mm anterior wound. The corneas with the implants were then cultured in full media (DMEM + 10% FBS) up to 72 hours and reepithelialization and epithelial cell maturation was tracked. Reepithelialization was tracked using fluorescein dye stain.

6.2.7. ***In vivo experiments***

New Zealand white rabbits were used for surgery. Under general anesthesia with Ketamine (35mg/kg of body weight) and Xylazine (5mg/kg of body weight) administered intramuscularly, partial keratectomy was conducted. After applying one to two drops of topical anesthetic (Proparacaine drops) the cornea was scored for a depth of about 150μm using a 6 mm Hessburg-Barron vacuum trephine. The corneal button was removed using an ophthalmic crescent knife, following which, oversize implants (6.5 mm) of AMC vitrigels were carefully placed on the wounded cornea. The thickness of the corneal wound depth was closely matched to material thickness. 4 overlay sutures were used to secure materials in place using 10-0 nylon sutures. After surgery, atropine drops were applied once a day or every other day for five days depending on the amount of iris dilation to prevent cycloplegia. A mixture of anti-biotics and anti-inflammatory ointment was applied to the operated eye once daily for 14 days, and once every 36 hours till day 21. Additionally, to reduce the pain, systemic analgesic (Meloxicam) was applied for 3 days via intramuscularly. Ophthalmic examinations were conducted at 3 days, 1 and 2 weeks post-surgery. To evaluate the functional re-epithelialization, 0.05% fluorescein dye was applied under blue light at day 7, 14, 21, and 30-day time points. Following the 31-day time-point, the animal was sacrificed, and the eye globes removed and fixed for further histological processing.

6.2.8. ***Histology***

Following fixation in 10% Formalin, samples underwent standard graded dehydration procedure in ethanol, followed by xylene treatment. After overnight paraffin infiltration, samples were embedded in paraffin wax and sectioned using a microtome at 5 um thickness. Slides were treated for Hematoxylin and Eosin staining as well as Masson's Trichrome staining.

6.3. Results and Discussion

6.3.1. ***Using ammonia to modulate collagen fibrillogenesis***

Collagen at acidic pH and at low temperatures is relatively stable as an aqueous solution. The temperature and pH of collagen can be gently raised in order to initiate gelation. The lab setup used to create the AMC gels reproducibly (**Figure 6.1**) consists of a water bath to control the temperature of ammonium hydroxide (thereby enabling the control of ammonia release) and a closed sealer container wherein the collagen solution was exposed to the high pH ammonia vapors for a stipulated time. Following gelation in the sealed chamber, the gels are then vitrified and rehydrated as per standard procedure (**Figure 6.1B**), to increase collagen concentration and create strong and transparent membranes (**Figure 6.1C**).

6.3.2. ***Type I Collagen source and processing affect AMC vitrigel characteristics***

AMC gels were prepared from type I collagen extracted from human neonatal fibroblast cell-culture ECM (Vitrocol), rat tail tendon (Gibco) and native bovine dermis (CosmoBio). It was observed that the AMC vitrigels prepared from bovine collagen had greater transparency than human and rat collagen AMC vitrigels (**Figure 6.2a**). AMCs formed using human collagen Vitrocol were mechanically the weakest and thinnest and handling with forceps caused material disintegration. The relative increase in transparency and mechanical strength of bovine collagens could be attributed to the higher number of aromatic groups (Phe and Tyr) in bovine collagen as compared

to human and rat collagens. Since human and rat tail collagens were pepsin solubilized, they do not possess telopeptides. It can be expected that presence of the telopeptide in bovine collagen allowed the formation of a more robust gel. AMC vitrigels from different sources however did not demonstrate a large difference in thermal denaturation peaks (**Figure 6.2b**) indicating that the collagen fibril formation between the different groups is not dissimilar.

6.3.3. ***Evidence of layering and alignment using Second Harmonic Generation microscopy***

Given this preliminary data, bovine collagen was chosen for the next experiments. AMC gels with bovine collagen were allowed to be in contact with ammonia gas for varying amounts of time. The duration of ammonia exposure significantly affects the properties of the final material. This was observed using Second Harmonic Generation microscopy (**Figure 6.3a**). Fibrillar collagen has a highly crystalline triple-helical structures which generate the second harmonic of incident light. Therefore, SHG microscopy is now widely used to detect the fibrillar structures of collagen in vitro or in vivo. In this study, SHG revealed the differences in fibrillogenesis of AMC vitrigels that exposed to Ammonia for different time duration. With short ammonia exposure time of 3 min (A3G30), fibrillogenesis occurred merely on the top and bottom surfaces of the membrane with over 150 μm in thickness. Thick fibrils scattered on the top and bottom surface, no SHG signal was detected in the middle of the membrane according to the Z-stack images. As the exposure time increases to 30 min (A3G30) and 120 min (A2hG30), more collagen fibrils with SHG signal appeared while fewer thick fibrils were observed as compared to the A3G30 group.

The transparency of the vitrigels correspond to degree of fibrillogenesis. AMC vitrigels were prepared at physiologically relevant thicknesses, and measured using a microplate reader. Transparency of the AMC gels decreased with increased ammonia gelation time (**Figure 6.3b**). Gels in contact with ammonia for 3 minutes were more transparent than gels exposed to ammonia

for 2 hours after vitrification and rehydration. AMC vitrigels were observed to demonstrate very low light scattering as observed from gross pictures after vitrification (**Figure 6.1c**). It was observed that the AMC vitrigels demonstrated excellent transparency over the range of the spectrum.

6.3.4. ***Ultrastructural and mechanical characterization***

AMC materials were also imaged using the SEM to ascertain surface topography. As initial SHG results implied, AMC demonstrated consistent and uniform fibrils with the characteristic d-banding (**Figure 6.4a**). The top view of the AMC vitrigels shown demonstrate that the materials have a relatively smooth surface with "star shaped" self-assembled collagen bundles. As the gelation time increases, a larger number of mature collagen bundles were observed. Small sized collagen fibrils are distributed underneath the thick collagen bundles on the surface. Longer gelation time corresponds to assembly of thinner fibrils into thicker fibers. These findings demonstrate that within a defined surface area (in our case, a 35mm petri dish) and volume (5ml), ammonia exposure duration can be used as a measure to directly influence the collagen fibril structure. The differences observed in the fibrillar diameter and density may also affect macroscopic properties such as mechanical strength.

In order to determine the mechanical characteristics of AMC vitrigels, tensile testing was performed. AMC vitrigels were rehydrated and cut into standard size test coupons and subjected to uniaxial tensile force. It was observed that there were no significant differences between the Young's moduli of the vitrigels regardless of exposure time (**Figure 6.4b**), although they were consistently higher than a cornea control. Young's moduli of these membranes were seen to be in the same range as of the previous βCD materials that the lab has produced. Further, the strain at break values for all samples (**Figure 6.4b, c**) also remained nearly constant at around 45% elongation, notably much lower than that of native corneal tissue.

6.3.5. ***Preliminary development of an ex vivo model for corneal reepithelialization***

In order to assess the reepithelialization potential of materials using a fast and reliable procedure as a first step, before *in vivo* animal implantation, we created and optimized an *ex vivo* cornea culture protocol. Implants of 6 mm diameter were surgically inserted into an *ex vivo* cornea after creation of a partial pocket model with a 4-mm anterior wound (**Figure 6.5a**). The corneas with the implants were then cultured in full media (DMEM + 10% FBS) up to 72 hours and reepithelialization and epithelial cell maturation was tracked. Reepithelialization was tracked using fluorescein dye stain (**Figure 6.5b**). Full reepithelialization in AMC materials was observed within 72 hours, significantly faster than in the negative control implant material (chemically crosslinked collagen gels which have been previously tested *in vivo* and failed to reepithelialize). Epithelialization over the AMC implants, while retarded epithelialization in a material that does not work *in vivo*, is a promising sign for the validity of the experiment.

Histological sections of the AMC implants in the *ex vivo* culture (**Figure 6.6a**) also demonstrated full reepithelialization in full medium within the first 48 hours, as evidenced from previous studies. Healthy cell layer attachment to the AMC implants was observed and multilayered cell growth over the implant was observed by 48 hours. At 72 hours, characteristic squamous epithelial cell morphology was seen on AMC materials.

We further studied the maturation of epithelial cells on AMC materials in the *ex vivo* culture over time with immunofluorescence. Epithelial gene marker keratin 14 (K14) and tight junction protein ZO-1 were counterstained with DAPI on reepithelialized implants (**Figure 6.6b**). Marker expression following 24 hour in culture was relatively dim, indicating low maturation. Marker expression significantly improved at 48 hours and 72 hours of culture, where the epithelial cell layers expressed high levels of K14 and form uniform polygonal tight junctions observed via localized ZO-1 expression. These results indicate the AMC material not only supports epithelial

cell migration, but also support relatively fast maturation and differentiation. The merged images with DAPI, K14 and ZO-1 staining demonstrated cell maturation and marker expression on the AMC materials in *ex vivo* model. Negative control demonstrated incomplete coverage, with very low cell numbers, and inconsistent cell marker expression.

6.3.6. ***Guiding collagen fibrillogenesis via physical nucleation cues***

AMC materials were manufactured with liquid collagen in contact with a micropatterned mesh (**Figure 6.7a**) to initiate guided collagen fibril assembly. Fibrils formed in the collagen materials when in contact with micropatterns were observed via SHG microscopy (**Figure 6.7b**) and were observed to closely follow the pattern. Further, we studied the impact of fibrillar patterns and surface morphology on epithelial cell migration. Epithelial cell marker K14 and tight junction protein ZO-1 were stained to test the maturation of epithelial cells (**Figure 6.7c**). Cells tended to migrate along the pattern first, and then proliferate to cover the rest of the surface. Therefore, while cells can be patterned by simply modulating the underlying collagen fibril pattern, the migration rate itself was slower than a randomized fibril surface. The immunostaining demonstrated cells expressed K14 epithelial marker indicating the epithelial cells maintained the phenotype, however due to the surface geometry, very limited ZO-1 expression was observed. These results indicate that a relatively smooth surface is critical for tight junction formation.

6.3.7. ***In vivo surgical implantation of AMC material***

Curved AMC vitrigels were formulated using custom PDMS molds for *in vivo* use to determine epithelial migration and functional biocompatibility (**Figure 6.8a**). The implants were followed to assess degradation and epithelial migration (**Figure 6.8b**). The implants did not demonstrate any degradation, melting or related immune reactions. At day 14, AMC material demonstrated good attachment to host tissue. By day 31, full reepithelialization and stabilization of the implant was observed, accompanied by significant smoothening of the surface of the corneal wound and implant

region. Histological processing using Masson's Trichrome demonstrates full epithelial coverage, rapid implant integration and keratocyte infiltration. Further, immunofluorescence to assess epithelial layer basement membrane protein Laminin expression was performed on histological sections. Laminin expression was evident between the epithelium and implant. The high level of integration and relatively quick epithelial cell migration over the AMC surface is a positive indicator for success in future animal trials.

6.4. Conclusions

The new ammonia based method of manufacturing vitrigels demonstrates great potential in terms of increased surface smoothness, increased optical clarity and decreased light scattering as well as biological and functional compatibility. The production of AMC vitrigels through varying degrees of exposure to ammonia demonstrates that the collagen ultrastructure of vitrigels is tunable. Further, bulk material properties such as transparency can be modulated by changing the underlying ultrastructure achieved through the versatility of the gelation process involving ammonia exposure. AMC materials also demonstrate biocompatibility through *ex vivo* studies. The *ex vivo* corneal tissue culture model demonstrated that it mimics the *in vivo* wound healing process and confirmed the viability of its results through the negative control study. This biological model allows for a cheaper, faster and more physiological evaluation of biocompatibility of corneal substitutes than a simple *in vitro* cell culture or scratch migration testing. Moreover, the use of the novel *ex vivo* model will enable evaluation of reepithelialization mechanisms and wound healing processes prior to animal testing. Finally, the suturability, biocompatibility and integration of AMC with host corneas *in vivo* was also demonstrated. Therefore, the AMC materials could potentially aid in creating viable biosynthetic corneas with accelerated epithelial cell migration and maturation.

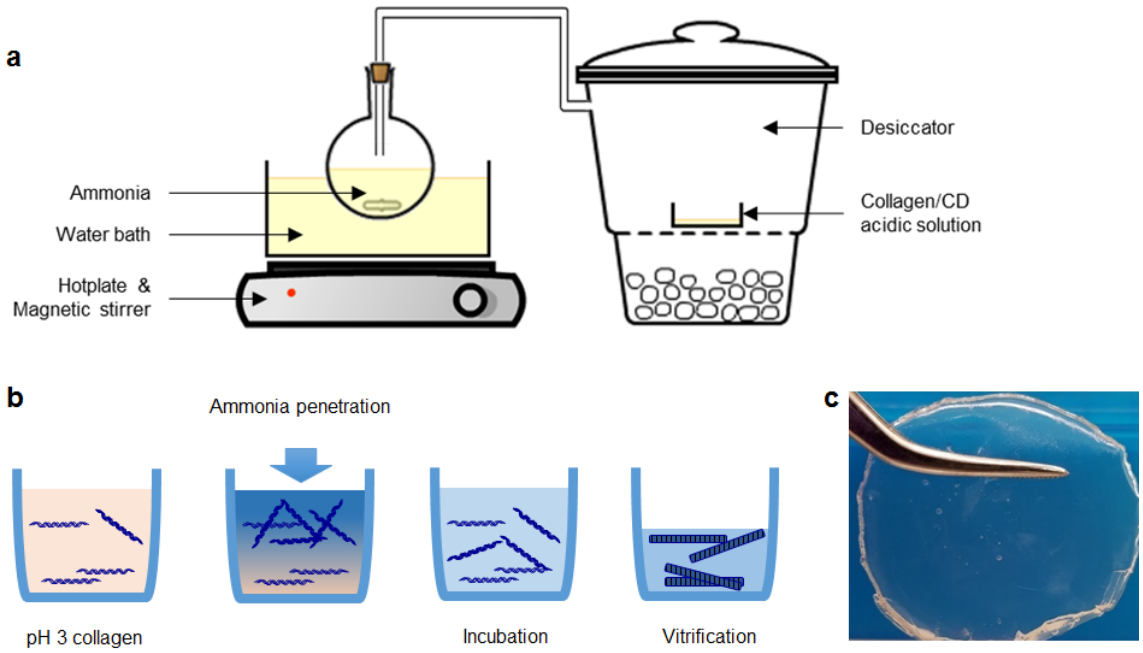

Figure 6.1 Schematics depicting ammonia mediated collagen gelation. a) Laboratory setup for controlled ammonia exposure on collagen materials. **b)** Fibril formation during ammonia penetration and gelation during the process of manufacturing AMC vitrigels. **c)** Gross picture of 35 mm diameter, 500 µm AMC vitrigel.

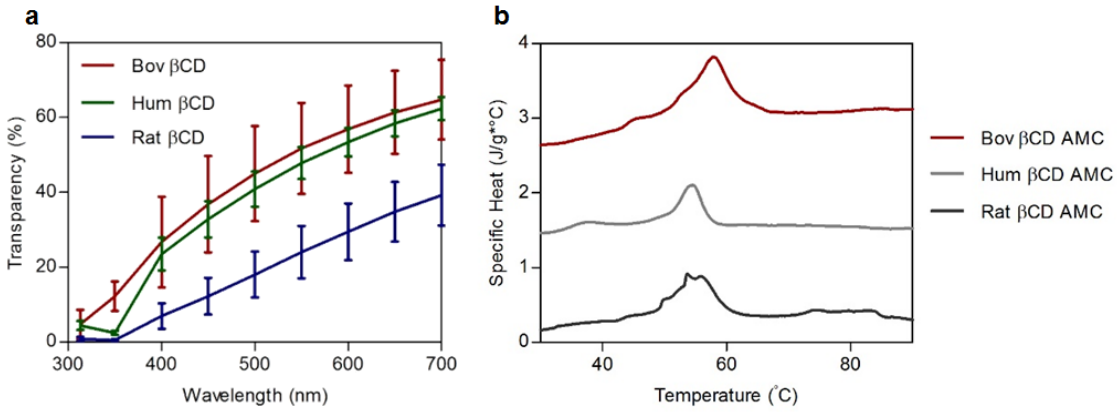

Figure 6.2 AMC vitrigel formulations with different collagen sources demonstrate differences in physical characteristics. a) Transparency of collagen vitrigels from different collagen sources, **b)** thermograms depicting collagen stability of vitrigels from collagen source.

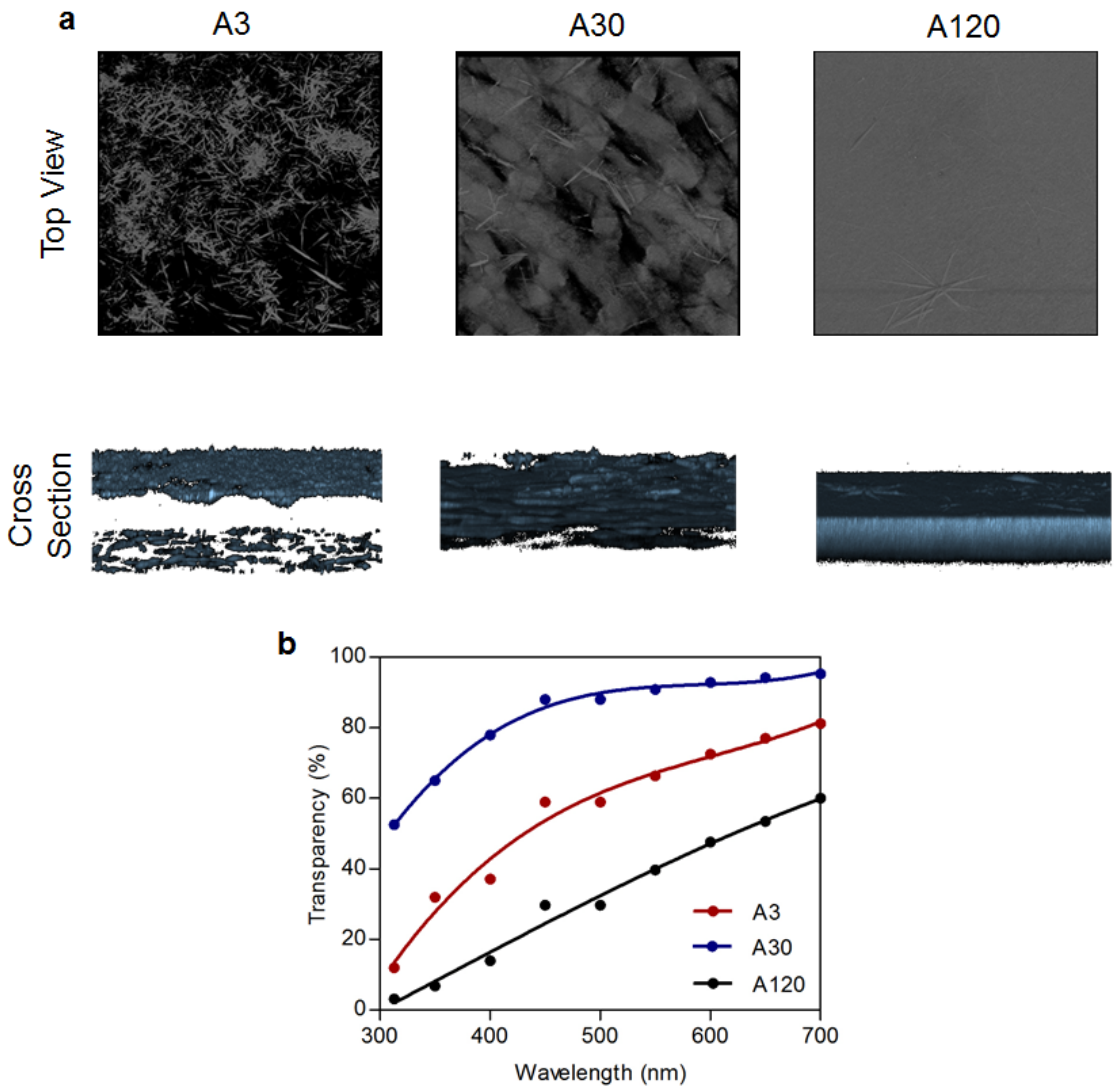

Figure 6.3 Duration of ammonia exposure causes changes in ultrastructure and optical characteristics of AMC materials. a) Second harmonic generation microscopy Z-stack imaging of AMC vitrigels with different exposure times, **b)** Transparency of AMC vitrigels change dramatically with different durations of ammonia exposure. Gelation times were constant at 30 min.

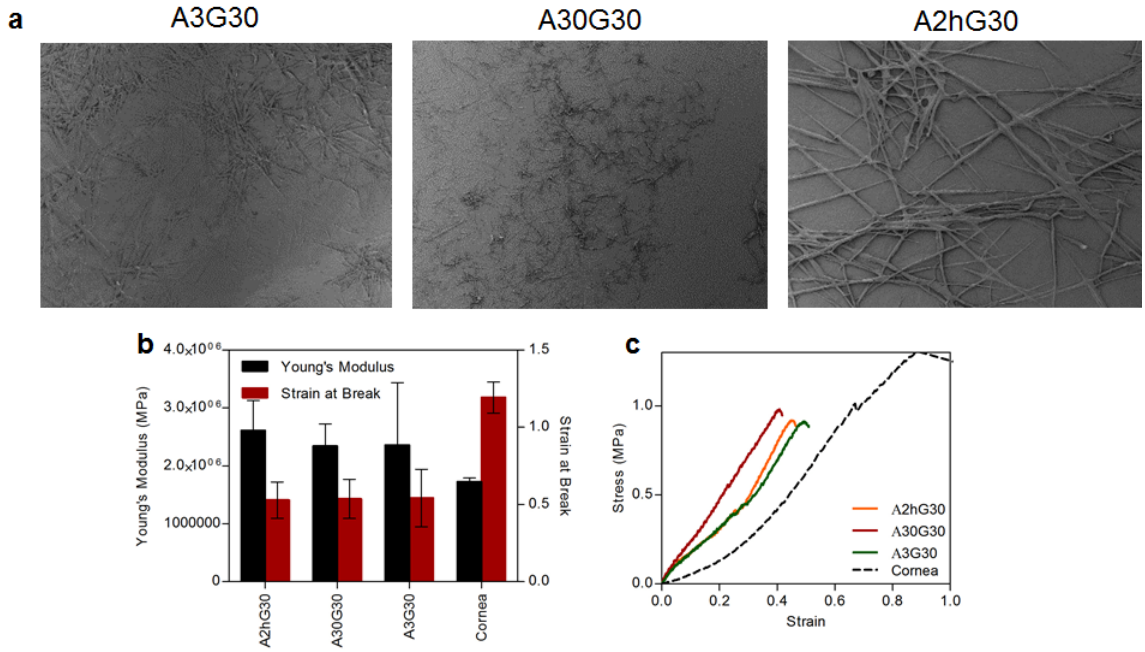

Figure 6.4 Ultrastructural changes and tensile properties of AMC with varying exposure times. a) SEM images of AMC vitrigels demonstrating fibrillar surface topography, **b)** Young's modulus and Strain at Break for various AMC materials. c) Representative stress-strain curves for AMC materials.

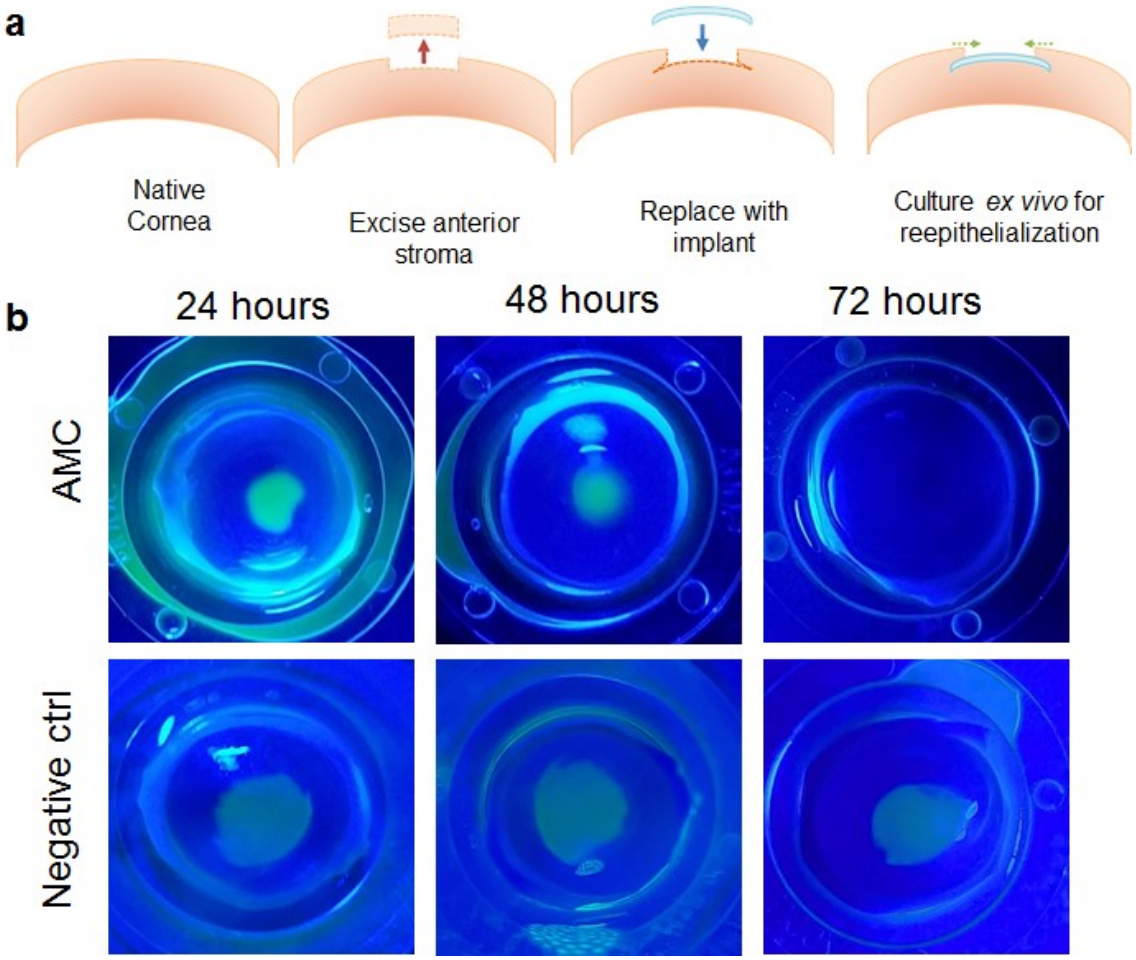

Figure 6.5 Development of ex vivo culture model for tracking corneal reepithelialization. a) Schematic depicting ex vivo corneal surgery and implantation of AMC materials, **b)** Fluorescein dye staining and imaging under blue light to track epithelial wound area (in yellow-green).

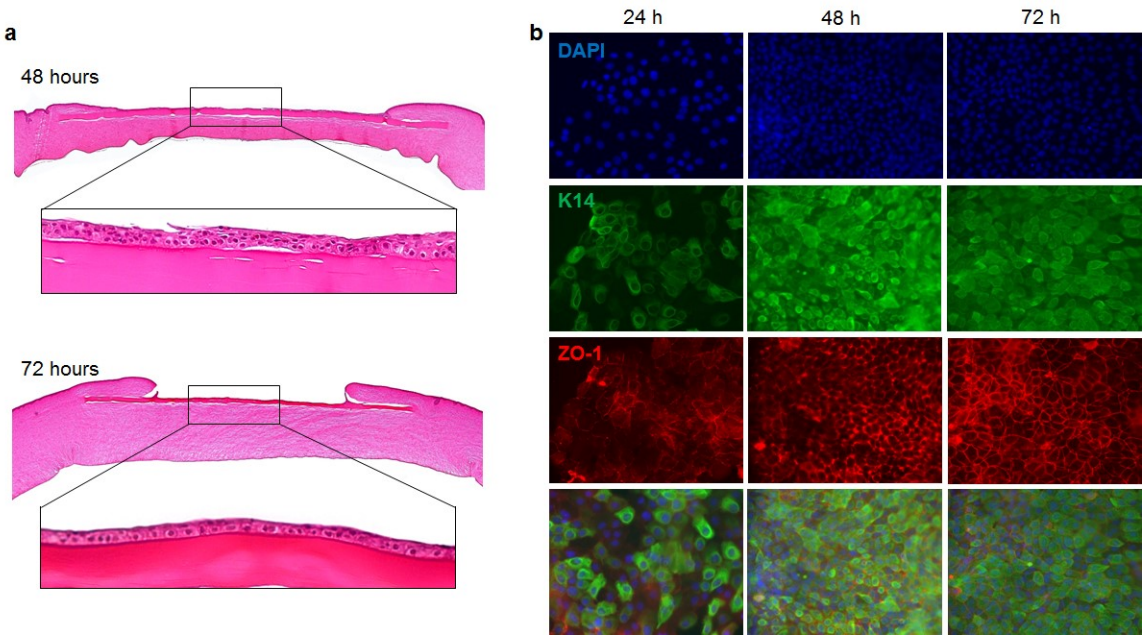

Figure 6.6 Histology and immunofluorescence of ex vivo AMC corneal cultures. a) H&E staining of corneal sections to demonstrate multicellular epithelialization, **b)** Immunofluorescence marker expression for nucleus (DAPI), keratin-14 (K14) and tight junction protein (ZO-1) in AMC materials to track epithelial cell maturation over 24 h, 48 hand 72 h.

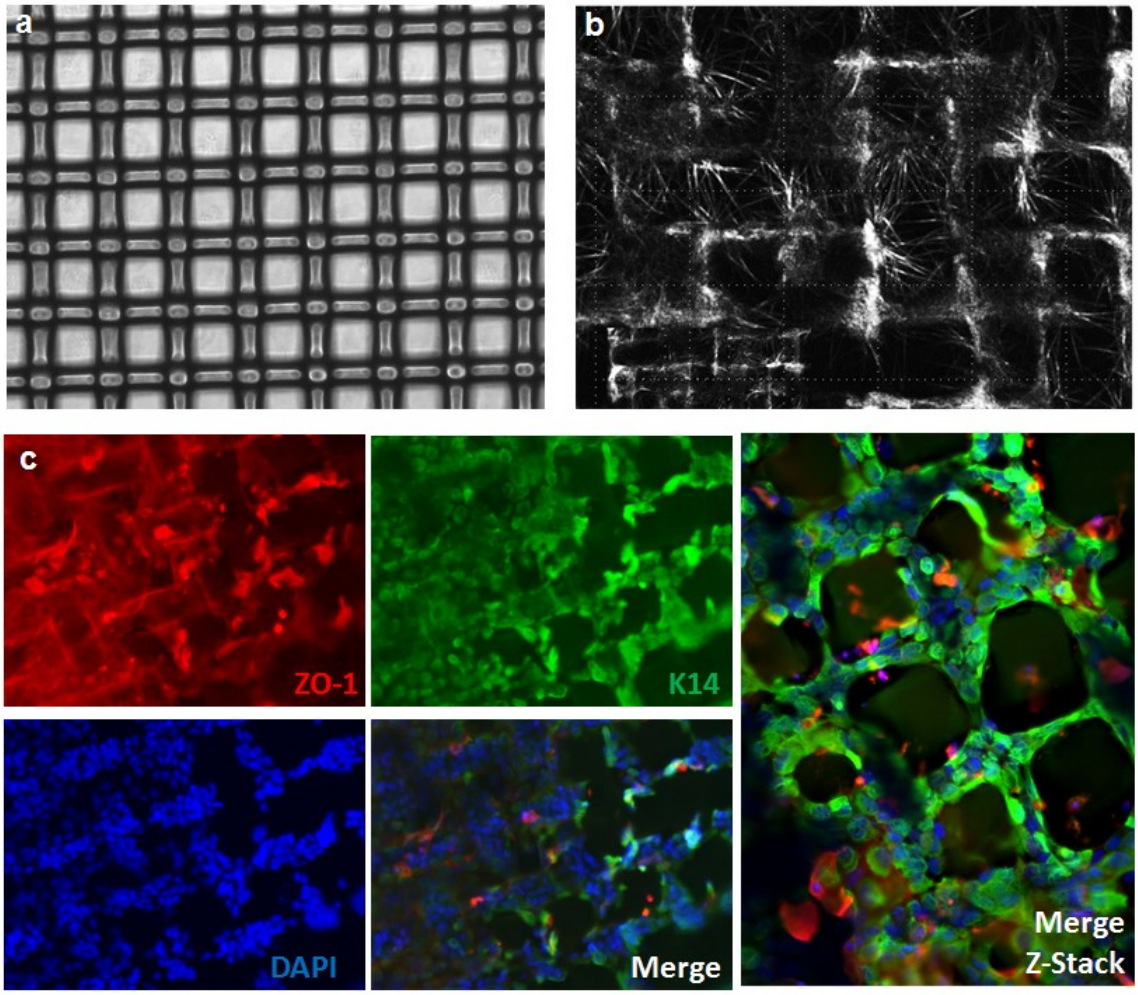

Figure 6.7 Micropatterning collagen ultrastructures on AMC materials. a) Micropattern mesh used to initiate guided fibril formation, **b)** SHG imaging of micropatterned AMC materials to visualize collagen fibril formation patterns, **c)** Corneal epithelial cell maturation with immunofluorescence markers K14, ZO-1 and DAPI on micropatterned AMC material at 72 hr.

.

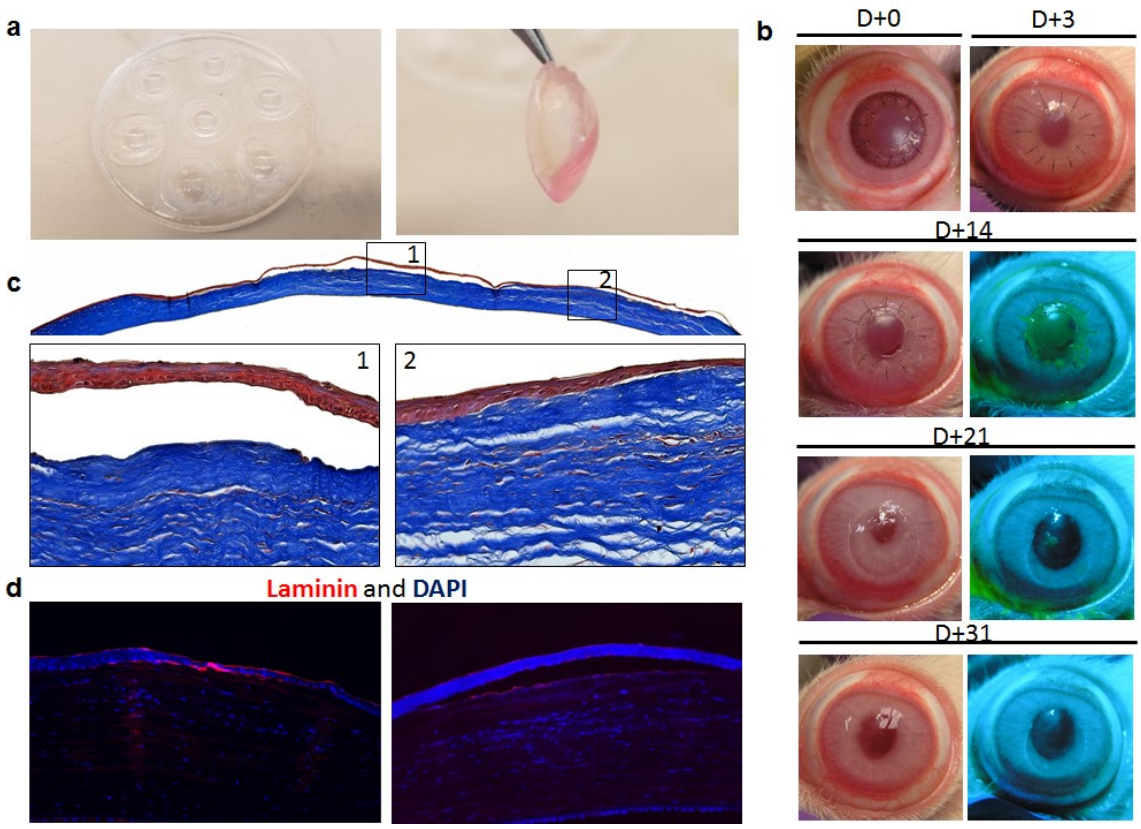

Figure 6.8 In vivo implantation of AMC vitrigels in rabbit model. a) Custom-made PDMS molds to manufacture lenticular AMC materials, **b)** Implanted AMC materials tracked over 31 days via anterior lamellar keratoplasty through gross images and fluorescein staining, **c)** Masson's Trichrome histology to observe integration of the implant, **d)** immunohistochemistry to detect basement membrane protein laminin (red).

References

1. Sykakis E, Carley F, Irion L, Denton J, Hillarby MC (2012) An in depth analysis of histopathological characteristics found in keratoconus. Pathology 44: 234-239.
2. Jhanji V, Sharma N, Vajpayee RB (2011) Management of keratoconus: current scenario. Br J Ophthalmol 95: 1044-1050.
3. John Wittenborn DR (2013) Cost of Vision Problems: The Economic Burden of Vision Loss and Eye Disorders in the United States. Chicago: Prevent Blindness America.
4. (2013) Eye Banking Statistical Report. Washington, DC: Eye Bank Association of America.
5. Qazi Y, Hamrah P (2013) Corneal Allograft Rejection: Immunopathogenesis to Therapeutics. Journal of clinical & cellular immunology 2013.
6. Niederkorn JY (2010) High-risk corneal allografts and why they lose their immune privilege. Current opinion in allergy and clinical immunology 10: 493-497.
7. (1992) The collaborative corneal transplantation studies (CCTS). Effectiveness of histocompatibility matching in high-risk corneal transplantation. The Collaborative Corneal Transplantation Studies Research Group. Archives of ophthalmology 110: 1392-1403.
8. Maguire MG, Stark WJ, Gottsch JD, Stulting RD, Sugar A, et al. (1994) Risk factors for corneal graft failure and rejection in the collaborative corneal transplantation studies. Collaborative Corneal Transplantation Studies Research Group. Ophthalmology 101: 1536-1547.
9. Schwartz EC, Huss R, Hopkins A, Dadjim B, Madjitoloum P, et al. (1997) Blindness and visual impairment in a region endemic for onchocerciasis in the Central African Republic. The British journal of ophthalmology 81: 443-447.
10. Gain P, Jullienne R, He Z, Aldossary M, Acquart S, et al. (2016) Global Survey of Corneal Transplantation and Eye Banking. JAMA ophthalmology 134: 167-173.
11. Guilbert E, Bullet J, Sandali O, Basli E, Laroche L, et al. (2013) Long-term rejection incidence and reversibility after penetrating and lamellar keratoplasty. American journal of ophthalmology 155: 560-569 e562.
12. DelMonte DW, Kim T (2011) Anatomy and physiology of the cornea. Journal of cataract and refractive surgery 37: 588-598.
13. Akhtar S, Bron AJ, Salvi SM, Hawksworth NR, Tuft SJ, et al. (2008) Ultrastructural analysis of collagen fibrils and proteoglycans in keratoconus. Acta ophthalmologica 86: 764-772.
14. McCall AS, Kraft S, Edelhauser HF, Kidder GW, Lundquist RR, et al. (2010) Mechanisms of Corneal Tissue Cross-linking in Response to Treatment with Topical Riboflavin and Long-Wavelength Ultraviolet Radiation (UVA). Investigative Ophthalmology & Visual Science 51: 129-138.
15. Zhang YT, Conrad AH, Conrad GW (2011) Effects of Ultraviolet-A and Riboflavin on the Interaction of Collagen and Proteoglycans during Corneal Cross-linking. Journal of Biological Chemistry 286: 13011-13022.
16. Kong HJ, Boontheekul T, Mooney DJ (2006) Quantifying the relation between adhesion ligand-receptor bond formation and cell phenotype. Proceedings of the National Academy of Sciences of the United States of America 103: 18534-18539.
17. Messmer EM, Meyer P, Herwig MC, Loeffler KU, Schirra F, et al. (2013) Morphological and Immunohistochemical Changes After Corneal Cross-Linking. Cornea 32: 111-117.
18. Freund DE, McCally RL, Farrell RA, Cristol SM, L'Hernault NL, et al. (1995) Ultrastructure in anterior and posterior stroma of perfused human and rabbit corneas. Relation to transparency. Invest Ophthalmol Vis Sci 36: 1508-1523.

19. Komai Y, Ushiki T (1991) The three-dimensional organization of collagen fibrils in the human cornea and sclera. Invest Ophthalmol Vis Sci 32: 2244-2258.
20. Maurice DM (1957) The structure and transparency of the cornea. J Physiol 136: 263-286.
21. Barrett GD (1987) Intraocular lens implants. USA: Ezekiel Nominees Pty. Ltd.
22. Jiraskova N, Rozsival P, Burova M, Kalfertova M (2011) AlphaCor artificial cornea: clinical outcome. Eye 25: 1138-1146.
23. Liu Y, Gan L, Carlsson DJ, Fagerholm P, Lagali N, et al. (2006) A simple, cross-linked collagen tissue substitute for corneal implantation. Investigative ophthalmology & visual science 47: 1869-1875.
24. Ahn JI, Kuffova L, Merrett K, Mitra D, Forrester JV, et al. (2013) Crosslinked collagen hydrogels as corneal implants: effects of sterically bulky vs. non-bulky carbodiimides as crosslinkers. Acta biomaterialia 9: 7796-7805.
25. Li F, Carlsson D, Lohmann C, Suuronen E, Vascotto S, et al. (2003) Cellular and nerve regeneration within a biosynthetic extracellular matrix for corneal transplantation. Proceedings of the National Academy of Sciences of the United States of America 100: 15346-15351.
26. Fagerholm P, Lagali NS, Ong JA, Merrett K, Jackson WB, et al. (2014) Stable corneal regeneration four years after implantation of a cell-free recombinant human collagen scaffold. Biomaterials 35: 2420-2427.
27. De Sa Peixoto P, Deniset-Besseau A, Schmutz M, Anglo A, Illoul C, et al. (2013) Achievement of cornea-like organizations in dense collagen I solutions: clues to the physico-chemistry of cornea morphogenesis. Soft Matter 9: 11241-11248.
28. Saeidi N, Karmelek KP, Paten JA, Zareian R, DiMasi E, et al. (2012) Molecular crowding of collagen: a pathway to produce highly-organized collagenous structures. Biomaterials 33: 7366-7374.
29. Fagerholm P, Lagali NS, Merrett K, Jackson WB, Munger R, et al. (2010) A biosynthetic alternative to human donor tissue for inducing corneal regeneration: 24-month follow-up of a phase 1 clinical study. Sci Transl Med 2: 46ra61.
30. Gil ES, Mandal BB, Park SH, Marchant JK, Omenetto FG, et al. (2010) Helicoidal multi-lamellar features of RGD-functionalized silk biomaterials for corneal tissue engineering. Biomaterials 31: 8953-8963.
31. Deshpande P, Ramachandran C, Sefat F, Mariappan I, Johnson C, et al. (2013) Simplifying corneal surface regeneration using a biodegradable synthetic membrane and limbal tissue explants. Biomaterials 34: 5088-5106.
32. Takezawa T, Ozaki K, Nitani A, Takabayashi C, Shimo-Oka T (2004) Collagen vitrigel: a novel scaffold that can facilitate a three-dimensional culture for reconstructing organoids. Cell Transplant 13: 463-473.
33. McIntosh Ambrose W, Salahuddin A, So S, Ng S, Ponce Marquez S, et al. (2009) Collagen Vitrigel membranes for the in vitro reconstruction of separate corneal epithelial, stromal, and endothelial cell layers. J Biomed Mater Res B Appl Biomater 90: 818-831.
34. McIntosh Ambrose W, Schein O, Elisseeff J (2010) A tale of two tissues: stem cells in cartilage and corneal tissue engineering. Current stem cell research & therapy 5: 37-48.
35. Calderon-Colon X, Xia Z, Breidenich JL, Mulreany DG, Guo Q, et al. (2012) Structure and properties of collagen vitrigel membranes for ocular repair and regeneration applications. Biomaterials 33: 8286-8295.
36. Guo Q, Phillip JM, Majumdar S, Wu PH, Chen J, et al. (2013) Modulation of keratocyte phenotype by collagen fibril nanoarchitecture in membranes for corneal repair. Biomaterials 34: 9365-9372.
37. Chae JJ, Ambrose WM, Espinoza FA, Mulreany DG, Ng S, et al. (2015) Regeneration of corneal epithelium utilizing a collagen vitrigel membrane in rabbit models for corneal stromal wound and limbal stem cell deficiency. Acta ophthalmologica 93: e57-66.

38. Rosso F, Giordano A, Barbarisi M, Barbarisi A (2004) From cell-ECM interactions to tissue engineering. Journal of cellular physiology 199: 174-180.
39. Berrier AL, Yamada KM (2007) Cell-matrix adhesion. Journal of cellular physiology 213: 565-573.
40. Guilak F, Cohen DM, Estes BT, Gimble JM, Liedtke W, et al. (2009) Control of stem cell fate by physical interactions with the extracellular matrix. Cell Stem Cell 5: 17-26.
41. Ruberti JW, Zieske JD (2008) Prelude to corneal tissue engineering - gaining control of collagen organization. Progress in retinal and eye research 27: 549-577.
42. Meek KM (2009) Corneal collagen-its role in maintaining corneal shape and transparency. Biophys Rev 1: 83-93.
43. Hassell JR, Birk DE (2010) The molecular basis of corneal transparency. Exp Eye Res 91: 326-335.
44. Romero-Jimenez M, Santodomingo-Rubido J, Wolffsohn JS (2010) Keratoconus: a review. Cont Lens Anterior Eye 33: 157-166; quiz 205.
45. Sugar J, Macsai MS (2012) What causes keratoconus? Cornea 31: 716-719.
46. Funderburgh JL, Mann MM, Funderburgh ML (2003) Keratocyte phenotype mediates proteoglycan structure: a role for fibroblasts in corneal fibrosis. J Biol Chem 278: 45629-45637.
47. West-Mays JA, Dwivedi DJ (2006) The keratocyte: corneal stromal cell with variable repair phenotypes. The international journal of biochemistry & cell biology 38: 1625-1631.
48. Beales MP, Funderburgh JL, Jester JV, Hassell JR (1999) Proteoglycan synthesis by bovine keratocytes and corneal fibroblasts: maintenance of the keratocyte phenotype in culture. Invest Ophthalmol Vis Sci 40: 1658-1663.
49. Muthusubramaniam L, Peng L, Zaitseva T, Paukshto M, Martin GR, et al. (2012) Collagen fibril diameter and alignment promote the quiescent keratocyte phenotype. J Biomed Mater Res A 100: 613-621.
50. Brown RA, Wiseman, M., Chuo, C.-B., Cheema, U., Nazhat, S.N. (2005) Ultrarapid engineering of biomimetic materials and tissues: Fabrication of nano- and microstructures by plastic compression. Advanced Functional Materials 15: 1762-1770.
51. Mi S, Chen B, Wright B, Connon CJ (2010) Ex vivo construction of an artificial ocular surface by combination of corneal limbal epithelial cells and a compressed collagen scaffold containing keratocytes. Tissue Eng Part A 16: 2091-2100.
52. Jones RR, Hamley IW, Connon CJ (2012) Ex vivo expansion of limbal stem cells is affected by substrate properties. Stem cell research 8: 403-409.
53. Espana EM, He H, Kawakita T, Di Pascuale MA, Raju VK, et al. (2003) Human keratocytes cultured on amniotic membrane stroma preserve morphology and express keratocan. Invest Ophthalmol Vis Sci 44: 5136-5141.
54. Puleo CM, McIntosh Ambrose W, Takezawa T, Elisseeff J, Wang TH (2009) Integration and application of vitrified collagen in multilayered microfluidic devices for corneal microtissue culture. Lab on a chip 9: 3221-3227.
55. Bailey AJ, Paul RG, Knott L (1998) Mechanisms of maturation and ageing of collagen. Mech Ageing Dev 106: 1-56.
56. Wu PH, Hung SH, Ren T, Shih Ie M, Tseng Y (2011) Cell cycle-dependent alteration in NAC1 nuclear body dynamics and morphology. Phys Biol 8: 015005.
57. Chen WC, Wu PH, Phillip JM, Khatau SB, Choi JM, et al. (2013) Functional interplay between the cell cycle and cell phenotypes. Integr Biol (Camb) 5: 523-534.
58. Chambliss AB, Wu PH, Chen WC, Sun SX, Wirtz D (2013) Simultaneously defining cell phenotypes, cell cycle, and chromatin modifications at single-cell resolution. FASEB J 27: 2667-2676.
59. Gonzalez RC WR (1992) Digital image processing. Boston, MA: Addison-Wesley Longman Publishing Co., Inc.

60. Livak KJ, Schmittgen TD (2001) Analysis of relative gene expression data using real-time quantitative PCR and the 2(-Delta Delta C(T)) Method. Methods 25: 402-408.
61. Xia ZY C-CX, Trexler M, Elisseeff J, Guo QY. (2012) Thermal denaturation of type I collagen vitrified gels. Thermochimica Acta 527: 172-179.
62. Muller LJ, Pels E, Vrensen GF (2001) The effects of organ-culture on the density of keratocytes and collagen fibers in human corneas. Cornea 20: 86-95.
63. Chen Y, Thompson DC, Koppaka V, Jester JV, Vasiliou V (2013) Ocular aldehyde dehydrogenases: protection against ultraviolet damage and maintenance of transparency for vision. Progress in retinal and eye research 33: 28-39.
64. Plant AL, Bhadriraju K, Spurlin TA, Elliott JT (2009) Cell response to matrix mechanics: focus on collagen. Biochimica et biophysica acta 1793: 893-902.
65. Rafat M, Li F, Fagerholm P, Lagali NS, Watsky MA, et al. (2008) PEG-stabilized carbodiimide crosslinked collagen-chitosan hydrogels for corneal tissue engineering. Biomaterials 29: 3960-3972.
66. Mason BN, Starchenko A, Williams RM, Bonassar LJ, Reinhart-King CA (2013) Tuning three-dimensional collagen matrix stiffness independently of collagen concentration modulates endothelial cell behavior. Acta Biomater 9: 4635-4644.
67. Saeidi N, Sander EA, Zareian R, Ruberti JW (2011) Production of highly aligned collagen lamellae by combining shear force and thin film confinement. Acta biomaterialia 7: 2437-2447.
68. Xuan M, Wang S, Liu X, He Y, Li Y, et al. (2016) Proteins of the corneal stroma: importance in visual function. Cell Tissue Res 364: 9-16.
69. Roberts CJ, Dupps WJ, Jr. (2014) Biomechanics of corneal ectasia and biomechanical treatments. J Cataract Refract Surg 40: 991-998.
70. Akhtar S, Bron AJ, Salvi SM, Hawksworth NR, Tuft SJ, et al. (2008) Ultrastructural analysis of collagen fibrils and proteoglycans in keratoconus. Acta Ophthalmol 86: 764-772.
71. Meek KM, Tuft SJ, Huang Y, Gill PS, Hayes S, et al. (2005) Changes in collagen orientation and distribution in keratoconus corneas. Invest Ophthalmol Vis Sci 46: 1948-1956.
72. Keating A, Pineda R, 2nd, Colby K (2010) Corneal cross linking for keratoconus. Semin Ophthalmol 25: 249-255.
73. Wollensak G, Spoerl E, Seiler T (2003) Stress-strain measurements of human and porcine corneas after riboflavin-ultraviolet-A-induced cross-linking. J Cataract Refract Surg 29: 1780-1785.
74. Wollensak G, Spoerl E, Wilsch M, Seiler T (2003) Endothelial cell damage after riboflavin-ultraviolet-A treatment in the rabbit. J Cataract Refract Surg 29: 1786-1790.
75. Dhawan S, Rao K, Natrajan S (2011) Complications of corneal collagen cross-linking. J Ophthalmol 2011: 869015.
76. Sady C, Khosrof S, Nagaraj R (1995) Advanced Maillard reaction and crosslinking of corneal collagen in diabetes. Biochem Biophys Res Commun 214: 793-797.
77. Michelacci YM (2003) Collagens and proteoglycans of the corneal extracellular matrix. Braz J Med Biol Res 36: 1037-1046.
78. Hassell JR, Cintron C, Kublin C, Newsome DA (1983) Proteoglycan changes during restoration of transparency in corneal scars. Arch Biochem Biophys 222: 362-369.
79. Metzler KM, Roberts CJ, Mahmoud AM, Agarwal G, Liu J (2016) Ex Vivo Transepithelial Collagen Cross-linking in Porcine and Human Corneas Using Human Decorin Core Protein. J Refract Surg 32: 410-417.
80. Pati F, Jang J, Ha DH, Won Kim S, Rhie JW, et al. (2014) Printing three-dimensional tissue analogues with decellularized extracellular matrix bioink. Nat Commun 5: 3935.
81. Cheng CW, Solorio LD, Alsberg E (2014) Decellularized tissue and cell-derived extracellular matrices as scaffolds for orthopaedic tissue engineering. Biotechnol Adv 32: 462-484.

82. Sasse KC, Brandt J, Lim DC, Ackerman E (2013) Accelerated healing of complex open pilonidal wounds using MatriStem extracellular matrix xenograft: nine cases. J Surg Case Rep 2013.
83. Gattazzo F, Urciuolo A, Bonaldo P (2014) Extracellular matrix: a dynamic microenvironment for stem cell niche. Biochim Biophys Acta 1840: 2506-2519.
84. Swinehart IT, Badylak SF (2016) Extracellular matrix bioscaffolds in tissue remodeling and morphogenesis. Dev Dyn 245: 351-360.
85. Sadtler K, Estrellas K, Allen BW, Wolf MT, Fan H, et al. (2016) Developing a pro-regenerative biomaterial scaffold microenvironment requires T helper 2 cells. Science 352: 366-370.
86. Rohaina CM, Then KY, Ng AM, Wan Abdul Halim WH, Zahidin AZ, et al. (2014) Reconstruction of limbal stem cell deficient corneal surface with induced human bone marrow mesenchymal stem cells on amniotic membrane. Transl Res 163: 200-210.
87. Vlasov A, Sia RK, Ryan DS, Mines MJ, Stutzman RD, et al. (2016) Sutureless cryopreserved amniotic membrane graft and wound healing after photorefractive keratectomy. J Cataract Refract Surg 42: 435-443.
88. Wang X, Huang Y, Jastaneiah S, Majumdar S, Kang JU, et al. (2015) Protective Effects of Soluble Collagen during Ultraviolet-A Crosslinking on Enzyme-Mediated Corneal Ectatic Models. PloS one 10: e0136999.
89. Lin YK, Liu DC (2006) Comparison of physical-chemical properties of type I collagen from different species. Food Chemistry 99: 244-251.
90. Balasubramanian SA, Mohan S, Pye DC, Willcox MD (2012) Proteases, proteolysis and inflammatory molecules in the tears of people with keratoconus. Acta Ophthalmol 90: e303-309.
91. Pahuja N, Kumar NR, Shroff R, Shetty R, Nuijts RM, et al. (2016) Differential Molecular Expression of Extracellular Matrix and Inflammatory Genes at the Corneal Cone Apex Drives Focal Weakening in Keratoconus. Invest Ophthalmol Vis Sci 57: 5372-5382.
92. Mootha VV, Kanoff JM, Shankardas J, Dimitrijevich S (2009) Marked reduction of alcohol dehydrogenase in keratoconus corneal fibroblasts. Mol Vis 15: 706-712.
93. Garcia B, Garcia-Suarez O, Merayo-Lloves J, Alcalde I, Alfonso JF, et al. (2016) Differential Expression of Proteoglycans by Corneal Stromal Cells in Keratoconus. Invest Ophthalmol Vis Sci 57: 2618-2628.
94. Binder PS, Lindstrom RL, Stulting RD, Donnenfeld E, Wu H, et al. (2005) Keratoconus and corneal ectasia after LASIK. J Cataract Refract Surg 31: 2035-2038.
95. Li X, Rabinowitz YS, Rasheed K, Yang H (2004) Longitudinal study of the normal eyes in unilateral keratoconus patients. Ophthalmology 111: 440-446.
96. Michelacci YM (2003) Collagens and proteoglycans of the corneal extracellular matrix. Brazilian journal of medical and biological research = Revista brasileira de pesquisas medicas e biologicas / Sociedade Brasileira de Biofisica [et al] 36: 1037-1046.
97. Collier SA (2001) Is the corneal degradation in keratoconus caused by matrix-metalloproteinases? Clin Exp Ophthalmol 29: 340-344.
98. Yeung K WS (2015) Firm up your approach to corneal ectasia: optometrists must see these patients "through thick and thin". Review of Optometry 152: 28-34.
99. McCall AS, Kraft S, Edelhauser HF, Kidder GW, Lundquist RR, et al. (2010) Mechanisms of corneal tissue cross-linking in response to treatment with topical riboflavin and long-wavelength ultraviolet radiation (UVA). Invest Ophthalmol Vis Sci 51: 129-138.
100. Bekesi N, Kochevar IE, Marcos S (2016) Corneal Biomechanical Response Following Collagen Cross-Linking With Rose Bengal-Green Light and Riboflavin-UVA. Invest Ophthalmol Vis Sci 57: 992-1001.
101. DeVore DP DB (2009) Decorin Corneal Stabilization. Investigative Ophthalmology & Visual Science 50: 1758.

102. Englert C, Blunk T, Muller R, von Glasser SS, Baumer J, et al. (2007) Bonding of articular cartilage using a combination of biochemical degradation and surface cross-linking. Arthritis research & therapy 9: R47.
103. Kao WW, Liu CY (2002) Roles of lumican and keratocan on corneal transparency. Glycoconjugate journal 19: 275-285.
104. Ronca F, Palmieri L, Panicucci P, Ronca G (1998) Anti-inflammatory activity of chondroitin sulfate. Osteoarthritis and cartilage / OARS, Osteoarthritis Research Society 6 Suppl A: 14-21.
105. Li Z, Hou WS, Escalante-Torres CR, Gelb BD, Bromme D (2002) Collagenase activity of cathepsin K depends on complex formation with chondroitin sulfate. J Biol Chem 277: 28669-28676.
106. Quantock AJ, Meek KM, Ridgway AE, Bron AJ, Thonar EJ (1990) Macular corneal dystrophy: reduction in both corneal thickness and collagen interfibrillar spacing. Current eye research 9: 393-398.
107. Vrana NE, Builles N, Justin V, Bednarz J, Pellegrini G, et al. (2008) Development of a reconstructed cornea from collagen-chondroitin sulfate foams and human cell cultures. Invest Ophthalmol Vis Sci 49: 5325-5331.
108. Lai JY, Li YT, Cho CH, Yu TC (2012) Nanoscale modification of porous gelatin scaffolds with chondroitin sulfate for corneal stromal tissue engineering. Int J Nanomedicine 7: 1101-1114.
109. Wang DA, Varghese S, Sharma B, Strehin I, Fermanian S, et al. (2007) Multifunctional chondroitin sulphate for cartilage tissue-biomaterial integration. Nature materials 6: 385-392.
110. Sandri G, Bonferoni MC, Rossi S, Delfino A, Riva F, et al. (2016) Platelet lysate and chondroitin sulfate loaded contact lenses to heal corneal lesions. Int J Pharm 509: 188-196.
111. Strehin I, Nahas Z, Arora K, Nguyen T, Elisseeff J (2010) A versatile pH sensitive chondroitin sulfate-PEG tissue adhesive and hydrogel. Biomaterials 31: 2788-2797.
112. Raiskup-Wolf F, Hoyer A, Spoerl E, Pillunat LE (2008) Collagen crosslinking with riboflavin and ultraviolet-A light in keratoconus: long-term results. J Cataract Refract Surg 34: 796-801.
113. Akhtar S, Almubrad T, Paladini I, Mencucci R (2013) Keratoconus corneal architecture after riboflavin/ultraviolet A cross-linking: ultrastructural studies. Mol Vis 19: 1526-1537.
114. Spoerl E, Mrochen M, Sliney D, Trokel S, Seiler T (2007) Safety of UVA-riboflavin cross-linking of the cornea. Cornea 26: 385-389.
115. Wollensak G, Wilsch M, Spoerl E, Seiler T (2004) Collagen fiber diameter in the rabbit cornea after collagen crosslinking by riboflavin/UVA. Cornea 23: 503-507.
116. Hayes S, Kamma-Lorger CS, Boote C, Young RD, Quantock AJ, et al. (2013) The effect of riboflavin/UVA collagen cross-linking therapy on the structure and hydrodynamic behaviour of the ungulate and rabbit corneal stroma. PloS one 8: e52860.
117. Balasubramanian SA, Pye DC, Willcox MD (2010) Are proteinases the reason for keratoconus? Current eye research 35: 185-191.
118. Wang F (2008) UVA/riboflavin-induced apoptosis in mouse cornea. Ophthalmologica 222: 369-372.
119. Cherfan D, Verter EE, Melki S, Gisel TE, Doyle FJ, Jr., et al. (2013) Collagen cross-linking using rose bengal and green light to increase corneal stiffness. Invest Ophthalmol Vis Sci 54: 3426-3433.
120. Di Lullo GA, Sweeney SM, Korkko J, Ala-Kokko L, San Antonio JD (2002) Mapping the ligand-binding sites and disease-associated mutations on the most abundant protein in the human, type I collagen. J Biol Chem 277: 4223-4231.

121. Tocce EJ, Smirnov VK, Kibalov DS, Liliensiek SJ, Murphy CJ, et al. (2010) The ability of corneal epithelial cells to recognize high aspect ratio nanostructures. Biomaterials 31: 4064-4072.
122. Gasiorowski JZ, Murphy CJ, Nealey PF (2013) Biophysical cues and cell behavior: the big impact of little things. Annual review of biomedical engineering 15: 155-176.
123. Raghunathan V, McKee C, Cheung W, Naik R, Nealey PF, et al. (2013) Influence of extracellular matrix proteins and substratum topography on corneal epithelial cell alignment and migration. Tissue engineering Part A 19: 1713-1722.
124. Bron AJ (2001) The architecture of the corneal stroma. Br J Ophthalmol 85: 379-381.
125. Holmes DF, Gilpin CJ, Baldock C, Ziese U, Koster AJ, et al. (2001) Corneal collagen fibril structure in three dimensions: Structural insights into fibril assembly, mechanical properties, and tissue organization. Proceedings of the National Academy of Sciences of the United States of America 98: 7307-7312.
126. Meek KM, Quantock AJ (2001) The use of X-ray scattering techniques to determine corneal ultrastructure. Progress in retinal and eye research 20: 95-137.
127. Zhang G, Chen S, Goldoni S, Calder BW, Simpson HC, et al. (2009) Genetic evidence for the coordinated regulation of collagen fibrillogenesis in the cornea by decorin and biglycan. J Biol Chem 284: 8888-8897.
128. Chen S, Mienaltowski MJ, Birk DE (2015) Regulation of corneal stroma extracellular matrix assembly. Experimental eye research 133: 69-80.
129. Stamov DR, Muller A, Wegrowski Y, Brezillon S, Franz CM (2013) Quantitative analysis of type I collagen fibril regulation by lumican and decorin using AFM. Journal of structural biology 183: 394-403.
130. Alarcon EI, Udekwu K, Skog M, Pacioni NL, Stamplecoskie KG, et al. (2012) The biocompatibility and antibacterial properties of collagen-stabilized, photochemically prepared silver nanoparticles. Biomaterials 33: 4947-4956.
131. Alarcon EI, Udekwu KI, Noel CW, Gagnon LB, Taylor PK, et al. (2015) Safety and efficacy of composite collagen-silver nanoparticle hydrogels as tissue engineering scaffolds. Nanoscale 7: 18789-18798.
132. O'Leary LE, Fallas JA, Bakota EL, Kang MK, Hartgerink JD (2011) Multi-hierarchical self-assembly of a collagen mimetic peptide from triple helix to nanofibre and hydrogel. Nat Chem 3: 821-828.
133. Dewavrin JY, Hamzavi N, Shim VP, Raghunath M (2014) Tuning the architecture of three-dimensional collagen hydrogels by physiological macromolecular crowding. Acta biomaterialia 10: 4351-4359.
134. Chellam J, Mandal AB (2013) Influence of cyclodextrins on the physical properties of collagen. International Journal of Pharma and Bio Sciences 4: 795-780.
135. McIntosh Ambrose W, Salahuddin A, So S, Ng S, Ponce Marquez S, et al. (2009) Collagen Vitrigel membranes for the in vitro reconstruction of separate corneal epithelial, stromal, and endothelial cell layers. Journal of biomedical materials research Part B, Applied biomaterials 90: 818-831.
136. Majumdar S, Guo Q, Garza-Madrid M, Calderon-Colon X, Duan D, et al. (2015) Influence of collagen source on fibrillar architecture and properties of vitrified collagen membranes. Journal of biomedical materials research Part B, Applied biomaterials.
137. Sader JE, Chon JWM, Mulvaney P (1999) Calibration of rectangular atomic force microscope cantilevers. Review of Scientific Instruments 70: 3967-3969.
138. Martinez NF, Garcia R (2006) Measuring phase shifts and energy dissipation with amplitude modulation atomic force microscopy. Nanotechnology 17: S167-172.
139. Saenger W (1983) Stereochemistry of circularly closed oligosaccharides: cyclodextrin structure and function. Biochemical Society transactions 11 Pt 2: 136-139.

140. Greenfield NJ (2006) Using circular dichroism spectra to estimate protein secondary structure. Nature protocols 1: 2876-2890.
141. Aachmann FL, Otzen DE, Larsen KL, Wimmer R (2003) Structural background of cyclodextrin-protein interactions. Protein engineering 16: 905-912.
142. Yeguas V, Altarsha M, Monard G, Lopez R, Ruiz-Lopez MF (2011) Peptide binding to beta-cyclodextrins: structure, dynamics, energetics, and electronic effects. The journal of physical chemistry A 115: 11810-11817.
143. Shanmugam M, Ramesh D, Nagalakshmi V, Kavitha R, Rajamohan R, et al. (2008) Host-guest interaction of L-tyrosine with beta-cyclodextrin. Spectrochimica acta Part A, Molecular and biomolecular spectroscopy 71: 125-132.
144. Messner M, Kurkov SV, Jansook P, Loftsson T (2010) Self-assembled cyclodextrin aggregates and nanoparticles. International Journal of Pharmaceutics 387: 199-208.
145. He Y, Fu P, Shen X, Gao H (2008) Cyclodextrin-based aggregates and characterization by microscopy. Micron 39: 495-516.
146. Takaoka K, Koezuka M, Nakahara H (1991) Telopeptide-depleted bovine skin collagen as a carrier for bone morphogenetic protein. Journal of orthopaedic research : official publication of the Orthopaedic Research Society 9: 902-907.
147. DelMonte DW, Kim T (2011) Anatomy and physiology of the cornea. J Cataract Refract Surg 37: 588-598.
148. Fratzl P (2008) Collagen: structure and mechanics: Springer Science & Business Media.
149. Holmes DF, Gilpin CJ, Baldock C, Ziese U, Koster AJ, et al. (2001) Corneal collagen fibril structure in three dimensions: structural insights into fibril assembly, mechanical properties, and tissue organization. Proceedings of the National Academy of Sciences 98: 7307-7312.
150. Chakravarti S, Magnuson T, Lass JH, Jepsen KJ, LaMantia C, et al. (1998) Lumican regulates collagen fibril assembly: skin fragility and corneal opacity in the absence of lumican. The Journal of cell biology 141: 1277-1286.
151. Irie T, Uekama K (1999) Cyclodextrins in peptide and protein delivery. Advanced Drug Delivery Reviews 36: 101-123.
152. Szente L, Szejtli J (2004) Cyclodextrins as food ingredients. Trends in Food Science & Technology 15: 137-142.
153. Kuhn MA, Wang X, Payne WG, Ko F, Robson MC (2002) Tamoxifen decreases fibroblast function and downregulates TGF(beta2) in dupuytren's affected palmar fascia. J Surg Res 103: 146-152.
154. Payne WG, Ko F, Anspaugh S, Wheeler CK, Wright TE, et al. (2006) Down-regulating causes of fibrosis with tamoxifen: a possible cellular/molecular approach to treat rhinophyma. Annals of plastic surgery 56: 301-305.

SHOUMYO MAJUMDAR

October 17, 1989 Bangalore, India	shoumyo@jhu.edu	+1 (443) 248-7760	3120 St Paul St, Apt 213 F Baltimore, MD 21218

EDUCATION

Johns Hopkins University — Baltimore, MD, USA
PhD, Materials Science and Engineering; GRE: 790Q, 610V, 4.5W — **(Expected) Aug 2017**
Patent: #WO2015164733 A1

Johns Hopkins University — Baltimore, MD, USA
MSE, Biomedical Engineering — **2013**

RV College of Engineering — Bangalore, India
BE, Biotechnology Engineering; GPA 9.3/10.0 — **2011**

RESEARCH EXPERIENCE

Johns Hopkins University — Baltimore, MD, USA
PhD Research — **2013 – Present**

Structural and functional biomimicry of the cornea via collagen self-assembly for tissue regeneration

- Formulated collagen biomaterials which biologically and functionally mimic human cornea.
- Performed biophysical studies to study complexation, self-assembly and fibril formation in collagen.
- Characterized biomaterial properties and ultrastructure, assessed functional *in vivo* biocompatibility.

Stem cell derived retinal pigment epithelial cell maturation and proliferation on biomimetic collagen substrates

- Cultured human embryonic stem cells on collagen gels to promote differentiation into retinal pigment epithelium.
- Assessed cell attachment, pigmentation, and polarization on substrates mimicking native Bruch's membrane.

Proteoglycan-chemistry based crosslinking to halt keratoconus progression

- Optimized therapeutic dose of chondroitin sulfate - N-hydroxysuccinimide based biocompatible crosslinker.
- Assessed improvement in corneal mechanics and extracellular matrix alignment following crosslinking.
- Developed and tested novel *ex vivo* corneal ectasia models.

Masters Research — **2011 –2013**

Influence of collagen source and ultrastructure on material properties and cell behavior

- Evaluated collagen biomaterial properties based on different animal sources and extraction processes.
- Modulated and controlled of corneal stromal cell phenotype based on collagen fibrillar nanoarchitecture.

PROFESSIONAL EXPERIENCE

Eyegenix, LLC — Honolulu, HI
Industry Collaboration and technology commercialization — **2014 - Present**

- Managed prototype optimization for biosynthetic cornea which led to preclinical testing and commercial development pathways.
- Coordinated research and communication and implemented GLP-like studies, troubleshooting and quality control panels.

- Facilitated technology transfer of patented corneal implant to company's R&D personnel.

University of Delhi Delhi, India
Marine Biotechnology Research Analyst **Jun-Aug 2010**

- Determined and established optimal processing techniques and protocols for microalgal lipid extraction and purification.
- Synthesized bio-diesel from locally procured microalgal cultures.

Ranbaxy Pharmaceuticals R&D Gurgaon, India
Pharmaceutical Research Assistantship **Jun-Aug 2009**

- Streamlined recombinant cell production and DNA purification for testing large batches of recombinant protein therapeutics.
- Developed upstream processing protocols for recombinant pharmaceuticals from microbial cells.

REEEP, United Nations Vienna, Austria
Renewable Energy Consulting Assistantship **Jul-Aug 2008**

- Determined market gaps and opportunities for clean lignocellulosic bio-ethanol technology deployment as an alternative fuel source.
- Produced market intelligence reports on economic feasibility and implications in developing countries, specifically China and India.

LEADERSHIP AND TEACHING EXPERIENCE

Johns Hopkins University Baltimore, MD
Treasurer, Graduate Representative Organization **2016-2017**

- Won graduate student body elections for the 'Treasurer' position of the campus-wide organization.
- Managed annual group funding of 100,000 USD for graduate student events and professional development.

Global Engineering Innovation **Sept-Dec 2016**

- Partnered with an Indonesian non-profit to resolve engineering challenges and foster local innovation in rural Indonesia.
- Designed solar dryer to increase yield and efficiency of drying fish, as part of a 6-member team.

Medical Entrepreneurship Perspectives program **Sept-Dec 2014**

- Participated in a 10-week intensive healthcare and life science entrepreneurship workshop, instructed by industry leaders.
- Presented a persuasive pitch to commercialize a device to assist respiration during pediatric surgeries.

Co-Chair, Masters Students Council **2012-2013**

- Coordinated with multiple student organizations for social and professional development events.
- Procured funding for organizing events and excursions to boost student engagement.

Research Mentor **2013-2017**

- Trained graduate students to use specialized equipment such as DSC and rheometer in the lab framework.
- Mentored undergraduate students on analytical skills, lab protocols, aseptic techniques, safety practices.

Graduate Teaching Assistant **2011-2016**

- Conducted weekly reviews for 20-30 students, graded problem sets, designed solution keys for four theory courses.
- Lead interactive sections of 10-20 students, introduced project concepts and experimental design for laboratory courses.

RV College of Engineering Bangalore, India
Co-Chair, Biotech Students Council **2008-2011**

- Organized, fundraised for and executed annual college fests with over 500 attendees per event.

SKILLS AND TECHNIQUES

- **Biological assay development:** primary/immortalized mammalian cell and stem cell culture; migration and metabolic assays, immunofluorescence, qPCR, histology, immunohistochemistry.
- **Biophysical analyses and quantification:** DSC, CD, ITC, QCM-D.
- **Microscopy techniques:** bright-field, fluorescence, phase contrast microscopy, SEM, TEM.
- **Synthetic/biological materials development:** biomaterial and hydrogel fabrication, physical characterization, design optimization.
- **Mechanical characterization:** rheology, tensile and compressive testing, contact angle measurements.
- **Pre-clinical experience:** assistance with *in vivo* rabbit ocular surgeries and subcutaneous injections in mice.
- **Technical:** Microsoft Office, MATLAB, Photoshop, Illustrator, ImageJ, GraphPad Prism, scientific writing, statistical analysis.

SELECTED AWARDS AND HONORS

- **STAR Award - Honorable Mention**, Society for Biomaterials (2017)
- **Best Presentation Award**, Mid-Atlantic Biomaterials Day (2017)
- **Best Poster Award**, 27th Wilmer Research Meeting (2016)
- **Travel Grant Award**, Knights Templar Eye Foundation (2015),
- **Dean's Fellowship for full-tuition,** MSE, Johns Hopkins University (2011-2013)
- **Award for Academic Excellence**, RV College (2011)

PATENT

- J. Elisseeff, Q. Guo, **S. Majumdar**, A. Singh (2015), "Compositions comprising cyclodextrin incorporated collagen matrices for use in biomedical applications" (Patent application WO2015164733 A1).

PUBLICATIONS

1. **S. Majumdar**, X. Wang, S. D. Sommerfeld, J. J. Chae, E.N. Athanasopoulou, L. S. Shores, X. Duan, L. M. Amzel, F. Stellacci, O. Schein, Q. Guo, A. Singh, J. H. Elisseeff, "Artificial chaperone driven collagen self-assembly to engineer a biomimetic cornea implant.", Nature Biomedical Engineering (In Review)
2. K. Sadtler, S. D. Sommerfeld, M. T. Wolf, X. Wang, **S. Majumdar,** L. Chung, D. S. Kelkar, A. Pandey, J. Elisseeff, "Proteomic composition and immunomodulatory properties of urinary bladder matrix scaffolds in homeostasis and injury", Seminars in Immunology (2017)
3. X. Wang, **S. Majumdar**, J. Sohn, G. Ma, S. C. Yiu, W. Stark, S. Swailem, J. H. Elisseeff, "Chondroitin Sulfate-based Biocompatible Crosslinker Restores Corneal Mechanics and Collagen Alignment", Investigative Ophthalmology & Visual Science (Accepted, June 2017)
4. X. Wang, J. Maruotti, **S. Majumdar**, J. Roman, H. Mao, D. Zack, J.H. Elisseeff, "Low-Fibril Density Collagen Vitrigels Enhance Human Embryonic Stem Cell-Derived Retinal Pigment Epithelial Cell Maturation", Journal of Tissue Engineering and Regenerative Medicine (In Review)
5. **S. Majumdar**, Q. Guo, M. Garza-Madrid, X. Calderón-Colón, D. Duan, P. Carbajal, O. Schein, M. M. Trexler, J. H. Elisseeff, "Influence of collagen source on fibrillar architecture and properties of vitrified collagen membranes", Journal of Biomedical Materials Research Part B (2015)
6. X. Wang, Y. Huang, S. Jastaneiah, **S. Majumdar**, J. Kang, S. Yiu, W. Stark, J. H. Elisseeff, "Protective Effects of Soluble Collagen during Ultraviolet-A Crosslinking on Enzyme-Mediated Corneal Ectatic Models", PLoS One (2015)

7. Q. Guo, J.M. Phillip, **S. Majumdar**, P. Wu, J. Chen, X. Calderón-Colón, O. Schein, B.J. Smith, M.M. Trexler, D. Wirtz, J.H. Elisseeff, "Modulation of keratocyte phenotype by collagen fibril nanoarchitecture in membranes for corneal repair," Biomaterials 34 (2013)

CONFERENCE PRESENTATIONS

1. **S. Majumdar**, X. Wang, J. Chae, J. Sohn, J. Qin, J. H. Elisseeff, "A versatile approach to modulate collagen fibrillogenesis to alter optical and biological properties of corneal implants" Association for Research in Vision and Ophthalmology Annual Meeting, Baltimore, MD, May 7-11, 2017
2. **S. Majumdar**, X. Wang, S. D. Sommerfeld, Q. Guo, A. Singh and J. H. Elisseeff, "Modulating Cornea-Mimetic Collagen Self-Assembly Using Artificial Chaperones", Society for Biomaterials, Minneapolis, MN, April 5-8, 2017
3. **S. Majumdar**, X. Wang, J. Chae, A. Singh, O. Schein, J. H. Elisseeff, "Modulation of collagen fibrillogenesis using ammonia gas to vary optical characteristics and biological compatibility of biosynthetic corneal implants.", Mid-Atlantic Biomaterials Day, New York, NY, February 24, 2017
4. **S. Majumdar**, S.D. Sommerfeld, X. Wang, A. Singh, Q. Guo, O. Schein, J. H. Elisseeff, "Cornea-mimetic lamellar microstructure and mechanical integrity of bioinspired collagen vitrigel implants", Association for Research in Vision and Ophthalmology Annual Meeting, Seattle, WA, May 1-5, 2016
5. **S. Majumdar**, S.D. Sommerfeld, X. Wang, Q. Guo, A. Singh, J. H. Elisseeff, "Fabrication and characterization of unique self-assembling cornea-mimetic collagen biomaterials", World Biomaterials Congress, Montreal, Canada, May 17-22, 2016
6. **S. Majumdar**, S.D. Sommerfeld, X. Wang, Q. Guo, A. Singh, J. H. Elisseeff, "Unique cornea-mimetic collagen based tissue engineered biomaterials", Tissue Engineering and Regenerative Medicine International Society World Congress, Boston MA, September 8-11, 2015
7. **S. Majumdar**, Q. Guo, A. Singh, O. Schein, M. Trexler, J.H. Elisseeff, "Fabrication of cornea-mimetic, cyclodextrins collagen based biomaterials for corneal transplantation", Association for Research in Vision and Ophthalmology Annual Meeting, Denver, CO, May 2-7, 2015
8. **S. Majumdar**, S.D. Sommerfeld, X. Wang, Q. Guo, A. Singh, J. H. Elisseeff, "Unique cornea-mimetic collagen based tissue engineered biomaterials", Tissue Engineering and Regenerative Medicine International Society World Congress, Boston MA, September 8-11, 2015
9. S.D. Sommerfeld, **S. Majumdar**, X. Wang, Q. Guo, A. Singh, J. H. Elisseeff, "Artificial Chaperones in the Ultra-structure Formation in Biomimetic Collagen Membranes", Tissue Engineering and Regenerative Medicine International Society World Congress, Boston MA, September 8-11, 2015
10. **S. Majumdar**, M. Trexler, O. Schein, J. H. Elisseeff, "Multilayered Collagen Vitrigels for Increased Suturability while Maintaining High Transparency for Corneal Applications", Tissue Engineering and Regenerative Medicine International Society, Washington, D.C., Dec 13-16, 2014
11. **S. Majumdar**, X. Calderón-Colón, M. Trexler, O. Schein, J.H. Elisseeff, "Electric Field mediated alignment of Collagen fibers in collagen vitrigel materials", Association for Research in Vision and Ophthalmology Annual Meeting, Orlando, FL, May 4-8, 2014.
12. Q. Guo, **S. Majumdar**, J.M. Phillip, P.-H. Wu, O. Schein, M.M. Trexler, D. Wirtz, J.H. Elisseeff, "Quantitative evaluation of keratocyte morphology controlled by biomimetic extracellular matrix," 28th Biennial Cornea Conference, Boston, MA, October 18-19, 2013.
13. **S. Majumdar**, M. Garza-Madrid, X. Calderón-Colón, M. Trexler, O. Schein, J. H. Elisseeff, "Collagen vitrigels for corneal reconstruction: collagen source and crosslinking", Association for Research in Vision and Ophthalmology Annual Meeting, Seattle, WA, May 5-9, 2013
14. M. Garza-Madrid, **S. Majumdar**, J. H. Elisseeff, "Soluble Collagen Protects Corneal Fibrils during Riboflavin Crosslinking", Association for Research in Vision and Ophthalmology Annual Meeting, Seattle, WA, May 5-9, 2013.